Graduate Theses, Dissertations, and Problem Reports

2019

Experimental and modeling investigation of the OH-initiated oxidation of semi-solid and aqueous saccharide aerosols

hanyu fan

hfan1@mix.wvu.edu

Follow this and additional works at: https://researchrepository.wvu.edu/etd

Part of the Physical Chemistry Commons

Recommended Citation

Experimental and modeling investigation of the OH-initiated oxidation of semi-solid and aqueous saccharide aerosols

Hanyu Fan

Dissertation submitted to the Eberly College of Arts and Sciences

at West Virginia University

in partial fulfillment of the requirement

for the degree of

Doctor of Philosophy

in

Chemistry

Fabien Goulay, Ph.D.

Kenneth Showalter, Ph.D.

Justin Legleiter, Ph.D.

Brian V. Popp, Ph.D.

Alan D. Bristow, Ph.D.

C. Eugene Bennett Department of Chemistry

Morgantown, West Virginia

2019

Keywords: Heterogeneous Reaction, Saccharide Aerosols, Kinetics, Reaction-diffusion kinetics model, Bulk Composition, Bulk Diffusion

Abstract

Experimental and modeling investigation of the OH-initiated oxidation of semi-solid and aqueous saccharide aerosols

Hanyu Fan

My research focuses on investigating the impact of moisture-induced and oligomer-induced viscosity changes on OH-initiated oxidation of semi-solid aerosols, and the role of gas-liquid interfaces in regulating aqueous aerosol chemistry. Saccharides, which are a major constituent of aqueous atmospheric aerosols, are chosen as model molecules to form highly oxygenated organic aerosols. The experiments are performed using an atmospheric pressure flow-tube reactor with both online VUV-AMS (Vacuum-Ultraviolet Aerosol Mass Spectrometer) and offline GC-MS analysis techniques. The decay rates of saccharide are determined by measuring the loss signal of saccharide in the particle phase as a function of OH exposure (time-integrated total concentration of OH radical). A reaction-diffusion model is developed to interpret the observed kinetics behavior. These results highlight that the chemical transformation of semi-solid aerosols is kinetically limited by bulk diffusion and that of aqueous aerosol is dependent on surface-bulk partitioning.

The kinetics of the OH-initiated oxidation of semi-solid monosaccharide particles are obtained over a range of relative humidity (RH) in order to investigate the impact of moisture-induced viscosity changes on the mechanisms of oxidative aging of semi-solid aerosols. The reactive uptake coefficient of monosaccharide (γ_{mono}) increases by a factor of 2.4 as the surrounding RH is increased from 10% to 30%. A reaction-diffusion kinetic model with a constant diffusion coefficient is developed to investigate the impact of bulk molecule diffusion on kinetics behavior of semi-solid aerosols. This study suggests that the diffusion of the bulk reactant from the particle inner core to its surface is the rate-limiting step in oxidation of the semi-solid aerosols.

In order to investigate the oligomer-induced viscosity changes on reactive properties of semi-solid aerosols, reactive uptake coefficients are measured over a range of monosaccharide:disaccharide molar ratio ranging between 1:1 and 4:1 at 30% RH. The γ_{mono} is found to decrease by a factor of 5 as the molar ratio changing from 4:1 to 1:1. The observed decay behaviors can be reproduced by using a simple compositional Vignes relationship to predict the composition-dependent diffusion coefficients of the saccharides. Simulation results suggest that a gradient diffusivity arises due to concentration gradients across the particle through heterogeneous

oxidation of semi-solid particles. These findings illustrate the impact of bulk composition on reactant bulk diffusivity, which determines the rate-limiting step during the chemical reaction of semi-solid multi-component particles.

For equimolar monosaccharide-disaccharide aqueous aerosols, the γ_{mono} is 5.02±1.12 and the γ_{di} is 0.39±0.10. Molecular dynamics simulations of the mixed aqueous solutions reveal the formation of a ~10 Å disaccharide exclusion layer below the water surface. The monosaccharide concentration is predicted to be low at the surface and to increase rapidly within the first 10 Å of the air-water interface. The observed decays are consistent with a poor spatial overlap of the OH radical at the interface with the disaccharide in the particle bulk. These findings highlight the critical importance of partitioning of bulk reactant at the gas-liquid interface in determining the reaction rate of reactive species in aqueous aerosols.

Acknowledgment

First and foremost, I would like to express my gratitude to my advisor Professor Fabien Goulay for his continuous support throughout my entire graduate career, for his immense knowledge, his patience and motivation. I am so lucky to have him as my advisor and mentor. His guidance helps me in all the time of research and writing this thesis. He is an excellent example for me in academic life. My sincere thanks go to Randall Eaglen, Allen Burns and Sherman Adams, who help me build the research experimental apparatus. Without their support it would not be possible to conduct this research. I would like to thank Dr. Mark R. Tinsley for simulating discussions. I would like to thank Dr. Novruz for his NMR experiments for structural elucidation. I would also like to express my appreciation to the formative members of the Dr. Goulay lab: Dr. Ranjith Kumar Abhinavam Kailasanathan, Dr. Juddha Thapa, Kacee Caster, James Lee, and Tadini Wenyika Masaya.

Besides my advisor, I would like to thank the rest of my committee members: Prof. Kenneth C. Showalter, Prof. Justin A. Legleiter, Prof. Brian V. Popp, Prof. Alan D. Bristow, for taking the time to serve as my committee member, but also for the questions which lead me to widen my research from various perspectives.

Last but not the least, I would like to thank my family for supporting me spiritually throughout my Ph.D. life. They are the loveliest people in the world.

Table of Contents

List of Tables

List of Figures

value. The red line is obtained by fitting the experimental data up to 0.5×10^{12} cm^{-3} s with an exponential function and extrapolated to higher OH exposure. 43

List of Abbreviations

GC-MS   Gas chromatography-mass spectrometry

MGP   Methyl β-D-glucopyranoside

SMPS   Scanning Mobility Particle Sizer

Long-DMA   Long Differential Mobility Analyzer

CPC   Condensation Particle Counter

VUV-AMS   Vacuum-Ultraviolet Photoionization Aerosol Mass Spectrometer

γ   Aerosol reactive uptake coefficient

RH   Relative Humidity

k_{MGP} the second order of heterogeneous reaction rate coefficient for OH+MGP

k_{Lac} the second order of heterogeneous reaction rate coefficient for OH+lactose

γ_{MGP} the reactive uptake coefficient for OH+MGP

γ_{Lac} the reactive uptake coefficient for OH+lactose

D_{H_2O} Diffusion coefficient for water

D_{OH} Diffusion coefficient for OH radical

D_{MGP} Diffusion coefficient for MGP

D_{Lac} Diffusion coefficient for lactose

$D_{MGP}^{30\%RH}$ Diffusion coefficient of MGP with a water activity of 0.3

$D_{Lac}^{30\%RH}$ Diffusion coefficient of lactose with a water activity of 0.3

E-R   Eley-Rideal reaction mechanism

L-H   Langmuir-Hinshelwood reaction mechanism

Chapter One

Introduction:

Heterogeneous oxidation of atmospheric organic

aerosols

Chapter 1. Introduction

1.1 Atmospheric organic aerosols

Atmospheric aerosols are defined as suspended fine solid or liquid particles in air, with a wide range of particle size (1nm to 10 µm in diameter). [1-4] The primary organic aerosols (POA) are directly emitted into the atmosphere from multiple sources: (1) natural source includes biomass burning, sea salt, volcanic eruptions, mineral dust; (2) anthropogenic source includes incomplete fossil fuel combustion, industrial and vehicle pollution. The secondary organic aerosols (SOAs) are the volatile organic compounds in the gas phase react with gas-phase oxidants such as OH, O_3, NO_3 radicals through homogeneous nucleation to form new particles, or condense to the existing particles reacting with gas-phase oxidants to form more highly oxygenated organic aerosols. [5, 6]

The presence of atmospheric aerosols could impact human being life. For example, atmospheric aerosols have ability to reduce visibility and impact climate directly by scattering and absorbing solar radiation. Atmospheric aerosols could also indirectly influence global climate by serving as cloud condensation nuclei (CCN) or ice nuclei (IN) to form cloud more readily. [7] Atmospheric aerosols have been shown to cause adverse health effects, the smallest particles can be inhaled deeply into the respiratory system and cause lung disease. [2]

1.1.1 Chemical components of atmospheric aerosol particles

The chemical components of atmospheric aerosol particles are generally divided into inorganic and organic subsets. Almost half of the atmospheric aerosol particles are organics. The inorganic salts include sulfate (32%), ammonium (13%), nitrate (11%), and chloride (1%). Carbonaceous matter includes 11% of hydrocarbon organic matter (i.e. aliphatics, polyaromatic hydrocarbons, unsaturated hydrocarbons) which are water insoluble, and 32% of oxygenated organic matter (i.e. alcohols, esters, carbonyls) which are water soluble. [8-10] A variety of configurations are shown schematically in Figure 1.1.
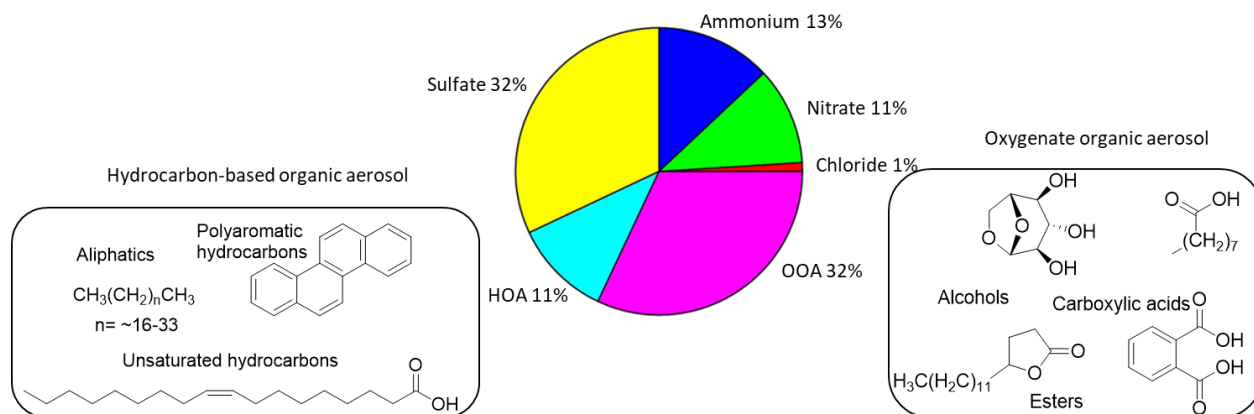
Figure 1. 1 Configurations of the average chemical composition of atmospheric aerosol particles. Specific molecule examples of hydrocarbon organic aerosol (HOA) particles and oxygenated organic aerosol (OOA) particles are identified in aerosol particles sampled in Berkeley, CA. [8-10]

1.1.2 Physical phase state of atmospheric aerosol particles

Atmospheric aerosol particles can be found in liquid phase state, semi-solid phase state, solid phase state or a mixture of both solid and liquid phase state. The particle phase is characterized according to its viscosity, η. Liquid state is like water (10^{-3} Pa s), olive oil ($\sim 10^{-1}$ Pa s) and honey ($\sim 10^{1}$ Pa s). Semisolid state is like peanut butter ($\sim 10^{3}$ Pa s) and tar pitch (10^{8} Pa s). Solid state is like glass marbles ($>10^{12}$ Pa s). [11] For viscous materials, the particle viscosity η and bulk molecule diffusion D can be related through the Stokes-Einstein equation:

$$D = \frac{k_B T}{6 \pi r \eta} \tag{1}$$

where k_B is the Boltzmann constant (1.38×10^{-23} J K^{-1}), T is the temperature (K), r is the radius of the diffusing molecule, and η is the dynamic viscosity (Pa s). Figure 1.2 is a viscosity scale together with familiar substances having a corresponding viscosity at room temperature.
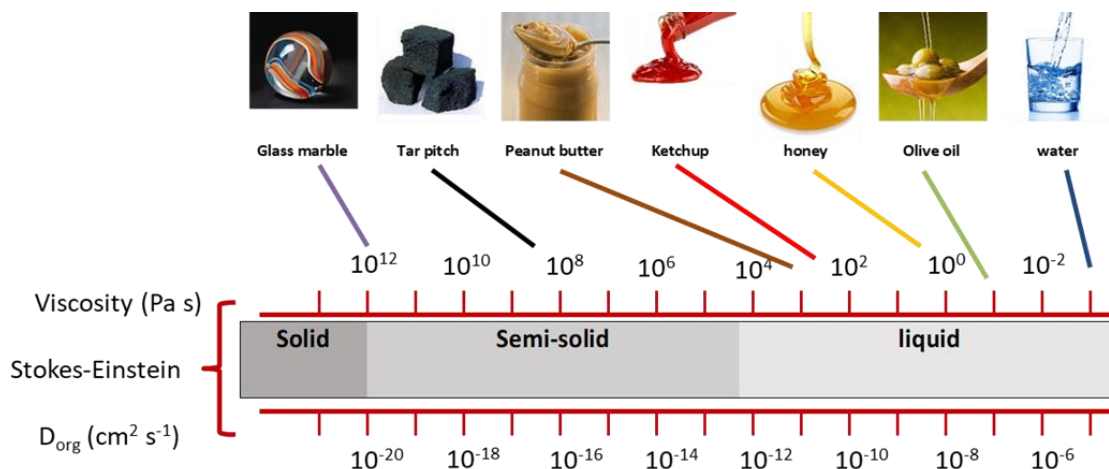
Figure 1. 2 Images of various substances as well as their approximate viscosity and diffusion coefficients at room temperature. The substances are classified into solid, semi-solid and liquid states based on their viscosity. The diffusion coefficients are calculated using Stokes-Einstein relationship equation. [11] All the substance images are from http://www.google.com.image.

The S-E equation is able to predict the diffusion coefficient for large molecule species, such as sucrose ($C_{12}H_{22}O_{11}$) in aqueous sucrose up to a viscosity of 0.1 Pa s. [12] But it has been shown to under-predict the diffusion coefficient for water molecules moving through viscous media matrix of large molecules. Such discrepancy is likely to be due to the propensity of water molecules to percolate through the network formed by the hydrogen-bonded molecules. [13, 14]

The viscosity of atmospheric particles is dependent on their chemical composition and ambient conditions. [15, 16] The controlling approach to gas-particle equilibrium are generally governed by three processes: gas-phase diffusion, interfacial transport and particle phase diffusion. For semi-solid atmospheric organic aerosols in the size range of 50 to 500 nm, the time scale to establish equilibrium between the surrounding gas phase and the particle bulk is limited by the particle-phase diffusion. The equilibrium partitioning time scale τ_{eq} in this case is:

$$\tau_{eq} = \frac{R_p^2}{\pi^2 D_b} \tag{2}$$

where R_p is the particle radius, D_b is molecular diffusion coefficient of the condensing species in the particle. [17]

1.2 Heterogeneous chemistry of atmospheric organic aerosol particles

1.2.1 General mechanism of heterogeneous oxidation of organic particles process

Figure 1.3 displays the generalized illustration of the processes during the heterogeneous oxidation of organic aerosol particles. The heterogeneous chemistry of aerosol particles involves several separate processes: (1) gas-phase diffusion: a gas molecule diffuses from the gas phase to the surface of the particle; (2) mass accommodation: the gas molecule strikes a given particle surface via collision, stick to the surface or bounce back to the gas phase; (3) surface chemical reaction: the gas-phase species react with surface-bounded particle molecules; (4) dissolution and bulk diffusion: the gas-phase species can either desorb back to the gas phase or dissolve in the bulk phase which depends on their solubility, the dissolved gas phase species then diffuse into the bulk phase; (5) bulk chemical reaction: the gas-phase molecule species react with bulk-phase molecule species. [18, 19]
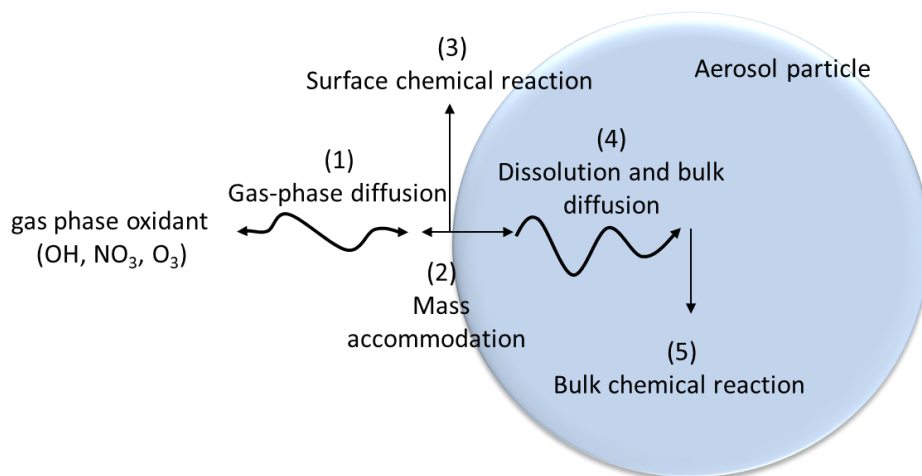
Figure 1. 3 Generalized illustration of the processes involved in the heterogeneous oxidation of an organic aerosol particle. [18, 19]

1.2.2 OH radicals uptake on a saturated hydrocarbon particle

The radical-initiated oxidation reactions of saturated hydrocarbon organic aerosol particles have long been studied. [18, 20, 21] The generalized illustration of processes that govern the kinetics of heterogeneous oxidation of organic aerosols by OH radicals are as following. First, OH radicals must diffuse from the gas phase to the surface of the particle, where the OH radicals adsorb onto

the surface site of the particle component. At the surface of the particle, the OH radicals ether desorb back into the gas phase or react with surface-bound molecules by abstracting a Hydrogen atom from an organic function group RH, leading to the formation of water and alkyl free radical. The water molecules quickly evaporate from the particle phase to the gas phase. In the presence of O_2, the alkyl radical quickly react with O_2 to form a peroxy (RO_2) radical. The peroxy (RO_2) radicals' self-reaction lead to the formation of a ketone and an alcohol which stay in the bulk, or two alkoxy (RO) radicals which could further chain propagation and form volatile oxygenated organics. A general reaction mechanism for the OH oxidation of saturated hydrocarbon molecules is shown in the Figure 1.4.
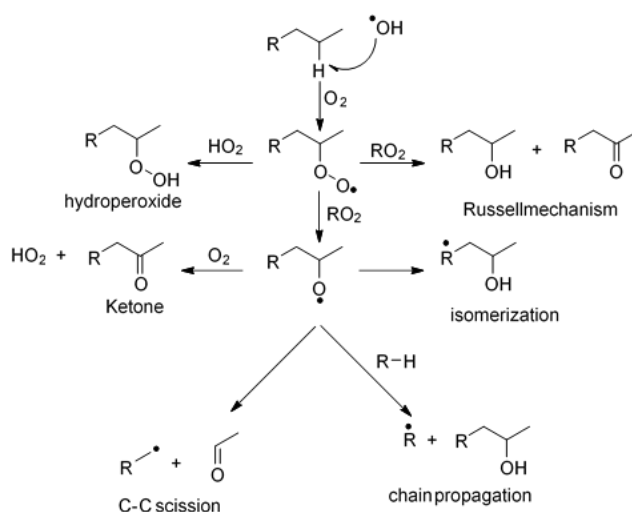
Figure 1. 4 A general chemical reaction mechanism for the OH oxidation of saturated hydrocarbon molecules. [18, 20, 21].

1.2.3 The reactive uptake coefficient (γ) of heterogeneous chemical reactions

A heterogeneous reaction is initiated by diffusion of a gas-phase reactant to the surface of a particle, followed by a collision leading to a reaction at the interface. It depends on many factors including solubility of gas-phase oxidant, reactivity of reactive species, bulk diffusion in the condensed phase, surface activity (surface tension, pH, etc.). [19] There are generally two mechanisms describing the reactive uptake at interface of particle. They are the Eley-Rideal reaction mechanism (one-step reaction) and the Langmuir-Hinshelwood reaction mechanism (two-step reaction). In the E-R, the gas-phase reactants do not adsorb onto the surface of the particle

before reacting with reactive species in the condensed phase. In the L-H, the gas-phase reactants need to adsorb onto the surface first, then followed by a reaction with a bulk molecule. [22] The diagrams of E-R and L-H are displayed in the Figure 1.5.
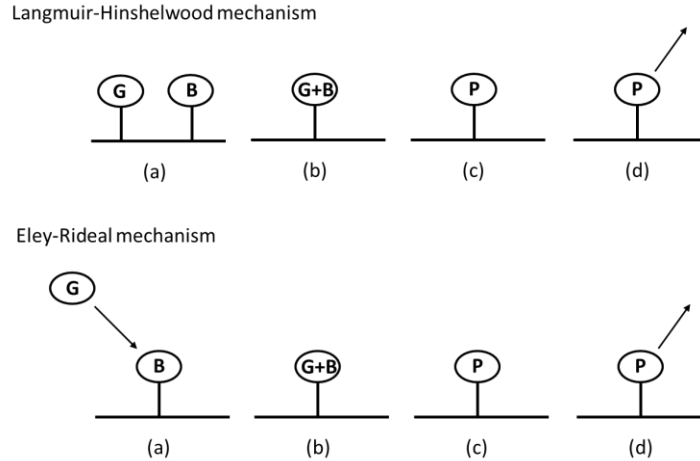
Figure 1. 5 (1) Diagram of the Langmuir-Hinshelwood (L-H) reaction G (gas-phase reactants) + B (bulk molecule) → P (products). The G need to adsorb on the surface (a) before reacting to form P (b), which may remain on the surface (c) or desorb (d). (2) Diagram of the Eley-Rideal (E-R) reaction, the G does not adsorb onto the surface prior to reaction (a, b). The P may remain on the surface (c) or desorb (d). [22]

The overall chemistry of heterogeneous reaction processes involves several elemental steps (summarized in the Figure 1.3). The relative influence of each step can be related to a net uptake coefficient (γ) as a resistance model:

$$\frac{1}{\gamma} = \frac{1}{\Gamma_g} + \frac{1}{\alpha} + \frac{1}{\Gamma_{rxn} + \Gamma_{sol}} \tag{3}$$

Where Γ_g is the gas-phase diffusion, α is the mass accommodation, Γ_{rxn} accounts for the reaction term and Γ_{sol} accounts for the solubility (dissolution). [23]

The γ reflects a combination of all the elementary steps involved in the heterogeneous chemistry reaction. It is the ratio of gas-particle collisions that leads to chemical reactions occur. [24, 25] It is determined in the following equation:

$$\gamma = \frac{2k_{Org}d_p\rho_0N_A}{3cM} \tag{4}$$

7

where k_{Org} is the observed apparent decay rate constant of the particle species (the second order of heterogeneous reaction rate coefficient). ρ_0, M, and N_A are the density of particle, the molecular weight of particle species and the Avogadro's number. d_p is the mean surface-weighted particle diameter and c is the mean speed of gas-phase reactant. If the value of γ is larger than 1, it indicates that one gas-particle collision yields more than one particle-phase reactant molecule reacted loss, and there is a secondary chain reaction occurring in the particle phase. [24, 25]

1.3 Laboratory techniques for measuring kinetics of heterogeneous reactions

The kinetics for heterogeneous reactions between gas-phase oxidant and the organic aerosol can be determined from the decay of gas-phase reactants or bulk-phase reactants. However, the gas-phase reactants loss could be due to gas phase reactions, loss on reactor walls etc. It is challenging to quantitatively analyze every single loss process described above. Therefore, it is relatively more convenient to measure the kinetics of heterogeneous reactions using the decay loss of reactants in the condensed phase and the equation describing the loss of organic particle species is as following: [24]

$$\frac{d[org]}{dt} = -k_{Org}[X_g][org] \tag{5}$$

where k_{Org} is the second order rate coefficient of heterogeneous reaction between the gas-phase oxidant and the organic aerosol. $[X_g]$ and $[org]$ are the concentration of gas-phase oxidant and bulk-phase reactant, respectively.

There are generally two parts involved to measure the kinetics of heterogeneous reactions: (1) a flow reactor or a chamber that allows aerosol particles to be exposed to gas-phase reactants under a controlled condition; (2) then an analytical method applied to measure changes in particle-phase composition or gas-phase reactant. [19] The following is a brief summary of both online and offline techniques used to measure rates of heterogeneous reactions.

1.3.1 Offline kinetics measurement method

So far there are only few studies of heterogeneous reaction kinetics measured by offline techniques. Offline kinetics measurement is typically achieved through chemical analysis of aerosol particles sample collected onto particle filters then extracted by sample extraction and

analyzed by gas chromatography-mass spectrometer (GC-MS) and high-performance liquid chromatography (HPLC). [26, 27]

Mendez et al. [26] investigated the reactivity of chlorine radical with submicron palmitic acid (PA) in a flow tube using an offline kinetic method. The kinetic has been determined from the analysis of the loss of PA in the reacted particles measured by GC-MS as a function of the chlorine exposure. Kwamena et al. [27] measured the kinetics of surface-bound anthracene onto phenysiloxane and azelaic acid aerosols with gas-phase ozone using offline analysis of anthracene loss by HPLC with ultraviolet detector.

The disadvantages of offline kinetics measurement are: (1) possible positive and negative sampling artifacts due to volatile gas compound adsorbed onto the collection filter and release of particulate-phase organics from the sample during the filter sampling; [28] (2) gas phase reactants may react with aerosol particles sample trapped onto the filter; (3) depending on the detection technique, it may require long time of sample collection; (4) sample loss during the sample preservation and sample extraction process.

1.3.2 Online kinetics measurement method

Analytical techniques such as IR, Raman and X-ray spectroscopy have limits in their applicability to resolve different chemical species. For a general purpose of detection technique, mass spectrometry is the most common technique allowed for real-time analysis of the chemical composition of organic aerosol particles. Aerosol mass spectrometry (AMS) is a powerful analysis tool applied in online heterogeneous reaction kinetics measurement with high resolution and high sensitivity. Aerosol mass spectrometer technique first vaporize aerosol sample either by thermal vaporization with hot copper tip or laser ionization. And then the vaporized particle-phase species are ionized by either a softer ionization source (e.g., vacuum ultraviolet (VUV) photoionization, [24, 29] electrospray ionization (ESI), [30] proton-transfer reaction (PTR), [31] Direct Analysis in Real Time (DART) ion source [32]) or a hard ionization source (e.g., laser, [33] Electron impact (EI) ion source [29]). The resulted ions with different mass-to-charge ratios are spatially separated through a time-of-flight tube or a quadrupole prior to detection.

1.4 Laboratory study on heterogeneous oxidation of semi-solid organic particles

1.4.1 Evidence that bulk diffusion is the rate-determining step in the heterogeneous oxidation of semi-solid organic particles

A flow tube study on the OH-initiated oxidation of squalane ($C_{30}H_{62}$) particles (well mixed particles) shows that decay behavior of particle species is in an exponential shape over the entire reaction. Figure 1.6 shows the decay of squalane as a function of OH exposure. The observed squalene decay behavior agrees well with an exponential fit. [24] Several other recent flow tube studies on small gas-phase oxidant species (OH, O_3, NO_3) reacting with semi-solid organic particles share a common kinetic behavior, which is an initial fast decay of particle-phase reactant followed by a slower decay. [31, 34-38]. Figure 1.7 displays a typical example of observed kinetic behavior in the OH oxidation of semi-solid levoglucosan particles. There is an apparent offset between the exponential fit and experimental data. The relative abundance of levoglucosan remaining in the semi-solid particles does not decay to zero due to the unreacted levogluosan in the core of the particles (with a slow mass transfer rate). [38] The discrepancy of the observed kinetics behavior between the semi-solid particles and well mixed particles is associated with the particle viscosity. For semi-solid particles, the decay of the particle-phase reactant is severely slowed or quenched due to the slow bulk diffusion. For well-mixed particles, the bulk diffusion is fast enough to allow the bulk molecule reactant in the core of the particle to diffuse to the particle surface to react with OH radicals. Here the kinetics are governed by surface reaction rate rather than bulk diffusion rate.
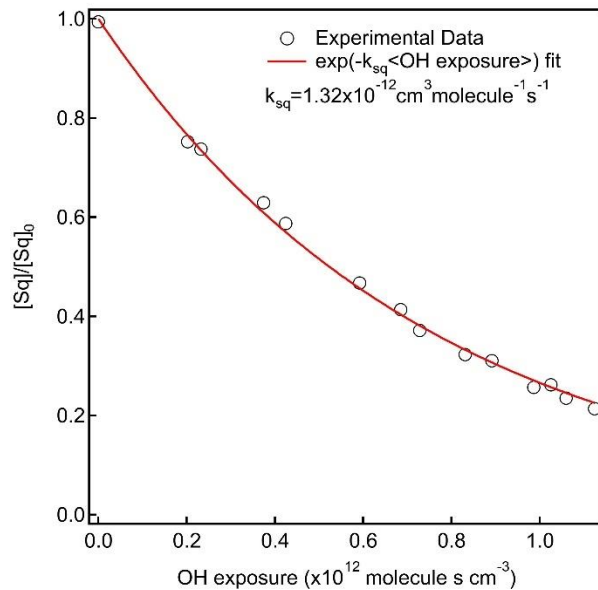
Figure 1. 6 The decay of squalane (black open circles) as a function of OH exposure is obtained for mass fragments at m/z=238, 422, and 113.13 by averaging the ion signal at three different masses. The decay is fit to exponential equation (red solid line) in order to determine the rate constant for the reaction of squalane with OH (k_{sq}), which is 1.32×10^{-12} cm^3 s^{-1}. [24]
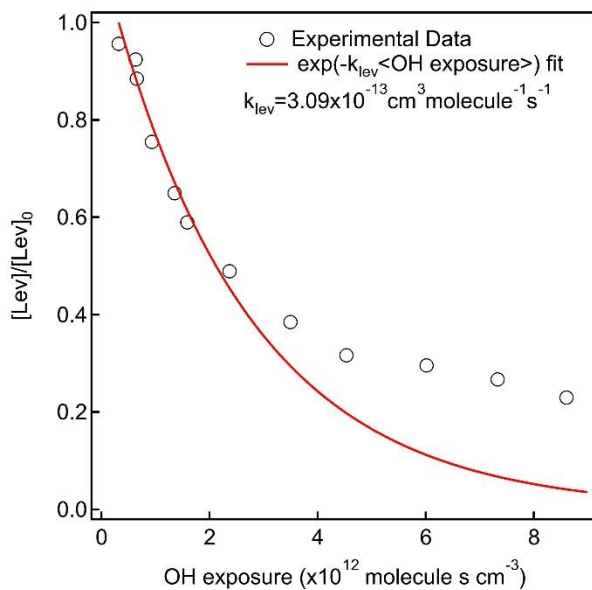
Figure 1. 7 Relative signal of unreacted levglucosan left in the particle phase as a function of OH exposure obtained for selected ions $C_6H_8O_4^+$ (black open circles). The red line is obtained by fitting the experimental data up to first e-fold of the decay. The obtained k_{lev} is 3.09×10^{-13} cm^3 s^{-1}. [38]

11

No viscosity measurements are available in the above kinetics measurement. There is a significant number of studies on investigating the variations in the diffusion coefficients of organic species either in solutions or in aerosols. [38-42] The diffusion coefficients in these matrix media are known to vary exponentially over a range of water content or organic component. [42-44] These variations are attributed to the formation of a hydrogen bond matrix among the organic molecules that eventually leads to glass transition. Surface glassy crusts have been identified during rapid drying of sucrose aerosols. This phenomenon restricts the diffusion of water into and out of the particle, ultimately leading to an extremely slow equilibrium of the water content in the particles with the surrounding relative humidity. [38] Changes in the composition of a particle, in terms of either oxygen-to-carbon (O:C) ratio or molar mass, can also lead to significant variation in the glass temperature and therefore mass transfer processes. [45] Because of the sensitive dependence of the viscosity on chemical and physical structure, small changes in solid phase composition can change the reactant diffusion coefficients by order of magnitudes, leading to complex kinetic behaviors. While studies have explicitly simulated changes in diffusivity during wetting and drying of particles, relative few of them have attempted to simulate the impact of changes in diffusivity on oxidative aging. [20, 43, 44, 46-48]

1.4.2 The effect of particle components on heterogeneous oxidation of semi-solid particles

To date studies about gas-phase oxidant species reacting with semi-solid multi-component organic particles are mainly focused on ozone oxidation of one reactive molecule species in the mixture particles. The reactive uptake coefficients of heterogeneous oxidation of semi-solid mixture particles are bulk composition dependent. Changes in particle viscosity or physical phase due to the particle composition are suggested to affect the semi-solid particle reactivity. [49-53] For example, the γ_{MA} on sucrose/MA (maleic acid, $C_2H_4O_4$) mass ratio 5:1 at 35% RH is two orders of magnitude smaller than that of sucrose/MA mass ratio 10:1 at a 40% RH due to a significant decrease in the viscosity by an addition of minor fraction of sucrose. [49] A study of the ozonolysis of highly viscous droplets of OL/SA (oleic-acid, $C_{18}H_{34}O_2$/stearic-acid, $C_{18}H_{36}O_2$) by transmission electron microscopy reported that the γ_{OL} decreased by a factor of 8 when changing from OL/SA mass ratio 1:0 to 1:1. No further changes in γ_{OL} are observed for higher SA content due to particle solidification. [50] Another study of ozonolysis of OL/n-docosane ($C_{22}H_{46}$) by CIMS (Chemical Ionization Mass Spectrometers) reported that the reaction-induced formation of a metastable solid

rotator phase of the n-docosane at the surface completely inhibits further reactions. [51] More recently, a study of the ozonolysis of OL using HR-ToF-AMS (High Resolution Time of Flight Aerosol Mass Spectrometry) found that the γ_{O_3} is decreased by two orders of magnitude as the ozone concentration is increased from 25 ppb to 1100 ppb. The authors interpret this drastic change to the formation of high-molecular-weight oligomer products at the outer layer of the particle which induce a "hard skin" (a decrease in the viscosity of particle surface) close to the particle surface limiting the diffusion of OL and O_3. [52, 53]

There is only a limited number of studies on the OH-initiated oxidation of semi-solid multi-component particles. [54, 55] Isaacman et al. [54] used GC-VUV-MS to measure the OH uptake by hydrocarbons in motor oil particles. Their results indicate that the reactive uptake coefficients of hydrocarbons are structure dependent: the values of γ_{Org} for branching hydrocarbons are bigger than these of normal alkanes and those of nonaromatic ring species are the smallest ones. The $\gamma_{squalane}$ increases by a factor of ~2 for a 42 nm thickness of the secondary organic aerosol (SOA, α-pinene+O_3) coating onto squalane particles compared to pure squalene particles using VUV-AMS. The possible explanations are that the loss of squalene buried below SOA coating are due to both direct oxidation by OH radicals and indirect secondary oxidation by SOA-derived radicals in particle phase. [55] More research is needed to give a clear trend result for an improved understanding of chemical transformation of semi-solid multi-component organic particles in the atmosphere.

1. 5 Laboratory study on heterogeneous oxidation of organic aqueous droplets

1.5.1 A kinetic framework for heterogenous oxidation of aqueous droplets

Aqueous aerosol droplets may dissolve inorganic salt ions and organic molecules. Some of the dissolved species are surface-active molecules with higher concentrations at the interface than in the bulk, which form a distinct thin water film at the air-water interface. Non-surface-active molecules predominantly be found in the bulk. [56] The pseudo-first odder reaction rate of heterogeneous oxidation of aqueous droplets depends on the surface water film thickness since it involves heterogeneous surface reaction and homogeneous bulk reaction. [57] The overall reaction rate is given by the following equation:

$$k_1 = k_{bulk} + (k_{1,\sigma}/\delta) \tag{6}$$

Where k_{bulk} and $k_{1,\sigma}$ are respectively the homogenous bulk aqueous phase and heterogeneous surface reaction rate constants, and δ is surface water film thickness. [57] Experimental observation of the UV photooxidation of two PAHs (phenanthrene and naphthalene) shows that the oxidation rate of all three major products increases as the surface water film thickness decreases, which are due to the fact that the surface water film thickness decreases, the surface heterogeneous reaction rate contributes more to the overall reaction rate. [57, 58] The generalized kinetics framework for gas-phase oxidants reacting with reactive organic species in an aqueous droplet is shown in Figure 1.8.
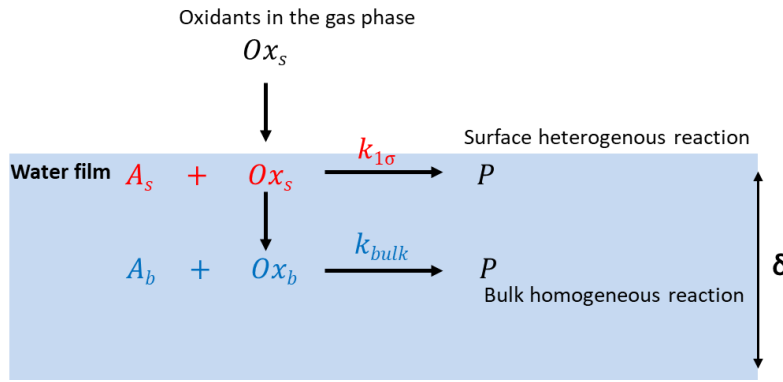
Figure 1. 8 A schematic of two reaction channels (surface heterogeneous reaction and bulk homogeneous reaction) for gas-phase oxidants reacting with organic reactive reactants in the aqueous droplet. A_s and A_b are the reactive organic species at the surface of aqueous droplet and in the bulk of droplet. Ox_s and Ox_b are the gas-phase oxidants at the surface of aqueous droplet and in the bulk of droplet. P is the product. [57]

1.5.2 Thermodynamics of the air-water interface

Pegran et al. [59] applied the thermodynamic criteria to describe a molecular species M_i in aqueous droplet to migrate from the bulk solution (B) to the air-water interface (Σ) with the corresponding partitioning equilibrium constant $K_{p,i}$:

$$K_{p,i} = \frac{[M_i]_\Sigma}{[M_i]_B} \tag{7}$$

and the corresponding partitioning Gibbs free energy is:

$$\Delta_p G° = -RT \ln K_{p,i} \tag{8}$$

14

where $[M_i]_B$ and $[M_i]_\Sigma$ are the bulk and interface concentrations, R the ideal gas constant, and T the temperature. Surface-active molecule has a negative value of $\Delta_p G^o$ and the non-surface-active molecules have a positive partitioning Gibbs free energy. For example, sucrose is a non-surface-active organic molecule with a $\Delta_p G^o$ close to 3 kcal mol^{-1}, which indicates that its concentration in bulk is 2 orders of magnitude larger than its concentration at the interface. [59] Molecules with intermediate values of $\Delta_p G^o$ could be both in the bulk and at the interface depending on its partitioning ratio.

1.5.3 Chemical Reactions at the air-water interface

The ubiquitous air-water interface plays a significant role in determining the reaction rate of surface-active molecule species. Recent Huang et al. [57] used field-induced droplet ionization mass spectrometry (FIDI-MS) to investigate the OH oxidation of pinonic acid at the air-water interface. Their result suggest that the influence of interface chemistry significantly depends on the relative presence of reactants near the surface. X-ray photoelectron spectroscopy investigated by Prisle et al. [60] on the surface partitioning of aqueous decanoate salts and the acid speciation. They reported that there is a pronounced enhancement of the acid formed at the surface by the addition of NH_4^+ cations to the bulk due to a different acid-base chemistry at the interface. In marine aqueous NaCl droplets, gaseous molecule chlorine product was observed due to the Cl$^-$ anion at the interface strongly attracts OH radicals in the gas phase and the reaction of OH and Cl$^-$ at the air-water interface are dominant. [61] Kumar et al. [62] studied the reactivity of the atmospherically relevant Criegee intermediate with nitric acid at the air-water interface. Their MD simulations suggested that surface reactions led to the formation of hydroxyethyl hydroperoxide, in stark contrast to nitroxyethyl hydroperoxide, which is formed by direct bulk reaction of the Criegee intermediate with nitric acid. These above results underscore the need to more extensively characterize interfacial competitive oxidation of aqueous species under a wide variety of different surface activity (surface tension, pH, etc.) conditions.

1.6 The motivation and object

Atmospheric aerosols (solid or liquid) react with gas-phase species involving numerous heterogeneous reactions. These multiphase reactions change the chemical and physical properties of aerosols, thereby affecting their reactive, hygroscopic, and optical properties. The chemical

transformation in the organic particles are essential for understanding, evaluating, and predicting of the global climate, air quality, and public health. [63, 64] Therefore, there is an urgent need to increase our knowledge of reactions occurring at or near the gas-particle interface and in the bulk phase. [56, 65]

The heterogeneous oxidation of aerosols is governed by chemical and physical processes occurring both in the particle bulk and at interfaces. The relative importance of these phenomena is then greatly dependent on the physical and chemical properties of the particle. [66] The chemical transformation of semi-solid particles (a viscosity range from 10^2 to 10^{12} pa s) is more likely limited by bulk diffusion from the inner core of particle to the particle surface. [31, 34-38] As the particle viscosity decreases, the diffusion coefficients of the reactive species increase by several orders of magnitude, and bulk diffusion is no longer rate-limiting. There is increasing evidence suggests that the oxidation reactions occurring at or close to the gas-liquid interface may be controlled by surface partitioning of the reactive species. [57, 60]

This thesis mainly focuses on trying to answer 4 key research questions regarding the heterogeneous oxidation of organic aerosols:

- What is the impact of moisture-induced viscosity changes on the mechanisms of oxidative aging of semi-solid single-component particles?
- What is the effect of oligomer-induced viscosity changes in the bulk phase on the reaction rates of reactive species in the semi-solid multi-component particles?
- What is the rate-limiting step in the heterogeneous oxidation of aqueous droplets?
- What is the role of gas-liquid interfaces in the oxidation of aqueous aerosols chemistry?

In Chapter 3 the kinetic of the OH-initiated heterogeneous oxidation of semi-solid particles was investigated for relative humidity ranging from 10% to 30% in Chapter 3. The kinetics measured by monitoring the loss of particle-phase reactants using Vacuum-Ultraviolet Photoionization Aerosol Mass Spectrometer (VUV-AMS). A reaction-diffusion kinetic model with constant bulk diffusion was also developed in order to evaluate the role of bulk diffusion in the heterogeneous oxidation. Chapter 4 presents the study on the kinetics of OH oxidation of semi-solid mixture particles for different monosaccharide:disaccharide molar ratio at 30% relative

humidity. A reaction-diffusion kinetic model with a composition-dependent bulk diffusion was developed in order to further investigate the impact of oligomer-induced viscosity changes on heterogeneous oxidation of semi-solid multi-component particles. In this model, the bulk diffusion was corrected to account for changes in the chemical composition. Chapter 5 presents the kinetics result from the OH-oxidation of aqueous equimolar monosaccharide-disaccharide droplets and pure disaccharide aqueous droplets. The role of surface-bulk partitioning in the aqueous aerosol chemistry is discussed.

References:

1. Finlayson-Pitts, B. J.; Pitts, J. N., Tropospheric Air Pollution: Ozone, Airborne Toxics, Polycyclic Aromatic Hydrocarbons, and Particles. *Science* **1997,** *276* (5315), 1045-1051.

2. Bernstein, J. A.; Alexis, N.; Barnes, C.; Bernstein, I. L.; Bernstein, J. A.; Nel, A.; Peden, D.; Diaz-Sanchez, D.; Tarlo, S. M.; Williams, P. B., Health effects of air pollution. *The Journal of allergy and clinical immunology* **2004,** *114* (5), 1116-23.

3. Seinfeld, J. H. a. P., S. N., *Atmospheric Chemistry and Physics: Atmospheric Chemistry and Physics from air pollution to climate change*. Wiley: New York, 1998.

4. Hinds, W. C., *Aerosol Technology: Properties, Behavior, and Measurement of Airborne Particles*. Wiley: New York, 1999.

5. Pöschl, U., Atmospheric Aerosols: Composition, Transformation, Climate and Health Effects. *Angewandte Chemie International Edition* **2005,** *44* (46), 7520-7540.

6. Chapleski, R. C.; Zhang, Y.; Troya, D.; Morris, J. R., Heterogeneous chemistry and reaction dynamics of the atmospheric oxidants, O3, NO3, and OH, on organic surfaces. *Chemical Society Reviews* **2016,** *45* (13), 3731-3746.

7. Solomon, S. Q., D.; Manning, M.; Chen, Z.; Marquis, M.; Averyt, K. B.; Tignor, M. and Miller, H. L., *IPCC, 2007: Summary for Policymakers. In: Climate Change 2007: The Physical Science Basis. Contribution of Working Group I to the Fourth Assessment Report of the Intergovernmental Panel on Climate Change*. Cambridge University Press: Cambridge, United Kingdom and New York, NY, USA., 2007.

8. Williams, B. J.; Goldstein, A. H.; Kreisberg, N. M.; Hering, S. V., An In-Situ Instrument for Speciated Organic Composition of Atmospheric Aerosols: Thermal Desorption Aerosol GC/MS-FID (TAG). *Aerosol Science and Technology* **2006,** *40* (8), 627-638.

9. Zhang, Q.; Jimenez, J. L.; Canagaratna, M. R.; Allan, J. D.; Coe, H.; Ulbrich, I.; Alfarra, M. R.; Takami, A.; Middlebrook, A. M.; Sun, Y. L.; Dzepina, K.; Dunlea, E.; Docherty, K.; DeCarlo, P. F.; Salcedo, D.; Onasch, T.; Jayne, J. T.; Miyoshi, T.; Shimono, A.; Hatakeyama, S.; Takegawa, N.; Kondo, Y.; Schneider, J.; Drewnick, F.; Borrmann, S.; Weimer, S.; Demerjian, K.; Williams, P.; Bower, K.; Bahreini, R.; Cottrell, L.; Griffin, R. J.; Rautiainen, J.; Sun, J. Y.; Zhang, Y. M.; Worsnop, D. R., Ubiquity and dominance of oxygenated species in organic

aerosols in anthropogenically-influenced Northern Hemisphere midlatitudes. *Geophysical Research Letters* **2007,** *34* (13).

10.   McNeill, V. F.; Sareen, N.; Schwier, A. N., Surface-Active Organics in Atmospheric Aerosols. In *Atmospheric and Aerosol Chemistry*, McNeill, V. F.; Ariya, P. A., Eds. Springer Berlin Heidelberg: Berlin, Heidelberg, 2014; pp 201-259.

11.   Koop, T.; Bookhold, J.; Shiraiwa, M.; Poschl, U., Glass transition and phase state of organic compounds: dependency on molecular properties and implications for secondary organic aerosols in the atmosphere. *Physical chemistry chemical physics : PCCP* **2011,** *13* (43), 19238-55.

12.   Power, R. M.; Simpson, S. H.; Reid, J. P.; Hudson, A. J., The transition from liquid to solid-like behaviour in ultrahigh viscosity aerosol particles. *Chemical Science* **2013,** *4* (6), 2597-2604.

13.   Price, H. C.; Murray, B. J.; Mattsson, J.; O'Sullivan, D.; Wilson, T. W.; Baustian, K. J.; Benning, L. G., Quantifying water diffusion in high-viscosity and glassy aqueous solutions using a Raman isotope tracer method. *Atmos. Chem. Phys.* **2014,** *14* (8), 3817-3830.

14.   Mazza, M. G.; Giovambattista, N.; Stanley, H. E.; Starr, F. W., Connection of translational and rotational dynamical heterogeneities with the breakdown of the Stokes-Einstein and Stokes-Einstein-Debye relations in water. *Physical Review E* **2007,** *76* (3), 031203.

15.   Martin, S. T., Phase Transitions of Aqueous Atmospheric Particles. *Chemical Reviews* **2000,** *100* (9), 3403-3454.

16.   Marcolli, C.; Luo, B.; Peter, T., Mixing of the Organic Aerosol Fractions: Liquids as the Thermodynamically Stable Phases. *The Journal of Physical Chemistry A* **2004,** *108* (12), 2216-2224.

17.   Mai, H.; Shiraiwa, M.; Flagan, R. C.; Seinfeld, J. H., Under What Conditions Can Equilibrium Gas–Particle Partitioning Be Expected to Hold in the Atmosphere? *Environmental Science & Technology* **2015,** *49* (19), 11485-11491.

18.   George, I. J.; Abbatt, J. P. D., Heterogeneous oxidation of atmospheric aerosol particles by gas-phase radicals. *Nature Chemistry* **2010,** *2*, 713.

19.   Davies, J. F.; Wilson, K. R., Chapter 13 - Heterogeneous Reactions in Aerosol. In *Physical Chemistry of Gas-Liquid Interfaces*, Faust, J. A.; House, J. E., Eds. Elsevier: 2018; pp 403-433.

20.   Shiraiwa, M.; Ammann, M.; Koop, T.; Pöschl, U., Gas uptake and chemical aging of semisolid organic aerosol particles. *Proceedings of the National Academy of Sciences* **2011,** *108* (27), 11003-11008.

21.   Wiegel, A. A.; Liu, M. J.; Hinsberg, W. D.; Wilson, K. R.; Houle, F. A., Diffusive confinement of free radical intermediates in the OH radical oxidation of semisolid aerosols. *Physical Chemistry Chemical Physics* **2017,** *19* (9), 6814-6830.

22.   Weinberg, W. H., Eley−Rideal Surface Chemistry: Direct Reactivity of Gas Phase Atomic Hydrogen with Adsorbed Species. *Accounts of Chemical Research* **1996,** *29* (10), 479-487.

23.   Worsnop, D. R.; Morris, J. W.; Shi, Q.; Davidovits, P.; Kolb, C. E., A chemical kinetic model for reactive transformations of aerosol particles. *Geophysical Research Letters* **2002,** *29* (20), 57-1-57-4.

24.   Smith, J. D.; Kroll, J. H.; Cappa, C. D.; Che, D. L.; Liu, C. L.; Ahmed, M.; Leone, S. R.; Worsnop, D. R.; Wilson, K. R., The heterogeneous reaction of hydroxyl radicals with sub-micron squalane particles: a model system for understanding the oxidative aging of ambient aerosols. *Atmos. Chem. Phys.* **2009,** *9* (9), 3209-3222.

25.   Renbaum-Wolff, L.; Smith, G. D., "Virtual Injector" Flow Tube Method for Measuring Relative Rates Kinetics of Gas-Phase and Aerosol Species. *The Journal of Physical Chemistry A* **2012,** *116* (25), 6664-6674.

26.   Mendez, M.; Ciuraru, R.; Gosselin, S.; Batut, S.; Visez, N.; Petitprez, D., *Reactivity of chlorine radical with submicron palmitic acid particles: kinetic measurements and products identification*. 2013; Vol. 13, p 16925-16960.

27.   Kwamena, N. O. A.; Staikova, M. G.; Donaldson, D. J.; George, I. J.; Abbatt, J. P. D., Role of the Aerosol Substrate in the Heterogeneous Ozonation Reactions of Surface-Bound PAHs. *The Journal of Physical Chemistry A* **2007,** *111* (43), 11050-11058.

28.   Perrino, C.; Canepari, S.; Catrambone, M., Comparing the Performance of Teflon and Quartz Membrane Filters Collecting Atmospheric PM: Influence of Atmospheric Water. *Aerosol and Air Quality Research* **2013,** *13* (1), 137-147.

29.   Canagaratna, M. R.; Jayne, J. T.; Jimenez, J. L.; Allan, J. D.; Alfarra, M. R.; Zhang, Q.; Onasch, T. B.; Drewnick, F.; Coe, H.; Middlebrook, A.; Delia, A.; Williams, L. R.; Trimborn, A. M.; Northway, M. J.; DeCarlo, P. F.; Kolb, C. E.; Davidovits, P.; Worsnop, D. R., Chemical

and microphysical characterization of ambient aerosols with the aerodyne aerosol mass spectrometer. *Mass Spectrometry Reviews* **2007,** *26* (2), 185-222.

30.	Doezema, L. A.; Longin, T.; Cody, W.; Perraud, V.; Dawson, M. L.; Ezell, M. J.; Greaves, J.; Johnson, K. R.; Finlayson-Pitts, B. J., Analysis of secondary organic aerosols in air using extractive electrospray ionization mass spectrometry (EESI-MS). *RSC Advances* **2012,** *2* (7), 2930-2938.

31.	Slade, J. H.; Knopf, D. A., Heterogeneous OH oxidation of biomass burning organic aerosol surrogate compounds: assessment of volatilisation products and the role of OH concentration on the reactive uptake kinetics. *Physical Chemistry Chemical Physics* **2013,** *15* (16), 5898-5915.

32.	Chan, M. N.; Nah, T.; Wilson, K. R., Real time in situ chemical characterization of sub-micron organic aerosols using Direct Analysis in Real Time mass spectrometry (DART-MS): the effect of aerosol size and volatility. *The Analyst* **2013,** *138* (13), 3749-57.

33.	Smith, G. D.; Woods, E.; DeForest, C. L.; Baer, T.; Miller, R. E., Reactive Uptake of Ozone by Oleic Acid Aerosol Particles: Application of Single-Particle Mass Spectrometry to Heterogeneous Reaction Kinetics. *The Journal of Physical Chemistry A* **2002,** *106* (35), 8085-8095.

34.	Zhang, H.; Ruehl, C. R.; Chan, A. W. H.; Nah, T.; Worton, D. R.; Isaacman, G.; Goldstein, A. H.; Wilson, K. R., OH-Initiated Heterogeneous Oxidation of Cholestane: A Model System for Understanding the Photochemical Aging of Cyclic Alkane Aerosols. *The Journal of Physical Chemistry A* **2013,** *117* (47), 12449-12458.

35.	Kessler, S. H.; Nah, T.; Daumit, K. E.; Smith, J. D.; Leone, S. R.; Kolb, C. E.; Worsnop, D. R.; Wilson, K. R.; Kroll, J. H., OH-Initiated Heterogeneous Aging of Highly Oxidized Organic Aerosol. *The Journal of Physical Chemistry A* **2012,** *116* (24), 6358-6365.

36.	Chan, M. N.; Zhang, H.; Goldstein, A. H.; Wilson, K. R., Role of Water and Phase in the Heterogeneous Oxidation of Solid and Aqueous Succinic Acid Aerosol by Hydroxyl Radicals. *The Journal of Physical Chemistry C* **2014,** *118* (50), 28978-28992.

37.	Zahardis, J.; Petrucci, G. A., The oleic acid-ozone heterogeneous reaction system: products, kinetics, secondary chemistry, and atmospheric implications of a model system – a review. *Atmos. Chem. Phys.* **2007,** *7* (5), 1237-1274.

38.   Kessler, S. H.; Smith, J. D.; Che, D. L.; Worsnop, D. R.; Wilson, K. R.; Kroll, J. H., Chemical Sinks of Organic Aerosol: Kinetics and Products of the Heterogeneous Oxidation of Erythritol and Levoglucosan. *Environmental Science & Technology* **2010,** *44* (18), 7005-7010.

39.   Gladden, J. K.; Dole, M., Diffusion in Supersaturated Solutions. II. Glucose Solutions. *Journal of the American Chemical Society* **1953,** *75* (16), 3900-3904.

40.   O'Leary, T. J., Concentration dependence of protein diffusion. *Biophysical journal* **1987,** *52* (1), 137-139.

41.   Rampp, M.; Buttersack, C.; Ludemann, H. D., c,T-dependence of the viscosity and the self-diffusion coefficients in some aqueous carbohydrate solutions. *Carbohydrate research* **2000,** *328* (4), 561-72.

42.   Rauch, J.; Kohler, W., Diffusion and thermal diffusion of semidilute to concentrated solutions of polystyrene in toluene in the vicinity of the glass transition. *Physical review letters* **2002,** *88* (18), 185901.

43.   Zobrist, B.; Soonsin, V.; Luo, B. P.; Krieger, U. K.; Marcolli, C.; Peter, T.; Koop, T., Ultra-slow water diffusion in aqueous sucrose glasses. *Physical chemistry chemical physics : PCCP* **2011,** *13* (8), 3514-26.

44.   Bones, D. L.; Reid, J. P.; Lienhard, D. M.; Krieger, U. K., Comparing the mechanism of water condensation and evaporation in glassy aerosol. *Proceedings of the National Academy of Sciences* **2012,** *109* (29), 11613-11618.

45.   Angell, C. A., Formation of Glasses from Liquids and Biopolymers. *Science* **1995,** *267* (5206), 1924-1935.

46.   Pfrang, C.; Shiraiwa, M.; Pöschl, U., Chemical ageing and transformation of diffusivity in semi-solid multi-component organic aerosol particles. *Atmos. Chem. Phys.* **2011,** *11* (14), 7343-7354.

47.   Shiraiwa, M.; Zuend, A.; Bertram, A. K.; Seinfeld, J. H., Gas–particle partitioning of atmospheric aerosols: interplay of physical state, non-ideal mixing and morphology. *Physical Chemistry Chemical Physics* **2013,** *15* (27), 11441-11453.

48.   Kroll, J. H.; Smith, J. D.; Che, D. L.; Kessler, S. H.; Worsnop, D. R.; Wilson, K. R., Measurement of fragmentation and functionalization pathways in the heterogeneous oxidation of oxidized organic aerosol. *Physical Chemistry Chemical Physics* **2009,** *11* (36), 8005-8014.

49.   Marshall, F. H.; Miles, R. E. H.; Song, Y.-C.; Ohm, P. B.; Power, R. M.; Reid, J. P.; Dutcher, C. S., Diffusion and reactivity in ultraviscous aerosol and the correlation with particle viscosity. *Chemical Science* **2016,** *7* (2), 1298-1308.

50.   Katrib, Y.; Biskos, G.; Buseck, P. R.; Davidovits, P.; Jayne, J. T.; Mochida, M.; Wise, M. E.; Worsnop, D. R.; Martin, S. T., Ozonolysis of Mixed Oleic-Acid/Stearic-Acid Particles: Reaction Kinetics and Chemical Morphology. *The Journal of Physical Chemistry A* **2005,** *109* (48), 10910-10919.

51.   Hearn, J. D.; Smith, G. D., Ozonolysis of Mixed Oleic Acid/n-Docosane Particles: The Roles of Phase, Morphology, and Metastable States. *The Journal of Physical Chemistry A* **2007,** *111* (43), 11059-11065.

52.   Mendez, M.; Visez, N.; Gosselin, S.; Crenn, V.; Riffault, V.; Petitprez, D., Reactive and Nonreactive Ozone Uptake during Aging of Oleic Acid Particles. *The Journal of Physical Chemistry A* **2014,** *118* (40), 9471-9481.

53.   Wang, M.; Yao, L.; Zheng, J.; Wang, X.; Chen, J.; Yang, X.; Worsnop, D. R.; Donahue, N. M.; Wang, L., Reactions of Atmospheric Particulate Stabilized Criegee Intermediates Lead to High-Molecular-Weight Aerosol Components. *Environmental Science & Technology* **2016,** *50* (11), 5702-5710.

54.   Isaacman, G.; Chan, A. W. H.; Nah, T.; Worton, D. R.; Ruehl, C. R.; Wilson, K. R.; Goldstein, A. H., Heterogeneous OH Oxidation of Motor Oil Particles Causes Selective Depletion of Branched and Less Cyclic Hydrocarbons. *Environmental Science & Technology* **2012,** *46* (19), 10632-10640.

55.   Kolesar, K. R.; Buffaloe, G.; Wilson, K. R.; Cappa, C. D., OH-Initiated Heterogeneous Oxidation of Internally-Mixed Squalane and Secondary Organic Aerosol. *Environmental Science & Technology* **2014,** *48* (6), 3196-3202.

56.   Valsaraj, K. T., A Review of the Aqueous Aerosol Surface Chemistry in the Atmospheric Context. *Open Journal of Physical Chemistry* **2012,** *Vol.02No.01*, 9.

57.   Chen, J.; Ehrenhauser, F. S.; Valsaraj, K. T.; Wornat, M. J., Uptake and UV-Photooxidation of Gas-Phase PAHs on the Surface of Atmospheric Water Films. 1. Naphthalene. *The Journal of Physical Chemistry A* **2006,** *110* (29), 9161-9168.

58.   Chen, J.; Ehrenhauser, F.; Valsaraj, K.; Wornat, M., Adsorption and UV Photooxidation of Gas-Phase Phenanthrene on Atmospheric Films. 2009; Vol. 1005, pp 127-146.

59. Pegram, L. M.; Record, M. T., Using Surface Tension Data to Predict Differences in Surface and Bulk Concentrations of Nonelectrolytes in Water. *The Journal of Physical Chemistry C* **2009,** *113* (6), 2171-2174.

60. Prisle, N. L.; Ottosson, N.; Öhrwall, G.; Söderström, J.; Dal Maso, M.; Björneholm, O., Surface/bulk partitioning and acid/base speciation of aqueous decanoate: direct observations and atmospheric implications. *Atmos. Chem. Phys.* **2012,** *12* (24), 12227-12242.

61. Knipping, E. M.; Lakin, M. J.; Foster, K. L.; Jungwirth, P.; Tobias, D. J.; Gerber, R. B.; Dabdub, D.; Finlayson-Pitts, B. J., Experiments and Simulations of Ion-Enhanced Interfacial Chemistry on Aqueous NaCl Aerosols. *Science* **2000,** *288* (5464), 301-306.

62. Kumar, M.; Zhong, J.; Zeng, X. C.; Francisco, J. S., Reaction of Criegee Intermediate with Nitric Acid at the Air–Water Interface. *Journal of the American Chemical Society* **2018,** *140* (14), 4913-4921.

63. Kolb, C. E.; Worsnop, D. R., Chemistry and Composition of Atmospheric Aerosol Particles. *Annual Review of Physical Chemistry* **2012,** *63* (1), 471-491.

64. Poschl, U.; Shiraiwa, M., Multiphase chemistry at the atmosphere-biosphere interface influencing climate and public health in the anthropocene. *Chem Rev* **2015,** *115* (10), 4440-75.

65. Laskin, A.; Gilles, M. K.; Knopf, D. A.; Wang, B.; China, S., Progress in the Analysis of Complex Atmospheric Particles. *Annual Review of Analytical Chemistry* **2016,** *9* (1), 117-143.

66. Burkholder, J. B.; Abbatt, J. P. D.; Barnes, I.; Roberts, J. M.; Melamed, M. L.; Ammann, M.; Bertram, A. K.; Cappa, C. D.; Carlton, A. G.; Carpenter, L. J.; Crowley, J. N.; Dubowski, Y.; George, C.; Heard, D. E.; Herrmann, H.; Keutsch, F. N.; Kroll, J. H.; McNeill, V. F.; Ng, N. L.; Nizkorodov, S. A.; Orlando, J. J.; Percival, C. J.; Picquet-Varrault, B.; Rudich, Y.; Seakins, P. W.; Surratt, J. D.; Tanimoto, H.; Thornton, J. A.; Tong, Z.; Tyndall, G. S.; Wahner, A.; Weschler, C. J.; Wilson, K. R.; Ziemann, P. J., The Essential Role for Laboratory Studies in Atmospheric Chemistry. *Environmental Science & Technology* **2017,** *51* (5), 2519-2528.

Chapter Two

Experimental Section:

Aerosol Reactor Flow Tube Setup

Chapter 2. Experimental section

2.1 Experimental setup

The study on the OH-initiated heterogeneous oxidation of saccharide aerosol particles are performed in an atmospheric pressure aerosol flow tube with online aerosol mass spectrometric technique and offline Teflon filter collection then analyzed using gas chromatography-mass spectrometry (GC-MS).

2.1.1 VUV-AMS analysis experimental setup

The study on the effect of relative humidity on OH-initiated heterogeneous oxidation of semi-solid monosaccharide aerosol particles (Chapter 3) is investigated using an atmospheric pressure slow flow reactor coupled to an aerosol mass spectrometer at the Chemical Dynamics Beamline at the Advanced Light Source synchrotron. Figure 2.1 displays a schematic of the experimental set up. [1, 2]
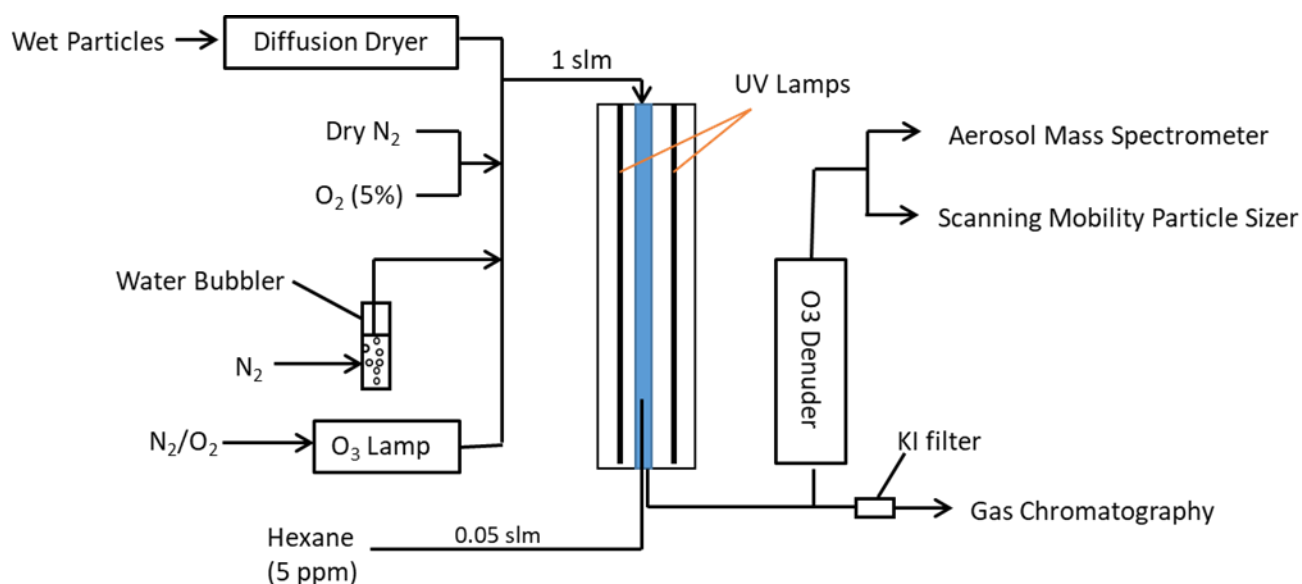
Figure 2. 1 Schematic of the atmospheric pressure flow tube reactor used in the heterogeneous oxidation of semi-solid MGP ($C_7H_{14}O_6$) aerosol particles. MGP ($C_7H_{14}O_6$) particles are generated by Aerosol Atomizer. The aerosol stream is then mixed with humidified N_2, O_2, O_3, and dry N_2. A total of 1 L min^{-1} aerosol stream enters an atmospheric pressure flow tube to react with OH radicals generated by 254 nm photolysis of O_3 in the presence of water vapor. Hexane is injected from bottom 1/6 of the flow tube. Upon exiting the flow tube, OH concentration is measured by

quantifying the loss of hexane tracer using GC-FID. Aerosol stream is analyzed by an Aerosol Mass Spectrometer and by a Scanning Mobility Particle Size (SMPS). The reaction time is 37 s. [1, 2]

Methyl β-D-glucopyranoside (MGP) ($C_7H_{14}O_6$) organic aerosol is formed by nebulizing a 1 mg/ml MGP-aqueous solution using a constant-output atomizer (TSI, Model 3076). The droplets then pass through a room-temperature diffusion dryer (1 meter-length) to remove the water vapor and dry the particles. In the diffusion dryer, the wet aerosol passes through an inner tube, made of wire screen. The silica gel is filled in the annular space between the inner tube and outer wall. The silica gel absorbs the water vapor as the wet aerosol passes through. The resident time in the dryer is about 15 s. The relative humidity in the flow tube is set by flowing a known amount of nitrogen gas through a water bubbler. Ozone is generated by a mercury pen-ray lamp (UVP, LLC) or a commercial corona discharge ozone generator (Ozone Lab Instruments). The amount of ozone is adjusted by the flow rate of molecular oxygen through the ozone generator or by the intensity of the corona discharge. OH radicals are generated along the flow tube by photolysis of ozone in the presence of water by four mercury lamps (λ=254 nm, UVP. LLC). The concentration of OH radical formed is controlled by the amount of ozone. A small amount of hexane gas (5 ppm) is injected to the flow tube in order to measure the OH exposure (the integral of the OH number density over the total reaction time). The wet nitrogen is then mixed with dry nitrogen, ozone, molecular oxygen (5%), trace hexane and the aerosol stream into a type-219 quartz flow tube reactor with an inner diameter of 2.5 cm and a length of 130 cm. The maximum of ozone in the flow tube is 10 ppm. The total sample flow rate entering the flow tube reactor is set to 1 slm (standard litter per minute) corresponding to a total reaction time of 37s.

Upon exciting the reaction flow tube, the aerosol passes through an ozone denuder to remove the gas phase ozone. A fraction of the flow is sent to a Scanning Mobility Particle Sizer (SMPS, TSI, Model 3936) to measure particle size distribution and number concentration. A portion of aerosol flow is sampled into a custom-built time-of-flight aerosol mass spectrometer for particle chemical composition determination by thermally vaporizing the aerosol followed by tunable vacuum-ultraviolet VUV photoionization. The remainder of sample flow is sent to a gas chromatograph (GC) equipped with a flame ionization detector (FID) (SRI model 8610C) for monitoring the loss of hexane. Ozone and particles are removed prior to entering the GC by a potassium iodide (KI) trap and particle filter. The initial hexane concentration entering the flow tube is about 250 ppb. The hexane tracer is injected from the bottom 1/6 of the flow tube through

27

a 1/8-inch I.D. Teflon tube. The OH exposure for the whole flow tube is obtained by injecting hexane first into the top of the flow tube and then separately through the bottom 1/6 of the flow tube at a relatively low O_3 concentration. The correction factor is then applied to all OH exposure measurements. [1, 2]

2.1.1.1 Scanning Mobility Particle Sizer

Scanning Mobility Particle Sizer (SMPS) (TSI Model 3936) system is used in this project. It includes Electrostatic Classifier (TSI Model 3080), which consists of a diffusion charger (Kr-85, Bipolar) and a long Differential Mobility Analyzer (TSI 3081 long-DMA), and Condensation Particle Counter (TSI Model 3775) with butanol as working fluid. The sample inlet flow rate is 0.3 L/min. It takes 120 s to scan one particle size spectrum. This SMPS system achieves efficiency in measuring particle size in the range from 10 to 1000 nanometer in diameter.

2.1.1.1.1 Electrostatic Classifier

When aerosol flows into Electrostatic Classifier, the particles larger than 1000 nm are first removed by the impactor (0.071 cm nozzle). The diffusion charger provides a known charge distribution on the aerosols when they enter the long DMA. Figure 2.2 displays the schematic of the long DMA. The polydisperse aerosol enters the DMA through a 17.468-inch length of tube from the top. The extra aerosol sample exits the DMA through the bypass outlet. The sheath air flows from the bottom to the top of DMA between the central rods. The sheath air flow rate is about 10 time of aerosol sample flow rate. The filter in the top is to remove the particles in the air. Then the particle-free air flows downward the center rods. The two high-voltage rods in the center are positively charged. The positively charged particles are stick to the outer electrodes and neutral particles are removed through the excess air outlet. Only negatively charged particles with a narrow range of electrical mobility exit the DMA through the monodisperse aerosol outlet. Electrical mobility, Z_p, is a ratio between particle charge and particle diameter as defined in the following equation: [3]

$$Z_p = \frac{neC}{3\pi\mu D_p} \tag{1}$$

Where: n is the number of elementary charges on the particle, e is the elementary charge (1.6×10^{-19} Colomb), C is the Cunningham slip correction ($C = 1 + Kn[\alpha + \beta \exp\left(-\frac{\gamma}{Kn}\right)]$, α=1.142, β=0.558, γ=0.999, $Kn = {2\lambda}/{D_p}$, λ is the gas mean free path, $\lambda = \lambda_r(\frac{P_r}{P})(\frac{T}{T_r})(\frac{1+S/T_R}{1+S/T})$, μ is gas viscosity (dyne $\cdot$ s/cm^2) poise ($\mu = \mu_r(\frac{T_r+S}{T+S})\frac{T^{\frac{3}{2}}}{T_r}$, s is the Sutherland constant (K), T is temperature (K), T_r is reference temperature), and D_p is the particle diameter (cm).
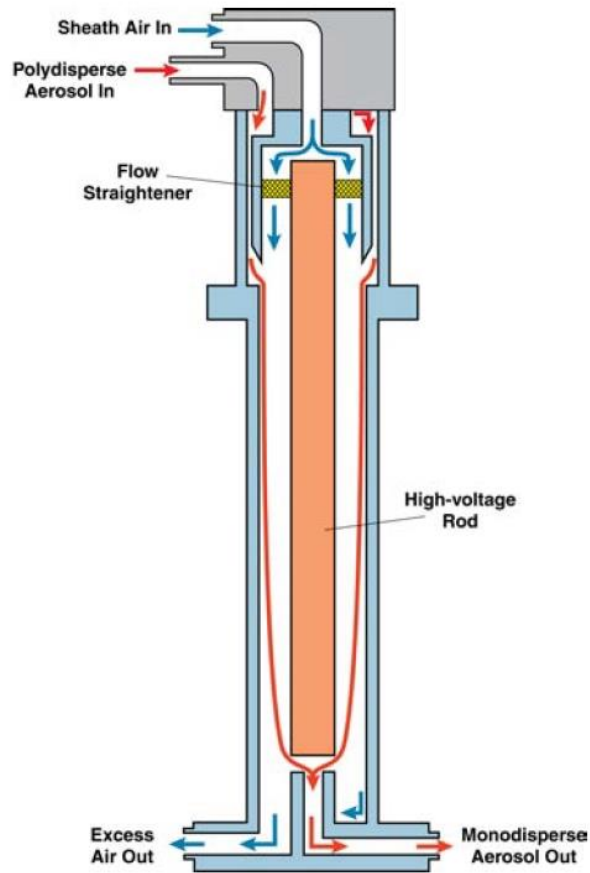
Figure 2. 2 Schematic Diagram of Long DMA. [3]

2.1.1.1.2 Condensation Particle Counter

Condensation Particle Counter (CPC) provides highly accurate measurements of particles concentration. In the CPC, first the particles enter the heated saturator (T=39℃) containing vapors of butanol. The butanol vapors diffuse into the particles stream. Then particles and butanol vapors

together come to the cooled condenser (T=14℃) where the particles serve as condensation nuclei and butanol vapors start to condense on particles. Once the droplets grow to a size between 1 and 10 µm, they can be detected by light scattering. The scattered-light pulses are collected by a photodetector. [3]

2.1.1.1.3 Typical Number distribution of MGP aerosol atomized from 1mg/ml solution

Figure 2.3 shows the SMPS number density distributions as a function of mobility diameter for unreacted MGP ($C_7H_{14}O_6$) particles normalized to the same particle number concentration. The typical surface-weighted mean diameter of the particles is 228±14 nm.
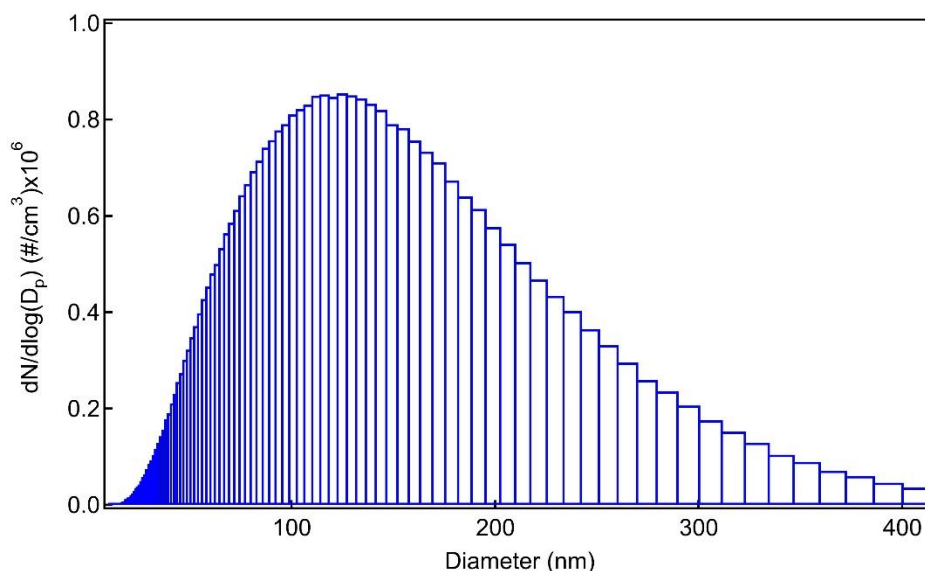
Figure 2. 3 Size distributions for unreacted MGP ($C_7H_{14}O_6$) particles normalized to the same particle concentrations: particle number density concentration as a function of mobility diameter.

2.1.1.2 Aerosol Mass Spectrometer

Aerosol TOF-MS instrument designed and constructed at the Chemical Dynamics Beamline at the Advanced Light Source is used in this project. Figure 2.4 displays schematic of aerosol TOF-MS. The main components of aerosol TOF-MS are: (1) a flow-limiting aerosol inlet which allows particles pass to enter the aerodynamic lens, where particles form a particle beam; (2) vaporization and ionization chamber, where a cartridge heater vaporizes the particles, then the vapors are

ionized by the VUV light produced with synchrotron source; (3) a time-of-flight tube and microchannel plate detector. [4]
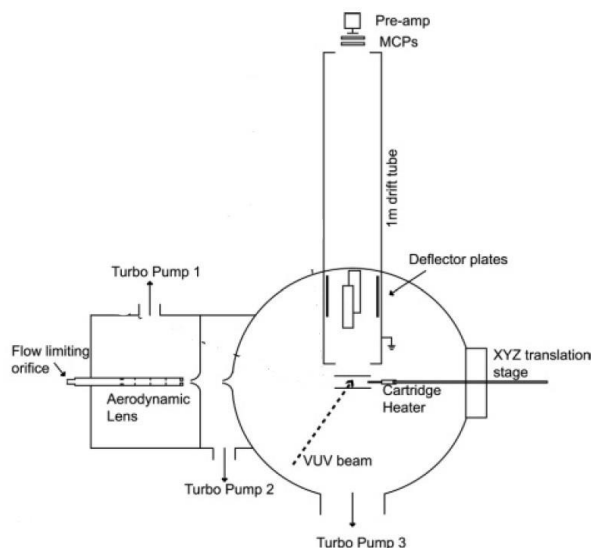
Figure 2. 4 Schematic of aerosol TOF-MS. [4]

2.1.1.2.1 Aerodynamic lens system

Figure 2.5 displays the schematic of aerodynamic lens system. The particles are sampled into the aerosol mass spectrometer through a 200 μm i.d. flow-limiting orifice located at the inlet of a 10-inch-long (1/2 in. o. d., 0.4 in i.d.) stainless steel tube. The aerosol sample flow rate through this inlet orifice is 0.25 L/min and the inlet pressure is 7.50 Torr. As the aerosol particles pass through the aerodynamic lens system, they are focused into a particle beam through the final 3.00 mm nozzle. [4, 5]
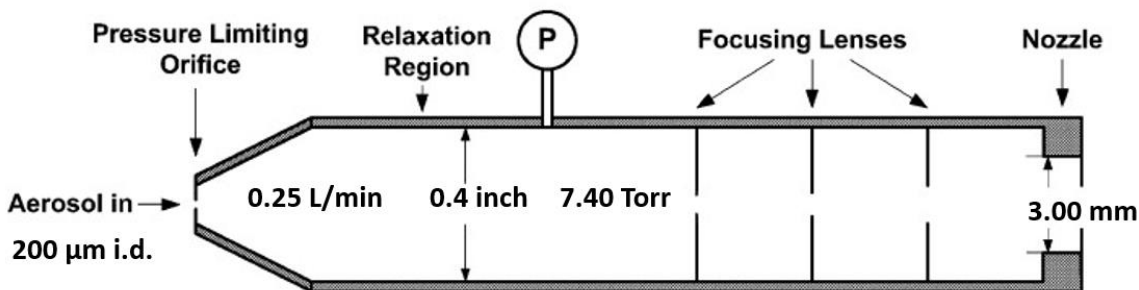
Figure 2. 5 Schematic of the aerodynamic lens system. [4, 5]

2.1.1.2.2 Vaporization and ionization chamber

Figure 2.6 displays the expanded view of vaporization and ionization chamber. When the particle beam exits the aerodynamic lens into vacuum and is accelerated by the gas expansion. Then the particle beam passes through two stages of differential pumping chamber to the ionization region of the main chamber. The pressure in the main chamber is 1.7×10^{-7} Torr. As the particle beam enters the ionization region of the main chamber, it impinges on a cartridge heater with a copper tip. The heater's position is designed with an XYZ translation stage where the copper tip is about 1.5 cm distance away from the center of the ionization region. This distance provides the maximum of vapor density reaching the ionization beam light and minimum interference of electrical filed caused by the copper between the extraction plates. The temperature of the copper tip is set at 423 K and the optical energy of beam light is determined to be 10.5 eV. The resulting ions are spatially separated by time of flight analyzer and detected by the microchannel plate detector. [4]
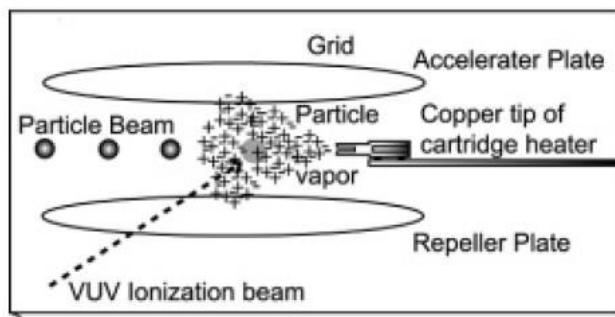
Figure 2. 6 Expanded view of vaporization/ionization chamber. [4]

32

2.1.1.2.3 Aerosol mass spectra of MGP particles

Figure 2.7 shows a typical mass spectrum obtained upon vaporization of unreacted MGP ($C_7H_{14}O_6$) nanoparticles at 10.5 eV using VUV-AMS. The photon energy was selected in order to maximize the ion signal while minimizing the dissociative ionization of the parent molecule. The parent fragment observed in Figure 2.7 is m/z=176, which is corresponding to dissociative ionization by loss of a water molecule. The other fragments indicated in Figure 2.7 are used as tracer of the relative abundance of MGP ($C_7H_{14}O_6$) left in the particle for the online kinetic measurements. [2]
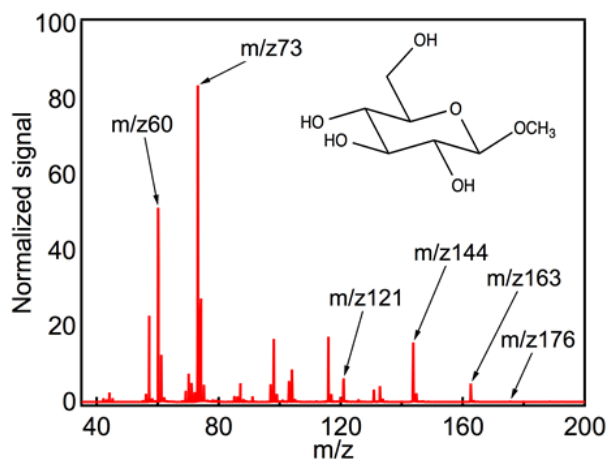
Figure 2. 7 Mass spectrum of unreacted methyl-β-D-glucopyranoside ($C_7H_{14}O_6$) nanoparticles obtained at 10.5 eV. [2]

2.1.1.3 Gas-Phase relative rate measurement

The rate constant for the OH oxidation of MGP ($C_7H_{14}O_6$) semi-solid particles is measured using a mixed-phase relative rate approach. In this case, it is not necessary to measure absolute reaction times or the concentration of OH radicals. [6] Hexane is chosen as the gas-phase reference compound. It is found that more than 99% loss of hexane is due to the reaction with OH radicals. [7] The time dependent decay of hexane due to the reaction with OH radicals is determined using the following equation:

$$\frac{d[Hex]}{dt} = -k_{hex}.[OH].[Hex] \tag{2}$$

Where [hex] and [OH] are the concentration of hexane and OH (molecules cm^{-3}) in the flow tube, respectively. t is the reaction time (s) and k_{hex} is the second-order rate constant (cm^3 molecule^{-1} s^{-1}) for OH+hexane reaction, which is 5.2×10^{-12} cm^3 molecule^{-1} s^{-1}. [8]

The OH exposure is obtained from the ratio of the hexane signal with and without the photolysis lamps using the following the equation:

$$\text{OH exposure} = -\frac{\ln(\frac{[Hex]_t}{[Hex]_0})}{k_{hex}} = \int_0^t [OH]dt = <OH>_t.t \qquad (3)$$

Where $[Hex]_0$ is the initial concentration of hexane entering the flow tube, and $[Hex]_t$ is final concentration of hexane exiting the flow tube after reaction with OH. $<OH>_t$ is the time averaged concentration of OH.

The rate constant for the OH oxidation of MGP ($C_7H_{14}O_6$) particles (k_{rx}) is measured by the loss of particle-phase MGP ($C_7H_{14}O_6$), determined from the AMS spectrum. An expression equivalent to Eqn (2), the time dependence decay of particle-phase MGP ($C_7H_{14}O_6$) loss is as following:

$$\frac{d[MGP]}{dt} = -k_{rx}.[OH].[MGP] \qquad (4)$$

Where k_{rx} (cm^3 molecule^{-1} s^{-1}) is the second-order rate constant for OH oxidation of MGP ($C_7H_{14}O_6$) particles. [MGP] and [OH] are the concentration of MGP ($C_7H_{14}O_6$) and OH (molecules cm^{-3}) in the flow tube, respectively.

From the simultaneous decay of gas-phase reference hexane and particle-phase MGP ($C_7H_{14}O_6$) for the same fixed reaction time, the k_{rx} is obtained through the standard relative rate method:

$$\ln([MGP]_t/[MGP]_0) = k_{rx}[\frac{\ln([Hex]_t/[Hex]_0)}{k_{Hex}}] \qquad (5)$$

Where $[MGP]_t/[MGP]_0$ is the fraction remaining of the particle phase MGP ($C_7H_{14}O_6$) after a given amount of reaction time, $[Hex]_t/[Hex]_0$ is the fraction of the gas-phase reference hexane remaining after reaction.

It is more convenient for the kinetic analysis to derive the exponential form by substitute Eqn (3) into Eqn (5) as following:

$$\frac{[MGP]_t}{[MGP]_0} = \exp(- k_{rx} < OH >_t . t) \tag{6}$$

The observed MGP ($C_7H_{14}O_6$) disappearance rate constants (k_{rx}) can be determined from an exponential fit by plotting $[MGP]_t/[MGP]_0$ versus $< OH >_t . t$.

2.1.1.4 Aerosol reactive uptake measurement

The rate constant for gas-particles reaction is measured by the loss of particle-phase species. The kinetic of reaction in the particle phase depends on many factors, such as particle size and particle shape. Therefore, it is often more useful to describe the efficiency of the heterogeneous reaction in terms of a reactive uptake coefficient, γ_{eff}. A reactive uptake coefficient (γ_{eff}) is defined as a fraction of OH-particle collisions which yield a reactive loss of a reactant molecule in the particle phase. Here it has been assumed that the particle is spherical and well mixed on the timescale of the reaction. Using this definition of γ_{eff}, the organic particle species reaction rate ($\frac{d[Org]}{dt}$) is,

$$\frac{d[Org]}{dt} = -\gamma_{eff} . f . J_{coll} . C_p . A \tag{7}$$

where f is the fraction of particle molecules remaining in the particle (i.e. $[Org]/[Org]_0$) and depends on the extent of reaction. J_{coll} is the OH flux at the particle surface, C_p is the particle number density, and A is the particle surface. Eqn (7) can be solved for γ_{OH}^{Org} by substituting $d[Org]/dt = -k_{rx} . [Org] . [OH], f = [Org]/[Org]_0, J_{coll} = c . [OH]/4$ to obtain,

$$\gamma_{eff} = \frac{k_{rx} . [Org] . [OH]}{f . J_{coll} . A . C_p} = \frac{4 . k_{rx} . [Org]_0}{c . A . C_p} \tag{8}$$

Where k_{rx} is the second order rate constant for the reaction of particle species with OH from Eqn (6), $[Org]_0$ is a spatially averaged concentration (molecules cm^{-3}),

$$[Org]_0 = \frac{C_P . V . \rho_0 . N_A}{M} \tag{9}$$

Where V is the particle volume, M is the molar mass of particle species, N_A is the Avogadro's number, and ρ_0 is the initial particle-phase density. Eqn (8) can be further simplified by the following expression: [1]

$$r_{eff} = \frac{2k_{rx}d_p\rho_0 N_A}{3cM} \tag{10}$$

Here d_p is the mean surface-weighted particle diameter. Note that if the value of r_{eff} is greater than 1, it indicates that there is a secondary loss processes for the particle species after the initial reaction with OH radical. Since the uncertainties in the measurements of k_{rx} (δk_{rx}) and d_p (δd_p) are independent, the uncertainty in r_{eff} (δr_{eff}) is given by:

$$\frac{\delta r_{eff}}{|r_{eff}|} = \sqrt{(\frac{\delta k_{rx}}{k_{rx}})^2 + (\frac{\delta d_p}{d_p})^2} \tag{11}$$

2.1.2 GC-MS analysis experimental setup

The studies presented in Chapters 4 and 5 were performed with an offline detection technique. The experiments are performed using an atmospheric pressure aerosol flow tube coupled with Scanning Mobility Particle Sizer (SMPS), Gas Chromatography-Flame Ionization Detector (GC-FID) and Teflon filter collection. Figure 2.8 displays the details of the experimental set up. [9, 10]
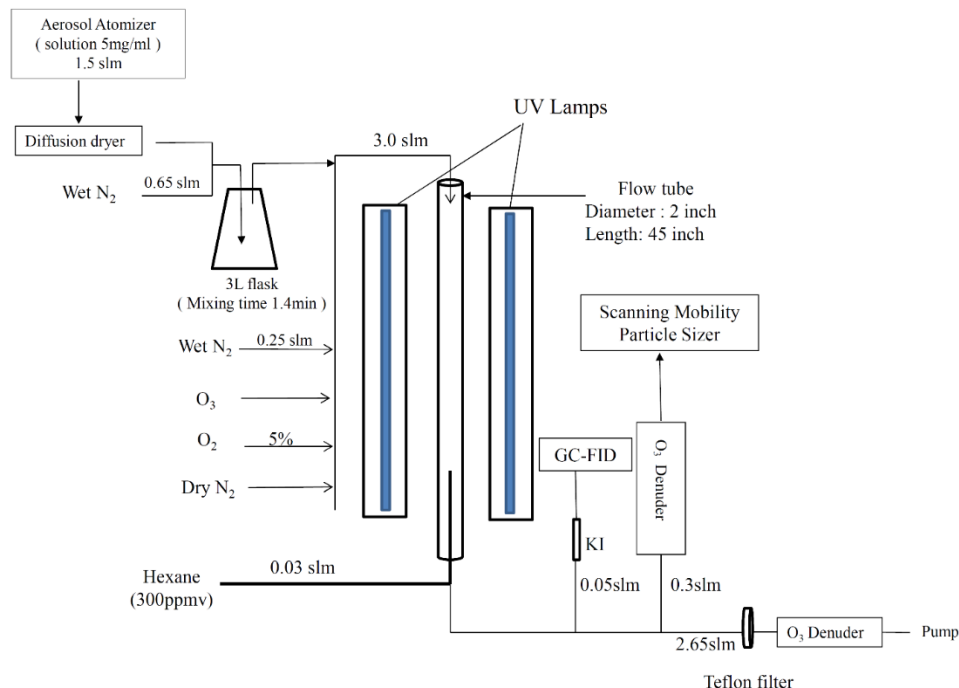
Figure 2. 8 Schematic of the flow reactor used in off-line kinetic measurement experiments. Saccharide particles are generated by Aerosol Atomizer. The aerosol stream is then mixed with humidified N_2, O_2, O_3, and dry N_2. A total of 3 L min^{-1} aerosol stream enters an atmospheric pressure flow tube to react with OH radicals generated by 254 nm photolysis of O_3 in the presence of water vapor. Hexane is injected from bottom 1/5 of the flow tube. Upon exiting the flow tube, OH concentration is measured by quantifying the loss of hexane tracer using GC-FID. Aerosol stream is analyzed by a Scanning Mobility Particle Sizer (SMPS) and is collected by Teflon filter. The reaction time is 46 s. [9]

The saccharides particles are generated by nebulizing a 5 mg/ml saccharides aqueous solution using a constant output atomizer (TSI, model3076) with a 1.5 L min^{-1} N_2 flow. For semisolid particles studies, the aerosol flow (1.5 L min^{-1}) passes through a room-temperature diffusion dryer to dry the particles and remove the excess water vapor. The diffusion dryer is a 47-inch long PTFE Teflon tube with a 3-inch inner diameter (I.D.) filled with Drierite Desiccant ($\geq$ 98% $CaSO_4$, <2% $CoCl_2$). A 1/2-inch I.D. wire screen tube allows the aerosol flow to pass through the dryer with a residence time of 6 s. At the exit of the dryer, the 1.5 L min^{-1} dry particle stream is mixed with a 0.65 L min^{-1} flow of wet N_2 into a 3 L Erlenmeyer flask with an estimated residence time of 84 s. For liquid nanodroplets study, the diffusion dryer is removed and the wet aerosol is directly mixed with the wet N_2 in the 3 L Erlenmeyer flask. The wet N_2 flow is obtained by bubbling pure N_2 into water. The relative humidity is fixed at 30% with humidified N_2 after which

37

another 0.25 L min^{-1} wet N$_2$, 0.15 L min^{-1} O$_2$ (5%), variable amounts of O$_3$, and Dry N$_2$ are added into the wet aerosol stream in order to obtain a total flow of 3 L min^{-1}. The ratio of total humidified N$_2$ over total aerosol sample flowrate is always 0.3. The resulting flow is then injected into a 45-inch long and 2-inch I.D. quartz tube surrounded by three UV lamps (UVP, λ_{mean}=254 nm). With a total flow through the flow tube of 3 L min^{-1}, the resident time is of the order of 46 s.

Ozone is generated either by passing a 1.0 L min^{-1} O$_2$ flow through an ozone generator (AC-500G, Ozone Solutions, 0.87 g/hr) or by passing a 5.66 L min^{-1} O$_2$ through a corona discharge ozone generator (CD2000P, ClearWater Tech, LLC., 27 g/hr). The O$_3$ concentration in the flow tube is varied by the O$_3$ flow rate. For the semisolid particle studies, the maximum amount of the O$_3$ in the flow tube is estimated to be 5 ppm. For the liquid nanodroplets study, the maximum amount of the O$_3$ in the flow tube is around 0.48 ppm. The OH radicals are generated by photolysis of ozone in the presence of water vapor. The amount of OH radicals can be varied either by controlling the concentration of ozone in the flow tube or by the number of UV lamps turned on.

The hexane is chosen as a gas-phase reference compound to quantify the average OH concentration. The initial hexane concentration entering the flow tube is 3 ppm. The hexane tracer is injected from the bottom 1/5 of the flow tube through a 1/8-inch I.D. Teflon tube. The OH exposure for the whole flow tube is obtained by injecting hexane first into the top of the flow tube and then separately through the bottom 1/5 of the flow tube at a relatively low O$_3$ concentration. [1] The correction factor is then applied to all OH exposure measurements. The decay of the relative hexane concentration is monitored by gas chromatography coupled to a flame ionization detector (FID) (Thermo Scientific Trace GC 2000). The gas is sampled onto the capillary column (phase ZB-5, 30 m × 0.32 mm I.D. and film thickness of 0.5 μFT, phenomenex) using a six-port valve. Helium is used as carrier gas at a flow rate of 5.0 mL min^{-1}. The injection temperature and the FID detector temperature are 250℃ and 300℃, respectively. The oven temperature is isothermally set at 50°C for the 5 min runs.

Upon exiting the flow tube, a 0.3 L min^{-1} of the total flow passes through an ozone denuder and is sent to a scanning mobility particle sizer (SMPS) (TSI, model 3936) for particle size distributions and concentration measurements. The typical surface-weighted mean diameter of the particles is about 350 nm. Another 0.05 L min^{-1} of the reacted flow passes through a packed potassium iodide tube to remove O$_3$ before reaching the GC-FID for hexane measurement. The

remaining of the particle flow 2.65 L min^{-1} passes through a PTFE (polytetrafluoroethylene) filter (Millipore FALP, 1.0 um, diameter 47mm). The collection is performed for 30 mins in order to collect about 1mg of saccharides particles.

Following the particle collection, the PTFE filter is sonicated twice for 15 min in a 10 mL mixture of ethanol: distilled water (1:1, v:v) together with 1 mg of internal standard xylose at room temperature. The combined (20 mL) extract aliquots are concentrated by rotary evaporation to about 10 mL. The remaining water solvent is removed by freeze drying with a Freeze Dryer (FreeZone 2.5 Plus, LABCONCO). Silylating reagent (1 mL) (pyridine: sylon BTZ (2:1, v:v) is added to the freeze-dried residue and allowed to react for 3 hour at room temperature.

The silylated mixtures are analyzed using a Trace 1310 Gas chromatograph interfaced with a Single Quadrupole Mass Spectrometer (GC-MS, Thermo Scientific). A capillary column (TG-SQC, 15 m × 0.25 mm I.D. and film thickness of 0.25 μm, Thermo Scientific) is used with helium as the carrier gas at a constant flow rate of 1.0 mL min^{-1}. The MS transfer line and ion source are maintained at 275 and 300 °C, respectively. The scan range is set from 50 to 650 Da at 0.2 scan s^{-1}. The column temperature is programed to increase from 40 °C to 160 °C at a rate of 30 °C min^{-1}, from 160 °C to 170°C at a rate of 2 °C min^{-1}, to 300 °C at a rate of 30 °C min^{-1}, followed by an isothermal hold at 300 °C for 2 min. The total running time is 16 min. All the samples are injected in triplicate for the quantification analysis.

References:

1.   Smith, J. D.; Kroll, J. H.; Cappa, C. D.; Che, D. L.; Liu, C. L.; Ahmed, M.; Leone, S. R.; Worsnop, D. R.; Wilson, K. R., The heterogeneous reaction of hydroxyl radicals with sub-micron squalane particles: a model system for understanding the oxidative aging of ambient aerosols. *Atmos. Chem. Phys.* **2009,** *9* (9), 3209-3222.

2.   Fan, H.; Tinsley, M. R.; Goulay, F., Effect of Relative Humidity on the OH-Initiated Heterogeneous Oxidation of Monosaccharide Nanoparticles. *The Journal of Physical Chemistry A* **2015,** *119* (45), 11182-11190.

3.   Classifiers, E., Series 3080 electrostatic classifiers operation and service manual. P/N 1933792, Revision J. TSI, Ed. 2009.

4.   Mysak, E. R.; Wilson, K. R.; Jimenez-Cruz, M.; Ahmed, M.; Baer, T., Synchrotron Radiation Based Aerosol Time-of-Flight Mass Spectrometry for Organic Constituents. *Analytical Chemistry* **2005,** *77* (18), 5953-5960.

5.   Liu, P.; Ziemann, P. J.; Kittelson, D. B.; McMurry, P. H., Generating Particle Beams of Controlled Dimensions and Divergence: I. Theory of Particle Motion in Aerodynamic Lenses and Nozzle Expansions. *Aerosol Science and Technology* **1995,** *22* (3), 293-313.

6.   Hearn, J. D.; Smith, G. D., A mixed-phase relative rates technique for measuring aerosol reaction kinetics. *Geophysical Research Letters* **2006,** *33* (17).

7.   Atkinson, R.; Baulch, D. L.; Cox, R. A.; Crowley, J. N.; Hampson, R. F.; Hynes, R. G.; Jenkin, M. E.; Rossi, M. J.; Troe, J., Evaluated kinetic and photochemical data for atmospheric chemistry: Volume I - gas phase reactions of Ox, HOx, NOx and SOx species. *Atmos. Chem. Phys.* **2004,** *4* (6), 1461-1738.

8.   Atkinson, R., Kinetics of the gas-phase reactions of OH radicals with alkanes and cycloalkanes. *Atmos. Chem. Phys.* **2003,** *3* (6), 2233-2307.

9.   Fan, H. and. Goulay, F., Effect of bulk composition on the diffusion properties of saccharide aerosols. (In Preparation).

10.   Fan, H.; Wenyika Masaya, T.; Goulay, F., Effect of surface–bulk partitioning on the heterogeneous oxidation of aqueous saccharide aerosols. *Physical Chemistry Chemical Physics* **2019,** *21* (6), 2992-3001.

Chapter Three

Effect of Relative Humidity on the OH-Initiated Heterogeneous Oxidation of Monosaccharide Aerosol

Chapter 3: Effect of relative humidity on the OH-initiated heterogeneous oxidation of monosaccharide aerosol

The present experimental study investigates the effect of relative humidity on the decay of β-methylglucopyranoside (MGP, $C_7H_{14}O_6$), by measuring the relative reactant number density as a function of OH exposure (time-integrated total concentration of OH radical). The kinetics are observed for relative humidity ranging from 10% to 30%. A simple reaction-diffusion model was developed to investigate the effect of variations in diffusion coefficient on the chemical behavior. The model includes the reaction and diffusion of OH, monosaccharide molecules in the semi-solid phase with different initial conditions. The model parameters are extracted from literature data when available. The experimental findings, supported by the modeling results, are discussed toward a better understanding of the role of molecular diffusion on the chemical reactivity of semi-solid materials and their implications for chemical transformation in atmospheric semi-solid particles.

3.1 Experimental results

3.1.1 Kinetic results

Figure 3.1 displays the relative abundance of unreactive MGP ($C_7H_{14}O_6$) in the particle phase as a function of OH exposure at a 30% relative humidity. The experimental points (red solid circles) in Figure 3.1 (b) are the average value of five different tracer masses shown in Figure 3.1 (a). The experimental data reported for a relative humidity at 30% in Figure 3.1 (b) are from two independent data sets. The error bars are two standard deviations about the mean value. The experimental decay of MGP ($C_7H_{14}O_6$) is an initial fast decay at low OH exposure followed by a slower decay at high OH exposure. The thick red line in Figure 3.1 (b) is an exponential fit to the experimental data up to an OH exposure of 0.5×10^{12} cm^{-3} s and extrapolated to higher OH exposure. The second order rate constant with two standard deviation error bars about the mean value for the OH oxidation of MPG ($C_7H_{14}O_6$) particles is obtained from the exponential fit, which is $(1.62\pm0.04) \times10^{-12}$ cm^3 s^{-1}. There is an apparent offset between the experimental data and exponential fit at OH exposure higher than 1.5×10^{12} cm^{-3} s: these tracer masses as shown in Figure 3.1 (a) do not appear to decay to zero. Possible reasons for this apparent offset have been suggested: there is signal interference from product compounds at the chosen tracer mass and

unreacted reactants in the core of particles with a slow mass transfer rate. [1] As shown in the Figure 3.1 (a), the decay rate of MGP ($C_7H_{14}O_6$) is found to be independent on the tracer mass fragments. This confirms that the observed MGP ($C_7H_{14}O_6$) decay behavior is not due to the interference of product signal at the same chosen mass fragment peak.
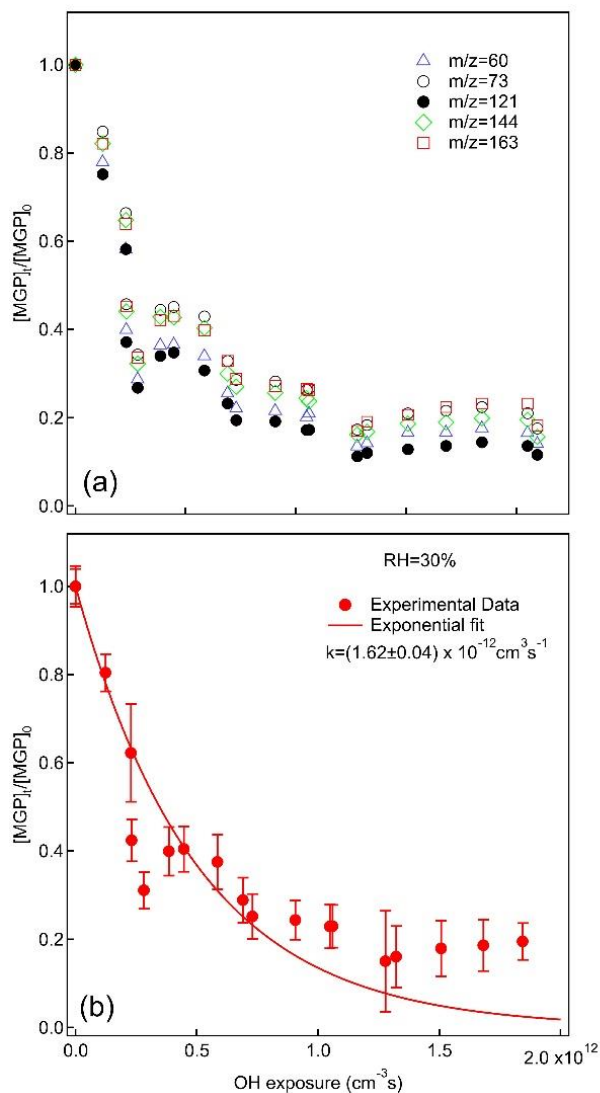
Figure 3. 1 Relative signal of unreacted MGP ($C_7H_{14}O_6$) left in the particle phase as a function of OH exposure obtained (a) for mass fragments at m/z=60 (blue triangles), 73 (black open circles), 121 (black filled circles), 144 (green diamonds), and 163 (red squares) and (b) by averaging the ion signal at five different masses. The error bars in (b) are two standard deviations about the mean value. The red line is obtained by fitting the experimental data up to 0.5×10^{12} cm^{-3} s with an exponential function and extrapolated to higher OH exposure.

Figure 3.2 displays relative unreactive MGP ($C_7H_{14}O_6$) in the particle as a function of OH exposure for 5% O_2 (red solid circles) and 15% O_2 (green solid triangles) in the gas phase at relative humidity of 30%. The decay rate of MGP ($C_7H_{14}O_6$) is found to be independent on the gas phase molecular oxygen concentration. The second order rate constant for the OH oxidation of MGP ($C_7H_{14}O_6$) at 15% O_2 is obtained by fitting an exponential function to the experimental data up to an OH exposure of 0.5×10^{12} cm^{-3} s. The rate constants and uptake coefficients obtained from fit to the data are shown in Table 3.1.
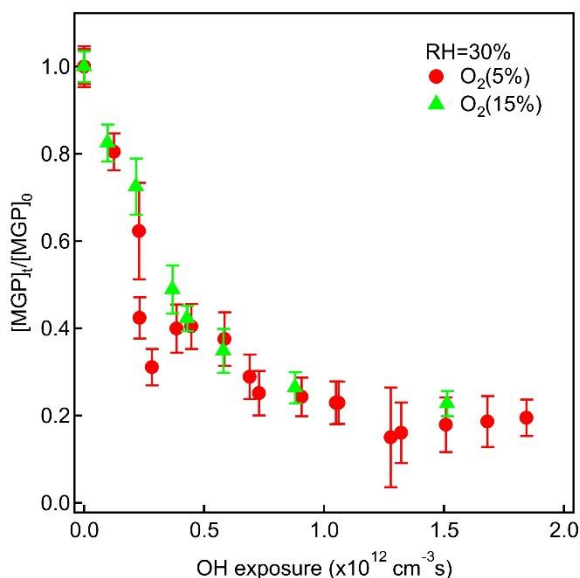
Figure 3. 2 Relative signal of unreacted MGP ($C_7H_{14}O_6$) in the particle phase as a function of OH exposure obtained for 5% O_2 (red solid circles) and 15% O_2 (green solid triangles) at relative humidity of 30%. The experimental points are averaging the ion signal at five different masses. The error bars are two standard deviations about the mean value.

Figure 3.3 displays the relative abundance of MGP ($C_7H_{14}O_6$) in the particle phase as a function of OH exposure for different relative humidity. They are 10% RH (blue solid diamonds), 20% RH (black solid squares) and 30% RH (red solid circles). The decay rate of MPG ($C_7H_{14}O_6$) is found to be relative-humidity dependent. All three decay traces of MGP ($C_7H_{14}O_6$) display a similar behavior: an initial fast decay at low OH exposure and a slower decay at high OH exposure. The observed MGP ($C_7H_{14}O_6$) disappearance rate constants (k_{MGP}) are determined from by fitting the initial part of experimental data up to an OH exposure of 0.5×10^{12} cm^{-3} s to an exponential function. The observed decay rate coefficient of MGP ($C_7H_{14}O_6$) is increased as the relative humidity is increased. The corresponding reactive uptake coefficients at low OH exposure are

0.76±0.14 for RH=10%, 1.34±0.39 for RH=20% and 1.83±0.09 for RH=30%. This suggests that water play a significant role during the heterogeneous oxidation reaction. The fraction of unreacted MGP ($C_7H_{14}O_6$) remaining in the particle are 10% for RH=30%, 40% for RH=20% and 60% for RH=10% at an OH exposure of 1.8×10^{12} cm^{-3} s. The rate constants and uptake coefficients obtained from fit to the data are shown in Table 3.1.

Table 3. 1 Rate constants and reactive uptake coefficients for heterogeneous oxidation of pure MGP ($C_7H_{14}O_6$) nanoparticles at different relative humidity with OH radicals.

Relative Humidity (RH %)	Rate constant $k_{MGP} \pm 2\sigma$ (cm s^{-1})	Uptake coefficient ($\gamma_{MGP} \pm 2\sigma$)
10% (5% O_2)	$6.73 \pm 0.06 \times 10^{-13}$	0.76 ± 0.14
20% (5% O_2)	$1.19 \pm 0.17 \times 10^{-12}$	1.34 ± 0.39
30% (5% O_2)	$1.62 \pm 0.04 \times 10^{-12}$	1.83 ± 0.09
30% (15% O_2)	$1.85 \pm 0.15 \times 10^{-12}$	2.09 ± 0.18
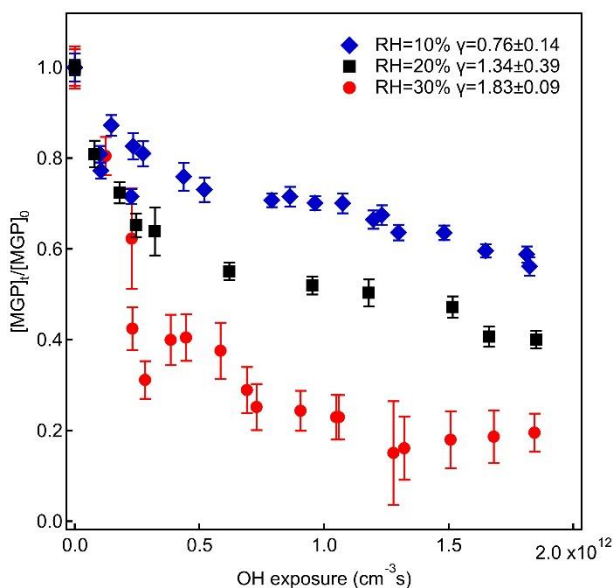
Figure 3. 3 Relative unreactive signal of MGP ($C_7H_{14}O_6$) as a function of OH exposure for RH=10 % (blue solid diamonds), RH=20% (black solid squares), and RH=30% (red solid circles). The error bars are 2 standard deviations about mean value by averaging the signal of five different fragments. The reactive uptake coefficients (γ) are obtained from an exponential fit of the data up to OH exposure of 1.8×10^{12} cm^{-3} s.

3.1.2 Evolution of particle size characterization

Figure 3.4 displays the absolute surface-weighted diameter (nm) as a function of OH exposure for 10% (blue open diamonds), 20% (black open squares) and 30% (red open circles) relative humidity from Scanning Mobility Particle Sizer (SMPS) measurement. The error bars are two standard deviations about triple time particle size data measurement. The typical surface-weighted mean diameter of the particles is 228 ± 14 nm ($\pm2\sigma$) for this study. There is almost no change on surface-weighted mean diameter for RH=10% and RH=20%. There is about 10 nm particle diameter size reduced for RH=30% up to high OH exposure of 1.8×10^{12} cm^{-3} s. The particle size reduction is more likely to be due to the vaporization of volatile organic products.

Figure 3.5 displays (a) total mass concentration (μg/m^3) (b) total number concentration (#/cm^3) and (c) the relative mass abundance of the MPG ($C_7H_{14}O_6$) reactant in one single particle as a function of OH exposure for 10% (blue solid circles), 20% (black solid circles) and 30% (red solid circles) relative humidity. All these data are measured by Scanning Mobility Particle Sizer. The error bars are two standard deviations about triple time particle size data collection. In the panel (c), the relative mass fraction remaining in single particle is a ratio of total mass concentration/total number concentration between reacted and unreacted MGP ($C_7H_{14}O_6$) nanoparticles.

$$\text{Relative mass fraction remainning in single particle} = \frac{[total\ mass]_t/[total\ number\ concentratiion]_t}{[total\ mass]_0/[total\ number\ concentration]_0} \quad (1)$$

where $[total\ mass]_t/[total\ number\ concentratiion]_t$ is one single particle mass is after a given amount of reaction time, $[total\ mass]_0/[total\ number\ concentration]_0$ is one single particle mass before reaction.
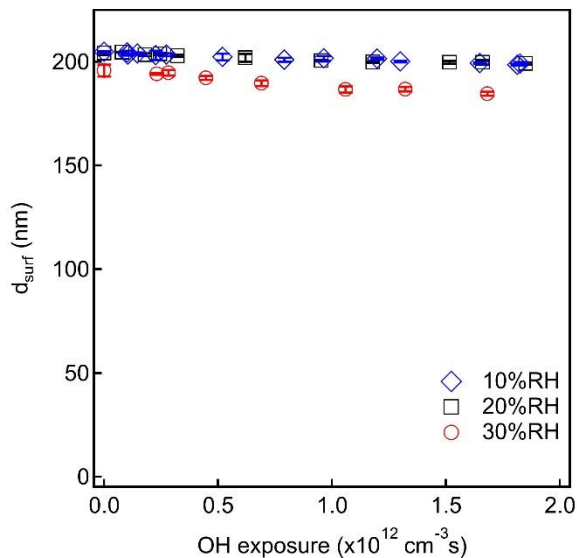
Figure 3. 4 Absolute surface weighted diameter as a function of OH exposure for RH=10% (blue open diamonds), RH=20% (black open squares) and RH=30% (red open circles).

In panel (a), the decay rates of the total mass concentrations (μg/m^3) are almost the same at low OH exposure (up to 2.5×10^{11} cm^{-3} s). The total mass concentrations are reduced by about 30% for RH=10%, RH=20% and 40% for RH=30% up to higher OH exposure of 1.9×10^{12} cm^{-3} s. In panel (b), the decay behaviors of the total number concentrations (#/cm^3) are similar for all different relative humidity studies. The total number concentrations are reduced by about 20% for RH=10%, RH=20% and RH=30% up to higher OH exposure of 1.9×10^{12} cm^{-3} s. In panel (c), the decay behaviors of the relative mass fraction remaining in single particle are similar to those of total mass concentration in panel (a), the relative mass fraction remaining in single particle are reduced 15% for both RH=10%, RH=20%, and 25% for RH=30%.
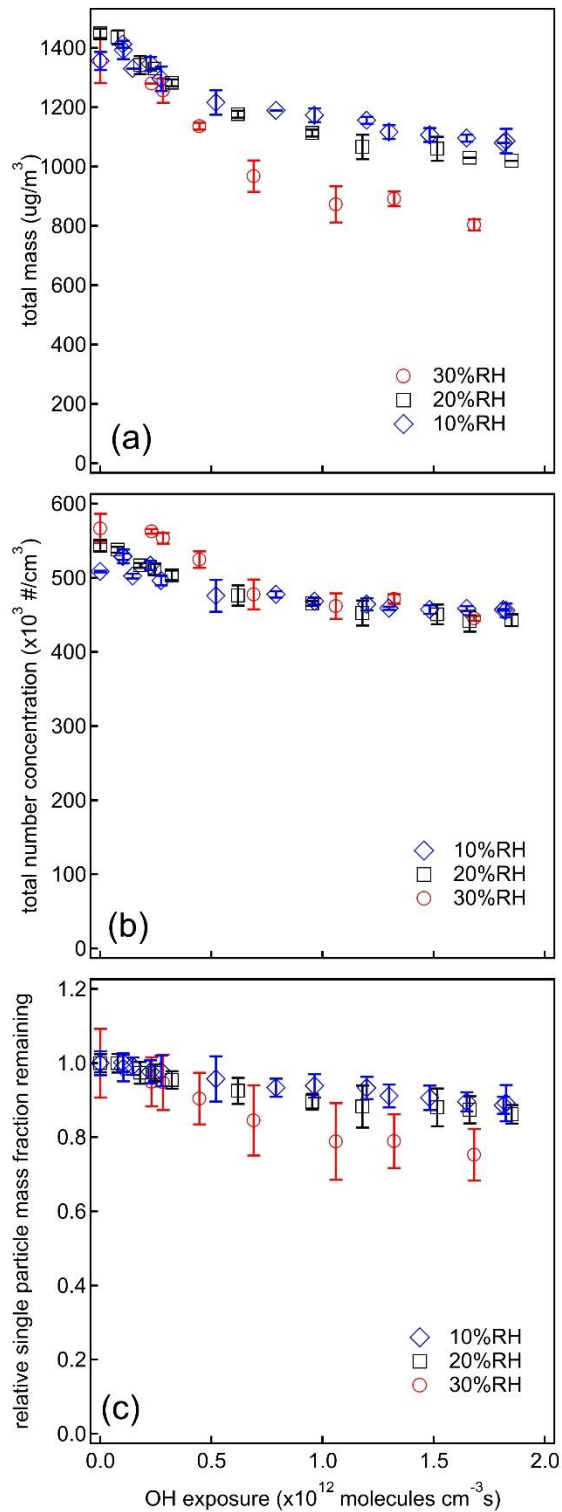
Figure 3. 5 (a) Absolute total mass concentration (μg/m^3) (b) absolute total number concentration (molecules/cm^3) (c) relative single particle mass fraction remaining as a function of OH exposure for RH=10% (blue open diamonds),

RH=20% (black open squares) and RH=30% (red open circles). The error bars are two standard deviations about three set of data collection.

3.1.3 Product results

Figure 3.6 shows that the aerosol mass spectrum of the (a) unreacted MGP ($C_7H_{14}O_6$) nanoparticles and (b) reacted MGP ($C_7H_{14}O_6$) nanoparticles over the 30 to 180 m/z range. In panel (b) the reacted MGP ($C_7H_{14}O_6$) nanoparticles aerosol mass spectrum is obtained at OH exposure of 0.4×10^{12} cm^{-3} s for 30% relative humidity. Small peaks are observed in addition to the fragment peaks of the MGP ($C_7H_{14}O_6$) molecule. These new signals are likely to be due to the fragmentation of the products upon on soft ionization, as detected for highly oxidized molecules. [2, 3] No signal is overserved at masses higher than that of the MGP ($C_7H_{14}O_6$) parent ion peak. This suggests that fragmentation chain reactions dominate the bulk reaction mechanism.
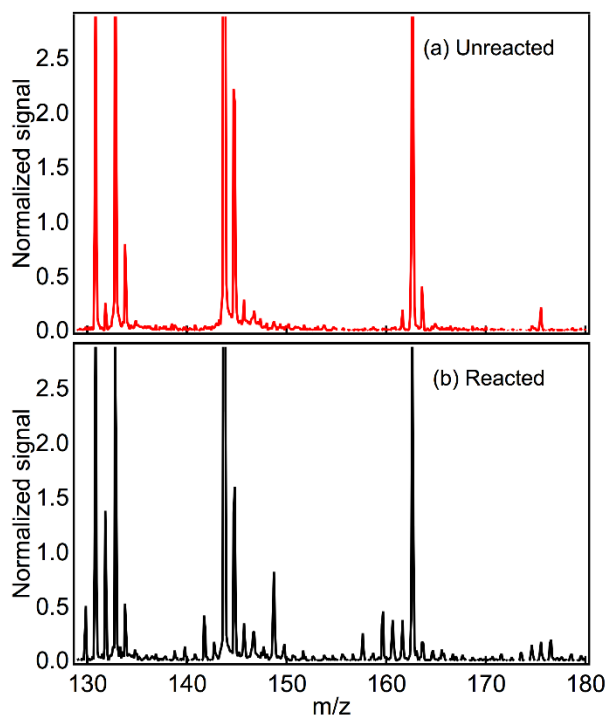
Figure 3. 6 Aerosol mass spectrum of MGP ($C_7H_{14}O_6$) nanoparticles obtained at 10.5 eV for (a) unreacted (red) and (b) reacted (black) samples over the 130 to 180 m/z range. The reacted sample is obtained for an OH exposure of 0.4×10^{12} cm^{-3} s and RH=30%.

Figure 3.7 shows the normalized signal of products ions at (a) m/z=77, (b) m/z=102, and (c) m/z=142 as a function of OH exposure for RH=10 % (blue squares), RH=20% (red triangles), and RH=30% (black circles). All the product signals reach a maximum at OH exposure less than that of 2.5×10^{11} cm^{-3} s. The OH exposure is almost twice smaller than that observed for reactant decay in Figure 3.3, where the OH exposure is at 5.0×10^{11} cm^{-3} s. In addition, the rise of products is found to be independent on the relative humidity. The following slower products decay is independent on relative humidity as well. This suggests that the presence of products in the bulk after reaching a maximum does not affect the decay rate of MGP ($C_7H_{14}O_6$) reactant in the particle. No evidence of secondary product formation is observed in this study.
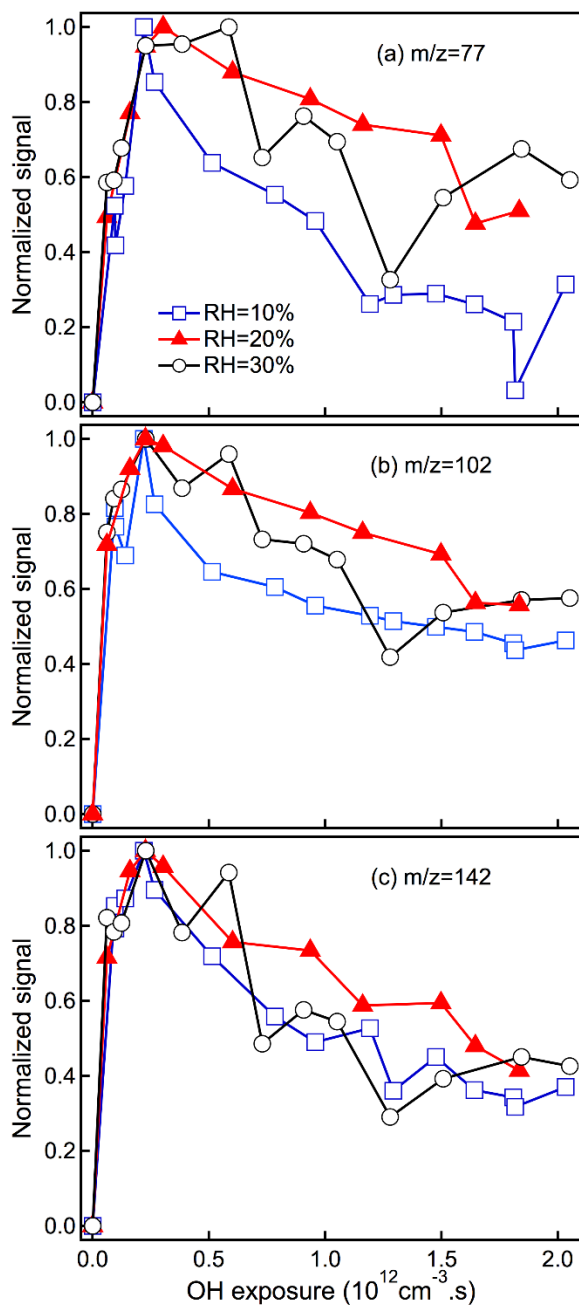
Figure 3. 7 Relative signal of the products detected in the bulk at (a) m/z=77, (b) m/z=102, and (c) m/z=142 as a function of OH exposure for RH=10 % (blue squares), RH=20% (red triangles), and RH=30% (black circles).

3.2 Modeling of the reactant diffusion and reaction

A simple reaction-diffusion kinetic model is developed in order to investigate the impact of bulk molecule diffusion on heterogeneous reaction behaviors. The reaction-diffusion equations couple

the reaction and diffusion of OH and MGP ($C_7H_{14}O_6$) in the particle. The coupled partial differential equations are solved using numerical solver pdepe in Matlab software. This approach makes possible to calculate the concentration of OH and MGP ($C_7H_{14}O_6$) as a function of time and position within the particle. In the model, the chemical reaction is limited by the diffusion of bulk molecule MGP ($C_7H_{14}O_6$) to the particle surface. The diffusive timescale of the MGP ($C_7H_{14}O_6$) reactant is relatively slow compared to the timescale of the MGP ($C_7H_{14}O_6$) and OH chemical reactions. The simulation results are capable to reproduce the observed experimental trends. [4, 5]

3.2.1 Reaction-Diffusion model overview

The OH concentration at the particle surface is modeled using a multistep uptake mechanism: [6]

$$OH_g + site_{MGP} \xrightarrow{k_{ad}} OH_{ad-MGP} \qquad \text{(R1)}$$

$$OH_{ad-MGP} \xrightarrow{k_{des}} OH_g + site_{MGP} \qquad \text{(R2)}$$

$$OH_{ad-MGP} + MGP \xrightarrow{k_{OH+MGP}} Product + H_2O + site_{MGP} \qquad \text{(R3)}$$
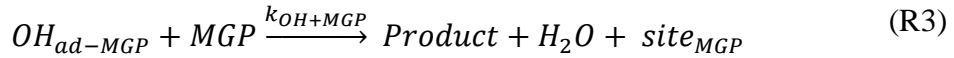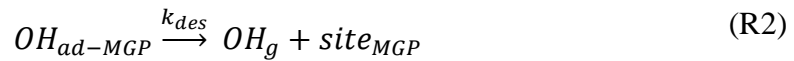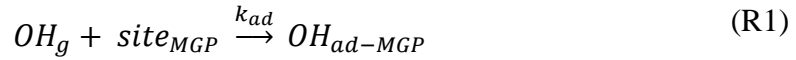
where k_{ad} is the pseudo-first order rate coefficient of adsorption (10 s^{-1}), [6] k_{des} is the rate coefficient of desorption (2.86×10^{10} s^{-1}). [7] k_{OH+MGP}, the rate coefficient for OH reacting with MGP ($C_7H_{14}O_6$) in aqueous solution is 5.31×10^{-12} cm^3 s^{-1}. [8] The above multiple steps describe the following microscopic process: first, the OH radicals in the gas phase must adsorb onto a surface site. Site is one per MGP ($C_7H_{14}O_6$) on the surface of the particle. After adsorption, the OH radicals either desorb back into the gas phase or react by abstracting a hydrogen atom from MPG ($C_7H_{14}O_6$) which produce a water and another surface site. Overall the surface site is constant through the heterogeneous oxidation reaction. Therefore, the OH radical concentration adsorbed onto the particle surface is uniform which is governed by the rate coefficients for adsorption (k_{ad}) and desorption (k_{des}). The experimental average OH concentration is 5.40×10^{10} molecules cm^{-3}. The concentration of bulk MGP ($C_7H_{14}O_6$) is assumed to be radially homogenous before the reaction, which is 4.53×10^{21} molecules cm^{-3}. The diffusion coefficient of OH radical in the particle phase (D_{OH}) is set to 1×10^{-9} cm^2 s^{-1}, which is sufficiently small so that it does not significantly penetrate into the particle. Each particle is assumed to be spherical symmetry with a radius of 100 nm. The reaction-diffusion equations written using spherical polar coordinates are as follows: [7, 9]

$$\frac{\partial [OH]_{ad-MGP}}{\partial t} = \frac{D_{OH}}{r^2}\frac{\partial}{\partial r}\left(r^2\frac{\partial [OH]_{ad-MGP}}{\partial r}\right) - k_{OH+MGP}[OH]_{ad-MGP}[MGP] \qquad (2)$$

$$\frac{\partial [MGP]}{\partial t} = \frac{D_{MGP}}{r^2}\frac{\partial}{\partial r}\left(r^2\frac{\partial [MGP]}{\partial r}\right) - k_{OH+MGP}[MGP][OH]_{ad-MGP} \qquad (3)$$

In the model, the initial particle water activity after the diffusion dryer is assumed to be 0.1. The room temperature experimental viscosity of glucose ($C_6H_{12}O_6$) at 0% relative humidity is 5.2×10^8 Pa s which is much smaller than the viscosity of glass transition at room temperature (12 Pa s). [10] Thus the gas/particle equilibrium follow the linear relationship ($\tau_{eq} = \frac{R_p^2}{\pi^2 D}$). For highly viscous droplet with a diameter between 50 and 500 nm, the time scale to establish gas-particle equilibrium is generally governed by particle-phase diffusion. [11] The experimental diffusion coefficient of water in pure citric acid ($C_6H_8O_7$) droplet with a water activity of 0.1 is about 1.0×10^{-11} cm^2 s^{-1}. [12] When the MGP ($C_7H_{14}O_6$) dry particles with water activity of 0.1 are introduced into flow tube with 10%, 20% and 30% relative humidity respectively, the time scale of gas-particle equilibrium is about 1 s based on the gas-particle equilibrium equation ($\tau_{eq} = \frac{R_p^2}{\pi^2 D_b}$). The particle phase water content concentration is in equilibrium with the surrounding relative humidity in the gas phase through the flow tube. Thus, the particle viscosity is uniform through the reaction. In the model, the diffusion coefficient of bulk molecule MPG ($C_7H_{14}O_6$) is assumed to be constant and the same everywhere in the particle despite bulk concentration gradient due to oxidation reaction.

A summary of simulation parameters and rate constants is shown in Table 3.2.

Table 3. 2 Key simulation parameters and rate constants for mixture semisolid particles.

Parameter	Value	Description
RH	10%, 20%, 30%	Relative humidity
[OH]	5.40×10^{10}	Average experimental [OH]
r_p	100 nm	Radius of the particle
k_{ad}	10 s^{-1}	Pseudo-first order adsorption rate coefficient of OH. [6]
k_{des}	2.86×10^{10} s^{-1}	Desorption rate coefficient of OH. [7]
k_{OH+MGP}	5.31×10^{-12} cm^3 s^{-1}	Rate coefficient of OH+MGP in aqueous solution. [8]

D_{OH}	1.00×10^{-9} cm^2 s^{-1}	Diffusion coefficient for OH. [5]
r_{MGP}	0.361nm	Hydrodynamic radius of MGP at 298.15K. [13]
$D_{MGP}^{10\%RH}$	2.50×10^{-14} cm^2 s^{-1}	Diffusion coefficient of MGP with a water activity of 0.1. (Viscosity of glucose particles at 10%RH is 7.40 (log value), based on E-S equation: $D_{glucose}^{10\%RH}=2.47 \times 10^{-16}$ cm^2 s^{-1}). [10]
$D_{MGP}^{20\%RH}$	8.00×10^{-14} cm^2 s^{-1}	Diffusion coefficient of MGP with a water activity of 0.2. (Viscosity of glucose particles at 20%RH is 6.10 (log value), based on E-S equation: $D_{glucose}^{20\%RH}=4.84 \times 10^{-15}$ cm^2 s^{-1}). [10]
$D_{MGP}^{30\%RH}$	3.50×10^{-13} cm^2 s^{-1}	Diffusion coefficient of MGP with a water activity of 0.3. (Viscosity of glucose particles at 30%RH is 5.55 (log value), based on E-S equation: $D_{glucose}^{30\%RH}=1.69 \times 10^{-14}$ cm^2 s^{-1}). [10]

*the water activity of sample is equal to the relative humidity of gas surrounding sample

3.2.2 Reaction-Diffusion model results

Figure 3.8 shows the modeled unreacted mole fraction of MPG ($C_7H_{14}O_6$) integrated over the entire particle as a function of OH exposure for 10% (blue solid line), 20% (black solid line) and 30% (red solid line) relative humidity. These profiles reproduce the observed MPG ($C_7H_{14}O_6$) decay behaviors in Figure 3.3. These decay behaviors can be interpreted by examination of the diffusion coefficients of MPG ($C_7H_{14}O_6$) in the system. In this work, the value of $D_{MGP}^{10\% RH}$ is set as 2.50×10^{-14} cm^2 s^{-1}, which is 100 times bigger than the diffusion coefficient of glucose ($D_{glucose}^{10\%RH}=2.47 \times 10^{-16}$ cm^2 s^{-1}) established from binary aqueous-glucose viscosity with water activity of 0.1. The value of $D_{MGP}^{20\% RH}$ is set as 8.00×10^{-14} cm^2 s^{-1}, which is 16 times bigger than the diffusion coefficient of glucose ($D_{glucose}^{20\%RH}=4.84 \times 10^{-15}$ cm^2 s^{-1}) established from binary aqueous-glucose viscosity with water activity of 0.2. The value of $D_{MGP}^{30\% RH}$ is set as 3.50×10^{-13} cm^2 s^{-1},

which is 20 times bigger than the diffusion coefficient of glucose ($D_{glucose}^{30\%RH}=1.69\times10^{-14}$ cm^2 s^{-1}) established from binary aqueous-glucose viscosity with water activity of 0.3. [10] This model shows an associated increase in relative humidity and bulk diffusion coefficient of particle molecule species. At 10% RH, the modeled decay of MGP deviates from the experimental data. The difference between experimental and computational results may be attribute to either unstable wet N$_2$ flow rate during the kinetics measurement, or limitation of model by using a constant bulk diffusion.
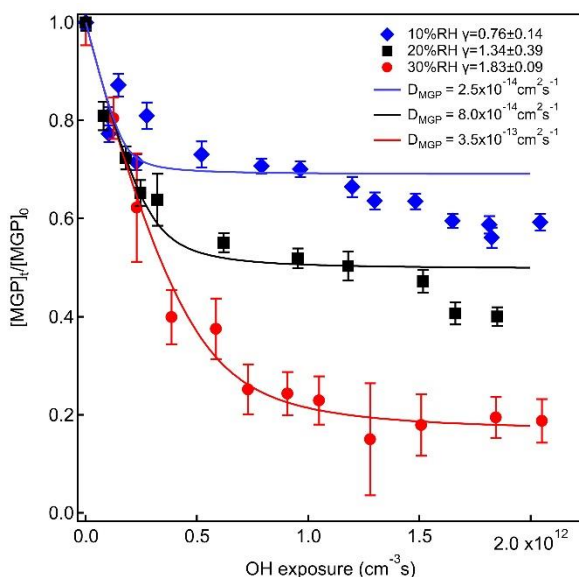
Figure 3. 8 Modeled total fraction of reactant remaining for different OH exposure for RH=10% (thin blue line), RH=20% (thin black line), and RH=30% (thick red line)

Figure 3.9 displays the modeled space-time plots of bulk concentration of MPG (C$_7$H$_{14}$O$_6$) for 10%, 20% and 30% relative humidity with a constant OH concentration of 5.40×10^{10} cm^{-3}. The y-axis is the radial distance from the core of the aerosol particle, which is 100 nm. The x-axis is the reaction time of 37 s. The MGP (C$_7$H$_{14}$O$_6$) concentration is assumed to be distributed uniformly within the particle at the reaction time zero, which is 4.53×10^{21} molecules cm^{-3}. For 10% relative humidity, the bulk of particle is free of OH radicals as most of them reacted at the surface. The depleted MGP (C$_7$H$_{14}$O$_6$) is within the outermost 20 nm of the aerosol. The surface concentration of MGP (C$_7$H$_{14}$O$_6$) stays low, which is about 1.67×10^{20} molecules cm^{-3}. The modeled unreacted mole fraction of reactant MGP (C$_7$H$_{14}$O$_6$) over the entire particle is about 0.69 up to a reaction time of 37s. For 20% relative humidity, the MGP (C$_7$H$_{14}$O$_6$) concentration decays occur more

deeply into the particle bulk and the MGP ($C_7H_{14}O_6$) concentration gradient is in the top 40 nm of the particle. After 37 s, the modeled unreacted mole fraction of reactant MGP ($C_7H_{14}O_6$) over the
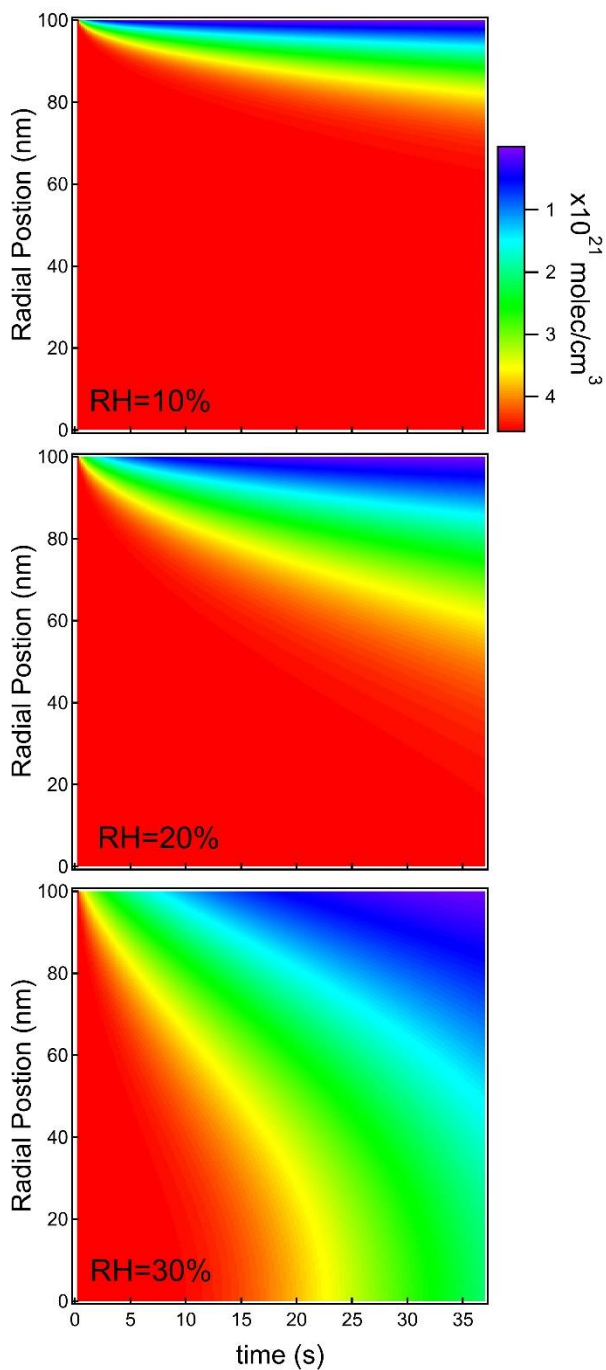
Figure 3. 9 Modeled space-time plots of bulk concentration of MPG ($C_7H_{14}O_6$) for (a) 10%, (b) 20% and (c) 30% relative humidity. The constant OH concentration is 5.40×10^{10} cm^{-3}.

entire particle is about 0.50 due to chemical reaction with OH radicals. For 10% and 20% relative humidity, the MGP ($C_7H_{14}O_6$) concentration in the unreactive core remains homogenously through the reaction. For 30% relative humidity, the model shows that gradient in the MGP ($C_7H_{14}O_6$) concentration is generated relatively rapidly compared to those of 10% RH and 20% RH studies. The magnitude of this diffusion coefficient is sufficient to allow the MGP ($C_7H_{14}O_6$) reactant in the core of the particle to diffuse to the particle surface and react with OH radicals. The MGP ($C_7H_{14}O_6$) concentration in the core of particle is about half of that of unreacted initial MGP ($C_7H_{14}O_6$). The modeled unreacted mole fraction of reactant MGP ($C_7H_{14}O_6$) over the entire particle is about 0.17 after reaction time of 37 s.

3.3 Discussion and implication for heterogeneous chemistry

The reaction between OH radical and MGP ($C_7H_{14}O_6$) molecule has been studied in the liquid solution by identifying the final products as well as the reaction intermediates. [9, 14-16] Electron paramagnetic resonance experiments showed that the initial reaction step is a hydrogen atom from the organic function group RH abstracted by OH radical to produce an organic radical and a water molecule. [9] In the presence of O_2, α-hydroxy-peroxyl radical is generated. [16] These peroxyl radicals can then decompose to give a HO_2 radical and a carbonyl compound. The main products have been observed are glucose and some organic acids through the loss of small alcohol and ketone molecules as determined in the aqueous solution. [15] The relative humidity independent rapid rise of the product signals shown in the Figure 3.7 are in agreement with oxidation of carbohydrate at the particle surface. The observed decays of product signals are likely to be due to further reaction with the OH radicals. Propagation chain reaction in the particle bulk would likely produce volatile organic compound which vaporize into the gas phase. The normalized product signals are consistent with chemical reactions mostly occurred at the particle surface with negligible bulk activity. The presence of the products in the particle surface has no significant effect on heterogeneous oxidation kinetics behavior. No evidence of oligomer products is observed in the present work. From these data, it is likely that MGP ($C_7H_{14}O_6$) rapidly react with OH and break down into smaller molecular species and vaporized to the gas phase.

A reaction diffusion model with a fast surface-only reaction is developed to evaluate the effect of varying bulk diffusion coefficients due to changes in the particle surrounding relative humidity during exposure to OH radicals. OH radicals are assumed to react with MGP ($C_7H_{14}O_6$)

molecule in semi solid organic matrix with the same rate coefficient as in the aqueous phase. In the simulation, the particle is assumed to be with a constant diameter by neglecting the vaporization of the volatile organic products. The assumption that OH radicals adsorbed onto the particle surface lead to reaction has been shown to be valid for OH radicals reacting with most saturated organic molecules with an initial step of abstraction of a hydrogen atom. The vaporization of volatile organic products from the particle surface would lead a new MGP ($C_7H_{14}O_6$) layer with effect on the particle bulk. The qualitative agreement between the experimental data in Figure 3.3 and the simulation result in Figure 3.8 suggest that the diffusion of MGP ($C_7H_{14}O_6$) from the bulk to the surface is the rate-limiting step. The reacto-diffusion length for OH radical within the particle is modeled to be within 1 nm, which is consistent with experimental measurement the reactive-diffusion length of OH in viscous organic aerosol. [3] Because the OH reacto-diffusion length is so small, the depth over which reaction occur is dependent on the diffusion coefficient of reactant in the condensed phase. As is shown in Figure 3.9, there is a gradient concentration of MPG distribution in the particle due to the slow diffusion of MGP ($C_7H_{14}O_6$). From 10% relative humidity to 30% relative humidity, the water content in the condensed phase is increased, the particle viscosity is decreased, then the diffusion coefficient of MGP ($C_7H_{14}O_6$) is increased, thereby the depth of reaction region in the particle surface is increased from 20 nm to the whole volume of the particle.

The reaction-diffusion model developed here strongly links the occurrence of observed kinetics to particle viscosity at different relative humidity. This remains true even if an initial uniform particle viscosity is assumed. In this case, the diffusion of MGP ($C_7H_{14}O_6$) (D_{MGP}) across the particle is uniform, and provided D_{MGP} is based on binary aqueous-glucose viscosity through the Einstein-Stokes equation. The simulation results show that the MGP ($C_7H_{14}O_6$) decay behavior is extremely sensitive to the diffusion coefficient of MGP ($C_7H_{14}O_6$). A decrease in coefficient of MGP ($C_7H_{14}O_6$) can slow down the kinetic. Under such conditions, it takes longer time for the MGP ($C_7H_{14}O_6$) to diffuse into the particle surface due to the high particle viscosity. At 10% relative humidity condition, the value of D_{MGP} is 100 times bigger than the diffusion coefficient of glucose established from binary aqueous-glucose viscosity with water activity of 0.1. At higher relative humidity condition, the value of D_{MGP} is less than 20 times bigger than the diffusion coefficient of glucose established from binary aqueous-glucose viscosity with water activity of 0.3. [10] The simulation results of the decay of MGP ($C_7H_{14}O_6$) behavior reproduce the observed

experimental kinetic trends in Figure 3.3. It revealed two key findings: (1) heterogeneous oxidation of semi-solid particles is limited by the bulk diffusion. (2) the presence of water significantly increases water soluble aerosol reactivity by reducing the particle viscosity.

Madden et al have reported thin film experimental results for the heterogeneous oxidation of levoglucosan under different relative humidity conditions with offline analysis method. [9] The experimental results are opposite to the observed kinetics behavior in Figure 3.3. They found that the kinetics determined reactant concentration in the thin film are increased with the relative humidity decreased. For the thin film experiments, the heterogeneous decay of the levoglucosan reactant is not controlled by the diffusion of bulk reactant but more likely by surface phenomena.

Under real atmospheric condition, the life time of semi-solid particles may be inferred from the particle size, the value of reactive uptake coefficient and OH radical concentration. The kinetics result from Figure 3.3, supported by the reaction-diffusion model, suggests that at higher OH exposure, the reaction significantly slows down due to the slow bulk diffusion of reactant, therefore increasing the aerosol particles lifetime. The aerosol particles in high relative humidity environment may have a shorter lifetime.

3.4 Conclusion

The kinetics of the OH-initiated heterogeneous oxidation of methyl-β-D-glucopyranoside (MGP) ($C_7H_{14}O_6$) show an initial rapid decay followed by a slower decay of the bulk reactant fraction. The observed kinetics behavior become more prominent as the surrounding relative humidity decreases. The initial decay rates of pure semi-solid MGP ($C_7H_{14}O_6$) nanoparticles (up to an OH exposure of 0.5×10^{12} cm^{-3} s) are $6.73\pm0.06 \times10^{-13}$ for 10% RH, $1.19\pm0.17 \times10^{-12}$ for 20% RH and $1.62\pm0.04 \times10^{-12}$ for 30% RH. The corresponding reactive uptake coefficients obtained from the observed loss of particle species are 0.76 ± 0.14 for 10% RH, 1.34 ± 0.39 for 20% RH and 1.83 ± 0.09 for 30% RH. The bulk reactant decay rate coefficient is found to be independent on the gas phase molecular oxygen concentration.

The rise rates and decay rates of normalized products signal are independent on relative humidity. This suggests that the presence of products in the bulk has no effect on kinetics behavior of heterogeneous oxidation of semi-solid particles. The very low level of product signals remained

in the reacted particles suggests that the primary products due to the reactions occurred at the particle surface are likely to further react to give small molecular species that vaporized into the gas phase. Under these conditions, diffusion of the bulk reactant from the particle inner core to its surface is expected to be the rate limiting steps. A reaction-diffusion kinetic model using systems of partial differential equations is developed to support this hypothesis.

The reaction-diffusion kinetic model accounts for the changes in the diffusion coefficient of reactant in the particle. It suggests that the observed kinetics are consistent with particle viscosity, leading to uniform but very slow bulk diffusion of the reactant. The details of which processes take place are sensitive to the diffusion coefficient of bulk reactant using current best available literature data. The model currently only applies constant bulk diffusion and neglects particle size reduced due to the bulk mass reactive loss. The simulation results show that the bulk diffusion coefficient of reactant MGP ($C_7H_{14}O_6$) is increased as the relative humidity increased, which is consistent with a recent report that the binary aqueous-monosaccharide viscosity is decreased as the relative humidity is increased.

References:

1.	Kessler, S. H.; Smith, J. D.; Che, D. L.; Worsnop, D. R.; Wilson, K. R.; Kroll, J. H., Chemical Sinks of Organic Aerosol: Kinetics and Products of the Heterogeneous Oxidation of Erythritol and Levoglucosan. *Environmental Science & Technology* **2010,** *44* (18), 7005-7010.

2.	Zegota, H.; Von, C., Radiation Chemistry of Carbohydrates, XV OH Radical Induced Scission of the Glycosidic Bond in Disaccharides. In *Zeitschrift für Naturforschung B*, 1977; Vol. 32, p 1060.

3.	Lee, L.; Wilson, K., The Reactive–Diffusive Length of OH and Ozone in Model Organic Aerosols. *The Journal of Physical Chemistry A* **2016,** *120* (34), 6800-6812.

4.	Fan, H.; Tinsley, M. R.; Goulay, F., Effect of Relative Humidity on the OH-Initiated Heterogeneous Oxidation of Monosaccharide Nanoparticles. *The Journal of Physical Chemistry A* **2015,** *119* (45), 11182-11190.

5.	Smith, G. D.; Woods, E.; Baer, T.; Miller, R. E., Aerosol Uptake Described by Numerical Solution of the Diffusion−Reaction Equations in the Particle. *The Journal of Physical Chemistry A* **2003,** *107* (45), 9582-9587.

6.	Wiegel, A. A.; Liu, M. J.; Hinsberg, W. D.; Wilson, K. R.; Houle, F. A., Diffusive confinement of free radical intermediates in the OH radical oxidation of semisolid aerosols. *Physical Chemistry Chemical Physics* **2017,** *19* (9), 6814-6830.

7.	Vieceli, J. R., M.; Potter, N.; Dang, L. X.; Garrett, B. C. and Tobias, D. J. , Molecular Dynamics Simulations of Atmospheric Oxidants at the Air−Water Interface: Solvation and Accommodation of OH and O3. *J. Phys. Chem. B.* **2005,** (109), 15876-15892.

8.	Zakatova, N. V. M., D. P. and Sharpatyi, V. A., Role of OH-radicals in the radiolytic decomposition of carbohydrates and polysaccharides. *Bull. Acad. Sci. USSR, Div. Chem. Sci. (Engl. Tran)* **1969**.

9.	Madden, K. P. a. F., R. W. , Est Study of the Attack of Photolytically Produced Hydroxyl Radicals on Alpha-Methyl-D-Glucopyranoside in Aqueous Solution. *J. Am. Chem. Soc.* **1982,** (104), 2578-2581.

10.	Song, Y. C.; Haddrell, A. E.; Bzdek, B. R.; Reid, J. P.; Bannan, T.; Topping, D. O.; Percival, C.; Cai, C., Measurements and Predictions of Binary Component Aerosol Particle Viscosity. *The Journal of Physical Chemistry A* **2016,** *120* (41), 8123-8137.

11.   Mai, H.; Shiraiwa, M.; Flagan, R. C.; Seinfeld, J. H., Under What Conditions Can Equilibrium Gas–Particle Partitioning Be Expected to Hold in the Atmosphere? *Environmental Science & Technology* **2015,** *49* (19), 11485-11491.

12.   Davies, J. F.; Wilson, K. R., Raman Spectroscopy of Isotopic Water Diffusion in Ultraviscous, Glassy, and Gel States in Aerosol by Use of Optical Tweezers. *Analytical Chemistry* **2016,** *88* (4), 2361-2366.

13.   Lide, D. R., *CRC Handbook of Chemistry and Physics*. 64th ed.; CRC Press: Boca Raton: FL, 1983.

14.   Yokoyama, T.; Nakagawa, A.; Konishi, F.; Matsumoto, Y., Investigation on hydrogen abstraction from methyl glucoside by active oxygen species under oxygen delignification conditions III: effects of the origin of active oxygen species. *Journal of Wood Science* **2011,** *57* (6), 512-519.

15.   Guay, D. F.; Cole, B. J. W.; Fort, R. C.; Hausman, M. C.; Genco, J. M.; Elder, T. J.; Overly, K. R., MECHANISMS OF OXIDATIVE DEGRADATION OF CARBOHYDRATES DURING OXYGEN DELIGNIFICATION. II. REACTION OF PHOTOCHEMICALLY GENERATED HYDROXYL RADICALS WITH METHYL β-CELLOBIOSIDE. *Journal of Wood Chemistry and Technology* **2001,** *21* (1), 67-79.

16.   Schuchmann, M. N. a. S., C. V. , Radiation-Chemistry of Carbohydrates XV Hydroxyl Radical Induced Oxidation of D-Glucose in Oxygenated Aqueous-Solution. *J. Chem. Soc. Perkin Trans* **1977,** (2), 1958-1963.

Chapter Four

Effect of Bulk Composition on the Heterogeneous Oxidation of Semi-solid Multi-component Saccharide Aerosols

Chapter 4: Effect of bulk composition on the heterogeneous oxidation of semi-solid multi-component saccharide aerosols

In the present work, we use lactose ($C_{12}H_{22}O_{11}$) and MGP (methyl-β-D-glucopyranoside, $C_7H_{14}O_6$) as model molecules to form highly oxygenated semi-solid organic particles. The goal of the present study is to investigate the impact of oligomer-induced viscosity changes on the mechanisms of oxidative aging of semi-solid particles through both online VUV-AMS (Vacuum-Ultraviolet Aerosol Mass Spectrometer) and offline GC-MS (Gas chromatograph Gas chromatograph interfaced with a Single Quadrupole Mass Spectrometer) analysis techniques using an atmospheric pressure flow-tube reactor. The decay rates of saccharide are determined by measuring the loss signal of saccharide in the particle phase as a function of OH exposure (time-integrated total concentration of OH radical). The observed decay rates in semi-solid particles are monitored for MGP:lactose molar ratios of 1:1, 2:1, 4:1, and 8:1. Implications of differences in decay rates of MGP and lactose over a range of molar ratio MGP:lactose are discussed in a diffusion-reaction kinetic model with a composition-dependent diffusion coefficient.

4.1 Experimental results

4.1.1 Kinetic results

4.1.1.1 VUV-AMS analysis kinetic results

Figure 4.1 displays the relative abundances of unreactive MGP reactant remaining in the particle phase as a function of OH exposure at MGP:lactose molar ratios of 1:1 (red solid circles), 2:1 (black solid squares), 4:1 (blue solid triangles), and 8:1 (green solid diamonds). The experimental data are reported for relative humidity at 30% RH. The relative signal of MGP is an average of five different mass fragments (m/z 60, m/z 73, m/z 121, m/z 144, m/z 163) identified in the aerosol mass spectra. The error bars are two standard deviation from the mean value. The solid lines are exponential fits to the experimental data with an exponential function below OH exposures of 2.0×10^{12} molecules cm^{-3} s $^{-1}$ in order to determine the rate constants for the reaction of OH with MGP at MGP:lactose molar ratios of 1:1, 2:1, 4:1, and 8:1, respectively. For high OH exposure, the mass fractions of MGP reactant remaining in the particle are 0.76 at 1:1 ratio, 0.65 at 2:1 ratio, 0.39 at 4:1 and 0.26 at 8:1 ratio. The summary of rate constants and uptake coefficients is shown

in Table 4.1. The calculated uptake coefficients using initial decay kinetics only indicate the particle reactivity at low OH exposure. The error bars are two standard deviation from the individual measurements.

Table 4. 1 Rate constants and uptake coefficients for MGP in OH oxidation of semi-solid MGP-lactose particles at 30% RH obtained in online kinetics measurement.

Molar ratio (MGP:lactose)	Rate constant $k_{MGP} \pm 2\sigma$ $(cm\ s^{-1})$	Uptake coefficient $(\gamma_{MGP} \pm 2\sigma)$
1:1	$4.02 \pm 4.78 \times 10^{-14}$	0.05 ± 0.06
2:1	$2.24 \pm 1.10 \times 10^{-13}$	0.31 ± 0.15
4:1	$3.26 \pm 0.04 \times 10^{-13}$	0.48 ± 0.01
8:1	$4.73 \pm 0.68 \times 10^{-13}$	0.73 ± 0.10

Figure 4. 1 Decay of MGP as a function of OH exposure obtained at MGP:lactose molar ratios of 1:1 (red solid circles), 2:1 (black solid squares), 4:1 (blue solid triangles), and 8:1 (green solid diamonds). The kinetics are measured using five ion peaks (m/z60, m/z73, m/z121, m/z144, m/z163). The error bars are 2σ about the mean value from the average of $[MGP]/[MGP]_0$. The solid lines (red for 1:1 ratio, black for 2:1 ratio, blue for 4:1 ratio and green for 8:1

ratio) are exponential fits of the MGP experimental data for OH exposure below 2×10^{12} molecule cm^{-3} s^{-1} and extrapolated to higher OH exposure (dash lines).

4.1.1.2 GC-MS analysis kinetic results

Figure 4.2 displays the relative abundances of unreactive MGP (red solid circles) and lactose (black solid squares) remaining in the particle as a function of OH exposure at MGP:lactose molar ratios of (a) 1:1, (b) 2:1, and (c) 4:1. The experimental data are reported for relative humidity at 30% RH. Within the experimental error bars, the observed MGP decay rate is close to that of lactose at MGP:lactose molar ratios of 1:1 and 2:1. At ratio 4:1, the initial lactose decay appears to be much slower than that of MGP reactant up to OH exposure of 2.0×10^{12} molecules cm^{-3} s^{-1}. At high OH exposure, the mass fractions of unreacted reactants remaining in the particle are 0.92, 0.77, 0.66 for MGP, and 0.87, 0.85, 0.66 for lactose at MGP:lactose molar ratios of 1:1, 2:1, and 4:1, respectively. The solid lines are exponential fits to the experimental data with an exponential function up to OH exposures of 1.6×10^{12} molecules cm^{-3} s^{-1}, 1.3×10^{12} molecules cm^{-3} s^{-1}, 1.2×10^{12} molecules cm^{-3} s^{-1} in order to determine the rate constants for the reaction of OH with MGP/lactose at MGP:lactose molar ratios of 1:1, 2:1, and 4:1, respectively. The summary of rate coefficients and effective uptake coefficients is displayed in Table 4.2.

Table 4. 2 Rate constants and uptake coefficients for OH oxidation of semi-solid MGP-lactose particle at 30% RH obtained in offline kinetics measurement.

Molar ratio (MGP:lactose)	Rate constant $k_{MGP}\pm2\sigma$ (cm s^{-1})	Uptake coefficient ($\gamma_{MGP}\pm2\sigma$)	Rate constant $k_{Lac}\pm2\sigma$ (cm^3 s^{-1})	Uptake coefficient ($\gamma_{Lac}\pm2\sigma$)
1:1	$1.63\pm0.66\times10^{-13}$	0.21 ± 0.08	$1.30\pm0.12\times10^{-13}$	0.17 ± 0.02
2:1	$2.88\pm0.74\times10^{-13}$	0.42 ± 0.11	$2.34\pm0.55\times10^{-13}$	0.34 ± 0.08
4:1	$4.11\pm1.61\times10^{-13}$	1.06 ± 0.25	$0.94\pm0.50\times10^{-13}$	0.15 ± 0.08
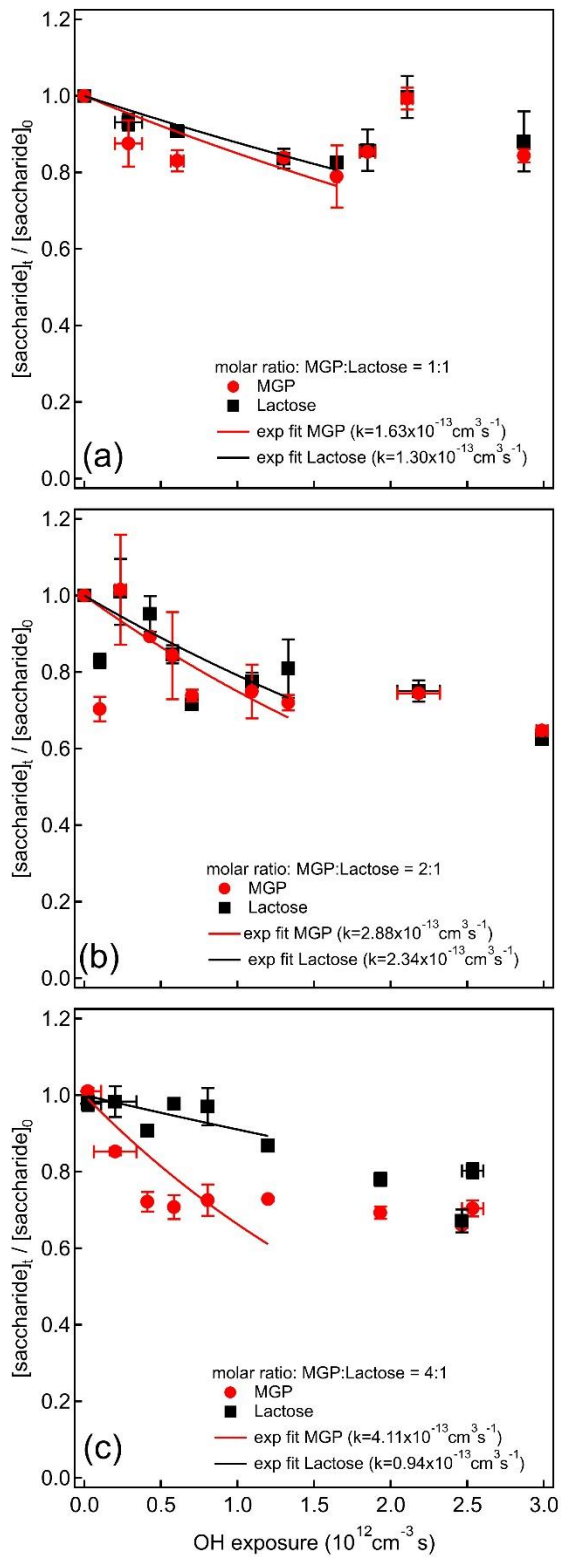
Figure 4. 2 The normalized concentration of unreacted MGP (red solid circles) and lactose (black filled squares) remaining in semi-solid MGP-lactose particles at 30% RH as a function of OH exposure obtained by GC-MS analysis

for MGP:lactose molar ratios of (a) 1:1; (b) 2:1; (c) 4:1 kinetics measurement. The error bars of $[saccharide]_t/[saccharide]_0$ represent the maximum and minimum experimental values. The error bars of OH exposure are two standard deviation about the mean value of four GC-FID analysis measurement. The lines (red for MGP, black for lactose) are exponential fits of the experimental data at OH exposures below 1.6×10^{12} molecule cm^{-3} s $^{-1}$.

4.1.2 Particle size characterization

Figure 4.3 displays the surface-weighted particle size distribution for semi-solid saccharide particles obtained in both online experiment and offline experiment. The particle sizer scan of saccharide particles is from unreacted sample with MGP:lactose a molar ratio of 1:1. The average of particle surface-weighted diameter of online analysis sample is about 220 nm and that of offline analysis sample is about 360 nm.
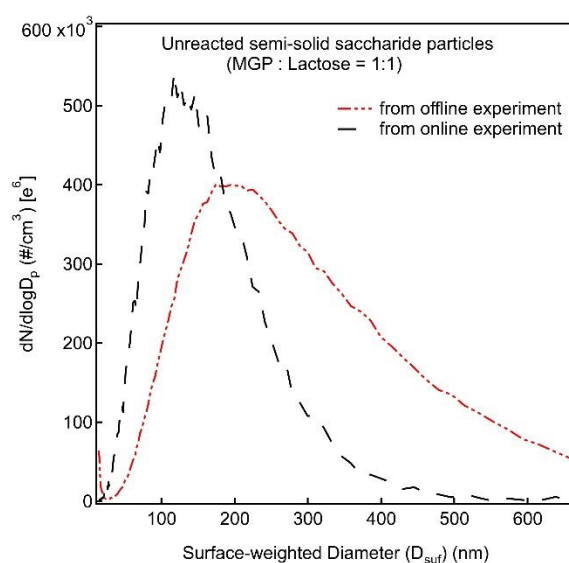
Figure 4. 3 Surface-weighted particle size distribution for unreacted saccharide particles with MGP:lactose a molar ratio of 1:1. The mean surface-weighted diameter and the total concentration of number particle size are 218.2 nm and 3.05×10^5 #/cm^3 for the VUV-AMS analysis sample (black dashed line) and 366.4 nm and 2.58×10^5 #/cm^3 for the GC-MS analysis sample (red dashed line).

4.1.2.1 VUV-AMS analysis evolution of particle size characterization

Figure 4.4 displays the absolute surface-weighted diameter (nm) as a function of OH exposure obtained at MGP:lactose molar ratios of 1:1 (red solid circles), 2:1 (black solid squares), 4:1 (blue solid up-triangles), and 8:1 (green solid down-triangles). These data are measured by Scanning

Mobility Particle Sizer (SMPS) measurement. The error bars are two standard deviation about triple time particle size data measurement. The typical surface-weighted mean diameter of the particles is about 220 nm for this study. There is no significant decrease on surface-weighted mean diameter as function of OH exposure for all ratios study.
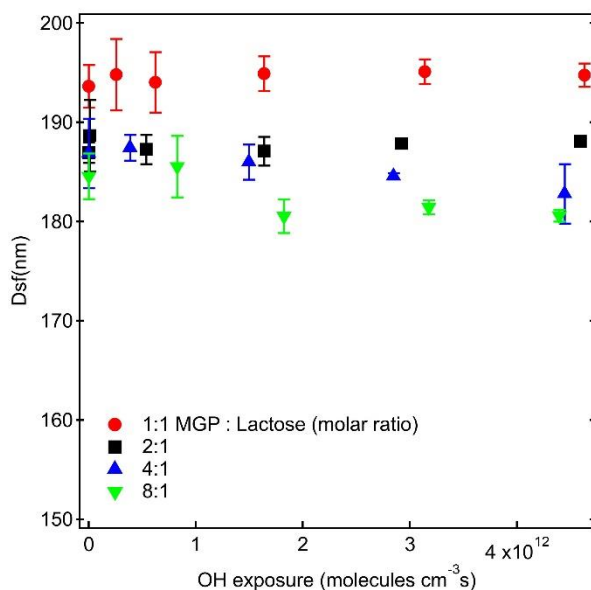
Figure 4. 4 Absolute surface weighted diameter as a function of OH exposure obtained at MGP:lactose molar ratios of 1:1 (red solid circles), 2:1 (black solid squares), 4:1 (blue solid up-triangles), and 8:1 (green solid down-triangles). The error bar is 2σ about mean value.

Figure 4.5 displays relative single particle mass fraction remaining as a function of OH exposure obtained at MGP:lactose molar ratios of 1:1 (red solid circles), 2:1 (black solid squares), 4:1 (blue solid up-triangles), and 8:1 (green solid down-triangles). All these data are measured by Scanning Mobility Particle Sizer. The error bars are two standard deviation about triple time particle size data collection. There is no significant decrease within error on relative single particle mass fraction remaining as a function of OH exposure for all ratios study.
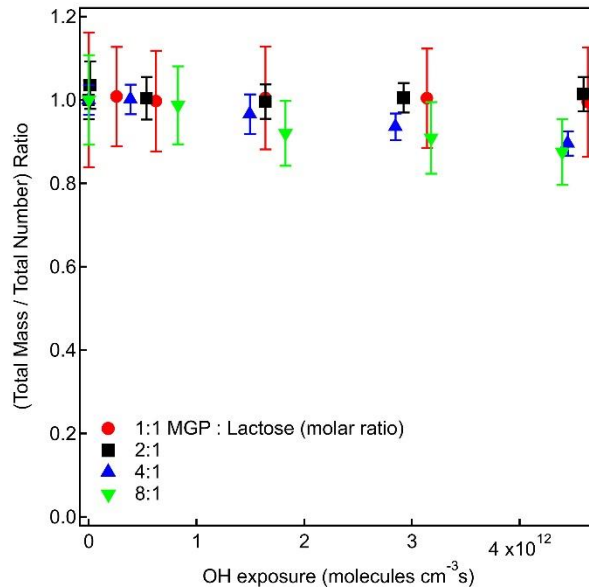
Figure 4. 5 Relative single particle mass fraction remaining as a function of OH exposure obtained at MGP:lactose molar ratios of 1:1 (red solid circles), 2:1 (black solid squares), 4:1 (blue solid up-triangles), and 8:1 (green solid down-triangles). The error bar is 2σ about mean value.

4.1.2.2 GC-MS analysis evolution of particle size characterization

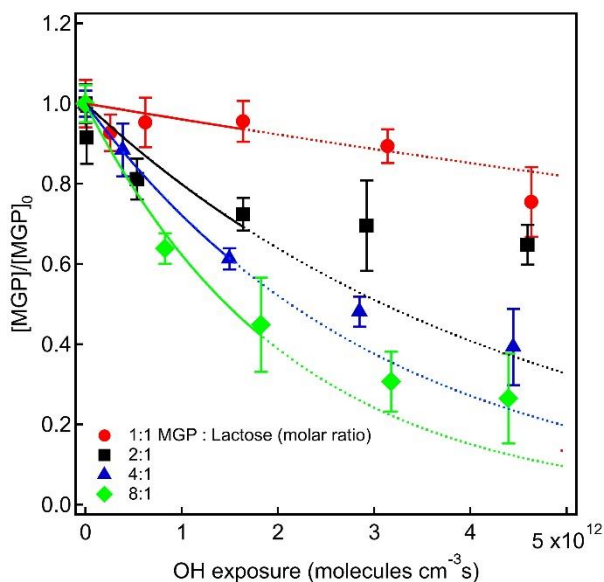Figure 4.6 displays relative surface weighted diameter as a function of OH exposure obtained at MGP:lactose molar ratios of 1:1 (red solid circles), 2:1 (black solid squares), and 4:1 (blue solid triangles). These data are measured by Scanning Mobility Particle Sizer (SMPS) measurement. The error bars are two standard deviation about four time particle size data measurement. The typical surface-weighted mean diameter of the particles is about 360 nm for this study. There is no significant decrease on surface-weighted mean diameter as function of OH exposure for all ratios study.
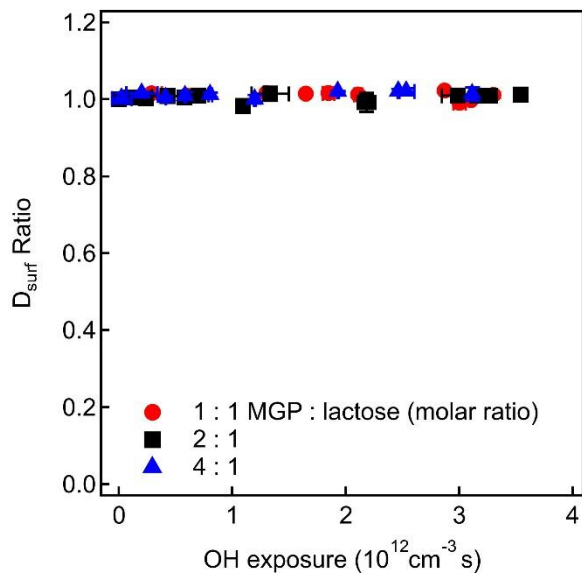
Figure 4. 6 Relative surface weighted diameter as a function of OH exposure obtained at MGP:lactose molar ratios of 1:1 (red solid circles), 2:1 (black solid squares), 4:1 (blue solid triangles). The error bar is 2σ about mean value.

Figure 4.7 displays relative single particle mass fraction remaining as a function of OH exposure obtained at MGP:lactose molar ratios of 1:1 (red solid circles), 2:1 (black solid squares), and 4:1 (blue solid up-triangles). These data are measured by Scanning Mobility Particle Sizer (SMPS) measurement. The error bars are two standard deviation about four time particle size data measurement. There is no significant decrease within error on relative single particle mass fraction remaining as a function of OH exposure for all ratios study.
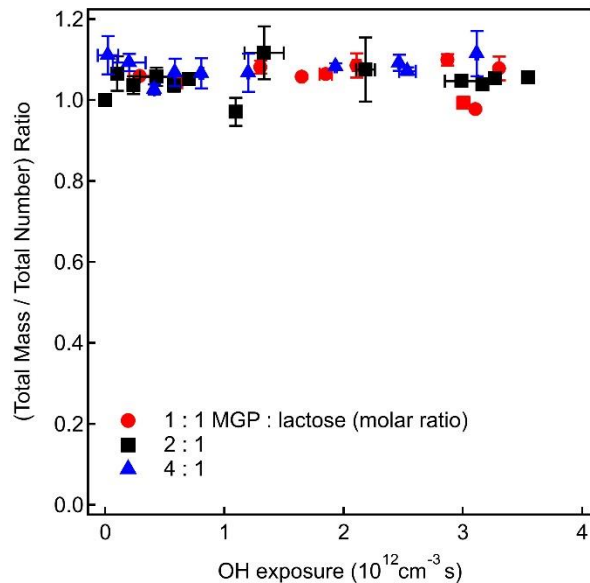
Figure 4. 7 Relative single particle mass fraction remaining as a function of OH exposure obtained at MGP:lactose molar ratios of 1:1 (red solid circles), 2:1 (black solid squares), 4:1 (blue solid up-triangles). The error bar is 2σ about mean value.

4.1.3 Products identification

Figure 4.8 displays typical offline analysis of chromatograms obtained for the unreacted (black) and reacted (red) saccharides particle with MGP:lactose a molar ratio of 4:1 collected at the OH exposure of 1.2×10^{12} molecule $cm^{-3} s^{-1}$.
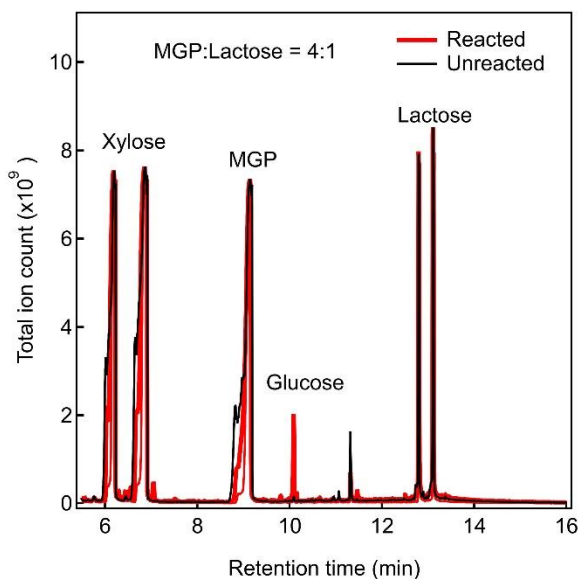
Figure 4. 8 GC-MS chromatogram of the silylated saccharides from the OH-initiated oxidation of saccharides for MGP:lactose a molar ratio of 4 : 1 at the OH exposure of 1.2×10^{12} molecule cm^{-3} s^{-1}. The reacted sample is red line and unreacted sample is black line. The retention time for internal standard xylose is 6.17 min and 6.83 min, for reactant MGP is 9.13 min, for reactant lactose is 12.79 min and 13.10 min, for glucose product is 10.09 min. The glucose product starts to be observed in the ratio 4:1 study. All the saccharides were identified with authentic samples.

Figure 4.9 shows a normalized product glucose signal as a function of OH exposure identified in semi-solid MGP-lactose particles with a molar ratio of 4:1. The glucose signal starts to be detected at OH exposure of 4.0×10^{11} molecules cm^{-3} s^{-1} and reach a maximum at OH exposure of 6.0×10^{11} molecules cm^{-3} s^{-1}. The glucose signal is relative stable between OH exposure of 1.0×10^{12} molecules cm^{-3} s^{-1} and 3.0×10^{12} molecules cm^{-3} s^{-1}. The glucose signal starts to be reduced after OH exposure of 3.0×10^{12} molecules cm^{-3} s^{-1}.
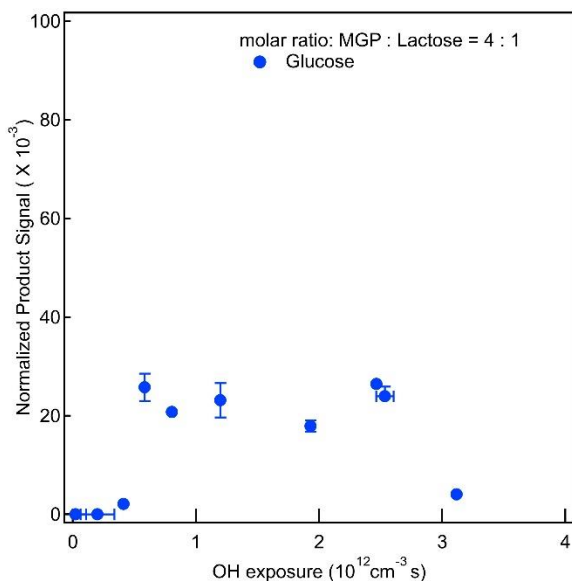
Figure 4. 9 Normalized signal of glucose detected in semi-solid MGP-lactose particles at a molar ratio of 4:1 as a function of OH exposure. The error bars of normalized product signal represent the maximum and minimum experimental values. The error bars of OH exposure are two standard deviation about the mean value of four GC-FID analysis measurement.

4.2 Reaction-Diffusion model development

4.2.1 Reaction-Diffusion model overview

A. Model study of bulk composition effect on semisolid particle diffusion

A reaction-diffusion kinetic model is developed in order to investigate the effect of composition-dependent diffusion on heterogeneous reaction behaviors. The coupled partial differential equations are solved using numerical solver pdepe in Matlab software. [1, 2]

Detailed Reaction-Diffusion equations.

The OH concentration at the particle surface is modeled using a multistep uptake mechanism: [3]

$$OH_g + site_{lactose} \xrightarrow{k_{ad}} OH_{ad-lactose} \qquad \text{(R1)}$$

$$OH_g + site_{MGP} \xrightarrow{k_{ad}} OH_{ad-MGP} \qquad \text{(R2)}$$

$$OH_{ad-lactose} \xrightarrow{k_{des}} OH_g + site_{lactose} \qquad \text{(R3)}$$

$$OH_{ad-lactose} \xrightarrow{k_{des}} OH_g + site_{lactose} \qquad \text{(R4)}$$

$$OH_{ad-latose} + lactose \xrightarrow{k_{OH+lactose}} Product + H_2O + site_{lactose} \qquad \text{(R5)}$$

$$OH_{ad-MGP} + MGP \xrightarrow{k_{OH+MGP}} Product + H_2O + site_{MGP} \qquad \text{(R6)}$$
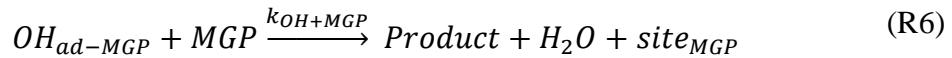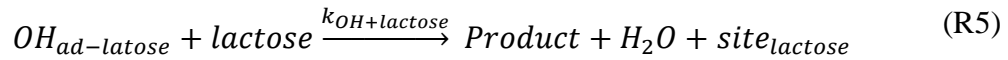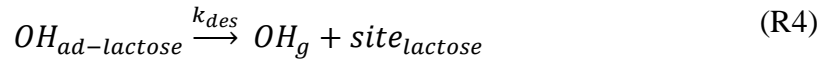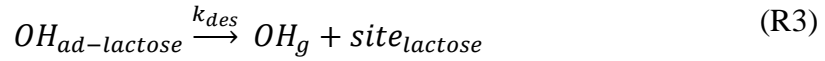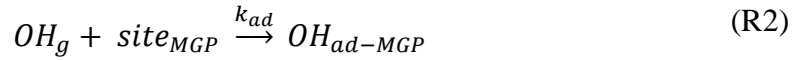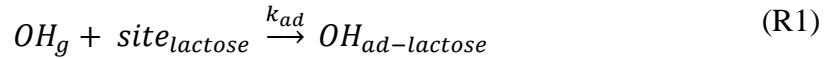
where k_{ad} is the pseudo-first order rate coefficient of adsorption (10 s^{-1}), [4] k_{des} is the rate coefficient of desorption (2.86×10^{10} s^{-1}). [5] The rate coefficient for OH reacting with lactose $k_{OH+lactose}$ is set to its value in aqueous solution: 5.15×10^{-12} cm^3 s^{-1}. [6] k_{OH+MGP} , the rate coefficient for OH reacting with MGP in aqueous solution is 5.31×10^{-12} cm^3 s^{-1}. [7] The above multiple steps describe the following microscopic process: first, the OH radicals in the gas phase adsorb onto a surface site. Site is one per saccharide at the surface of the particle. After adsorption, the OH radicals either desorb back into the gas phase or react by abstracting a hydrogen atom from saccharide which produces a water and another surface site. The mole fraction of surface site for MGP/lactose is the same as its bulk mole fraction. The experimental average OH concentration is

1.35×10^{11} molecules cm^{-3} for VUV-AMS analysis kinetic experiments and 8.70×10^{10} molecules cm^{-3} for GC-MS analysis kinetic experiments. The diffusion coefficient of OH radical in the particle phase (D_{OH}) is set to be 1×10^{-9} cm^2 s^{-1}, which is close to the value of D_{H_2O} for mixtures of citric acid ($C_6H_8O_7$) and sucrose ($C_{12}H_{22}O_{11}$) droplet at 30% RH. [8] The concentrations and diffusion coefficients of the saccharide molecules are assumed to be radially homogeneous before the reaction. The particles are assumed to have spherical symmetry with a radius of 100 nm for VUV-AMS analysis sample and 180 nm for GC-MS analysis sample. The reaction-diffusion equations written using spherical polar coordinates are as follows:

$$\frac{\partial [OH]_{ad-Lac}}{\partial t} = \frac{D_{OH}}{r^2} \frac{\partial}{\partial r} \left(r^2 \frac{\partial [OH]_{ad-Lac}}{\partial r} \right) - k_{OH+Lac}[OH]_{ad-Lac}[lactose] \tag{1}$$

$$\frac{\partial [OH]_{ad-MGP}}{\partial t} = \frac{D_{OH}}{r^2} \frac{\partial}{\partial r} \left(r^2 \frac{\partial [OH]_{ad-MGP}}{\partial r} \right) - k_{OH+MGP}[OH]_{ad-MGP}[MGP] \tag{2}$$

$$\frac{\partial [lactose]}{\partial t} = \frac{D_{Lac(x_{Lac})}}{r^2} \frac{\partial}{\partial r} \left(r^2 \frac{\partial [lactose]}{\partial r} \right) - k_{OH+Lac}[lactose][OH]_{ad-Lac} \tag{3}$$

$$\frac{\partial [MGP]}{\partial t} = \frac{D_{MGP(x_{Lac})}}{r^2} \frac{\partial}{\partial r} \left(r^2 \frac{\partial [MGP]}{\partial r} \right) - k_{OH+MGP}[MGP][OH]_{ad-MGP} \tag{4}$$

A Vignes-type fit is used to parametrize the relationship between the diffusion coefficients of saccharides and bulk composition: [9]

$$D_{MGP(x_{MGP})}^{30\% \, RH} = (D_{MGP}^{30\% \, RH})^{x_{MGP}} (D_{lactose}^{30\% \, RH})^{(1-x_{MGP})} \tag{5}$$

where $D_{MGP}^{30\% \, RH}$ and $D_{lactose}^{30\% \, RH}$ are the diffusion coefficients of MGP and lactose in a binary aqueous droplet at 30% RH and x_{MGP} is the mole fraction of MGP. [10] The diffusion coefficients of saccharides in the mixture semi-solid particles follow a logarithmic dependence on the mole fraction of monosaccharide component. The value of $D_{MGP}^{30\% \, RH}$ is 6.00×10^{-13} cm^2 s^{-1}, which is 35 times higher than the diffusion coefficient of glucose established using the S-E relationship through the binary aqueous-glucose viscosity at 30% RH. [11] The value of $D_{lactose}^{30\% \, RH}$ is the same as the diffusion coefficient of sucrose established from the binary aqueous-sucrose viscosity at 30% RH. [10] The summary of simulation parameters and rate constants is shown in Table 4.3.

Table 4. 3 Key simulation parameters and rate constant for mixture semisolid particles

Parameter	Value	Description
RH	30%	Relative humidity
[OH]	1.35×10^{11} cm^{-3} (online)	Average experimental [OH]
	8.70×10^{10} cm^{-3} (offline)	
r_p	100 nm (online sample)	Radius of the particle
	180 nm (offline sample)	
k_{ad}	10 s^{-1}	Pseudo-first order adsorption rate coefficient of OH. [4]
k_{des}	2.86×10^{10} s^{-1}	Desorption rate coefficient of OH. [5]
k_{OH+MGP}	5.31×10^{-12} cm^3 s^{-1}	Rate coefficient of OH+MGP in aqueous solution. [7]
$k_{OH+lactose}$	5.15×10^{-12} cm^3 s^{-1}	Rate coefficient of OH+lactose in aqueous solution. [6]
D_{OH}	1×10^{-9} cm^2 s^{-1}	Diffusion coefficient for OH. [8]
$D_{MGP}^{30\%RH}$	6.0×10^{-13} cm^2 s^{-1}	Diffusion coefficient of MGP with a water activity of 0.3. (Binary aqueous-glucose viscosity at 30% RH is 5.554 (log value), based on E-S equation, $D_{glucose}^{30\%RH}=1.69\times10^{-14}$ m^2 s^{-1}). [11]
$D_{lac}^{30\%RH}$	1.5×10^{-17} cm^2 s^{-1}	Diffusion coefficient of lactose with a water activity of 0.3. (Binary aqueous-sucrose viscosity at 30% RH is 8.526 (log value), based on E-S equation, $D_{sucrose}^{30\%RH}=1.50\times10^{-17}$ m^2 s^{-1}). [11]
r_{MGP}	0.361nm	Hydrodynamic Radius of MGP molecule. [12]
r_{lac}	0.433nm	Hydrodynamic Radius of lactose molecule. [12]

4.2.2.1 VUV-AMS analysis kinetic model results

Figure 4.10 shows the modeled mass fractions of reactant MGP remaining in the particle as a function of OH exposure for different MGP:lactose molar ratios of 1:1, 2:1, 4:1, and 8:1. The profiles reproduce those observed in the VUV-AMS analysis kinetics measurement of saccharides decay behaviors observed in Figure 4.1. At ratio 1:1, the modeled decay of MGP is relative faster than the observed occurrence up to OH exposure of 2.0×10^{12} molecule cm^{-3} s $^{-1}$. In the VUV-AMS analysis kinetics measurement, the dry MGP-lactose particle stream after diffusion dryer (with less than 10% RH) were then directly mixing with 30% RH and reacting with OH radicals in the flow tube. It takes relative longer time for semi-solid MGP-lactose particles with ratio 1:1 to get equilibrium with surrounding 30% RH than those with ratio 2:1, 4:1 and 8:1. [11, 13] Davies and Wilson recently reported that D_{H_2O} for citric acid:sucrose molar ratio of 1:1 at 20% RH is about

1.0×10^{-12} cm^2 s^{-1}. [8] By using this value of D_{H_2O} calculated with $\tau_{eq} = \frac{R_p^2}{\pi^2 D_b}$ (R_p is the particle radius, and D_b is the water molecular diffusivity in the particle phase), it takes at least 10 s for a semi-solid particle with a radius of 100 nm to get equilibrium with surrounding RH. [13] In the flow tube, it takes much longer than 10 s for semi-solid MGP-lactose particles (ratio 1:1) to get equilibrium with surrounding 30% RH and the reaction is only 37 s here. The viscosity of semi-solid MGP-lactose particles with ratio 1:1 is higher than that of particles estimated with a uniform water activity of 0.3 in the simulation. Therefore, there is a discrepancy between the experimental observation and modeled behavior in the low OH exposure at ratio 1:1.
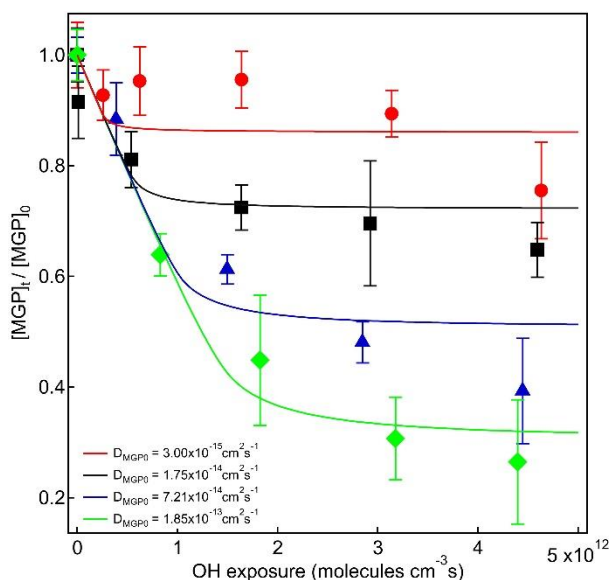
Figure 4. 10 Modeled total mass fraction of unreacted reactant MGP (solid lines) remaining in the particle as a function of OH exposure for different MGP:lactose molar ratios of 1:1 (red solid line), 2:1 (black solid line), 4:1 (blue solid line), and 8:1 (green solid line). The particle radius is 100 nm here. D_{MGP0} is the assumed initial diffusion coefficient of MGP in saccharides particle over different molar ratios. D_{MGP0} is 3.00×10^{-15} cm^2 s^{-1} at ratio 1:1. D_{MGP0} is 1.75×10^{-14} cm^2 s^{-1} at ratio 2:1. D_{MGP0} is 7.21×10^{-14} cm^2 s^{-1} at ratio 4:1. D_{MGP0} is 1.85×10^{-13} cm^2 s^{-1} at ratio 8:1.

4.2.2.2 GC-MS analysis kinetic model results

Figure 4.11 displays modeled mass fractions of unreacted MGP (solid lines) and lactose (dash lines) remaining in the particle as a function of OH exposure for MGP:lactose molar ratios of (a) 1:1 (red), (b) 2:1 (black), and (c) 4:1 (blue). These modeled profiles reproduce the trends observed in the GC-MS analysis kinetics measurement of saccharides decay behaviors observed in Figure 4.2. In the model, at ratio 1:1 and 2:1 the surface mole fraction of MGP/lactose reactive site is

equal to its bulk mole fraction. At ratio 4:1, the surface mole fraction of MGP is the same as its bulk mole fraction, but the lactose reactive site is reduced by a factor of 2 compared to its bulk mole fraction to reproduce the trend observed in Figure 4.2 (c).
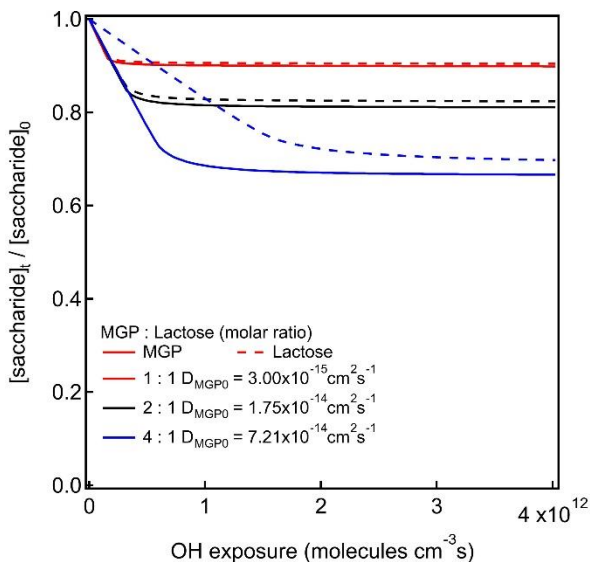
Figure 4. 11 Modeled mass fractions of unreacted MGP (solid lines) and lactose (dash lines) remaining in the particle as a function of OH exposure for MGP:lactose molar ratios of (a) 1:1 (red), (b) 2:1 (black), and (c) 4:1 (blue). D_{MGP0} is the assumed initial diffusion coefficient of MGP in the particle with different MGP:lactose molar ratios , which is radially homogeneous before the reaction. The diffusion coefficient of lactose is 0.83 of that of MGP. The diffusion coefficients of saccharides follow the Vignes-type relationship during the reaction. Here the particle radius is 180 nm.

Figure 4.12 displays the modeled space-time plots of MGP concentration for MGP:lactose molar ratios of (a) 1:1, (b) 2:1, (c) 4:1 with a constant OH gas number density of 8.70×10^{10} cm^{-3}. The particle radius is 180 nm and the reaction time is 46 s. In Figure 4.12 (a) At 46 s, the depleted MGP is observed to be only within the outermost 10 nm of the aerosol with its concentration being close to zero within top 0.3 nm of the particle. In Figure 4.12 (b) After 46 s, the MGP concentration decays occur 15 nm deeper into the particle bulk compared to that of MGP:lactose 1:1 ratio. The MGP concentration gradient is observed within the top 25 nm of the particle. In Figure 4.12 (c) it shows that a MGP concentration gradient is established within the outermost 50 nm of the particle after the reaction time of 46 s. The MGP concentration in the unreactive inner core remains homogeneously through the reaction.
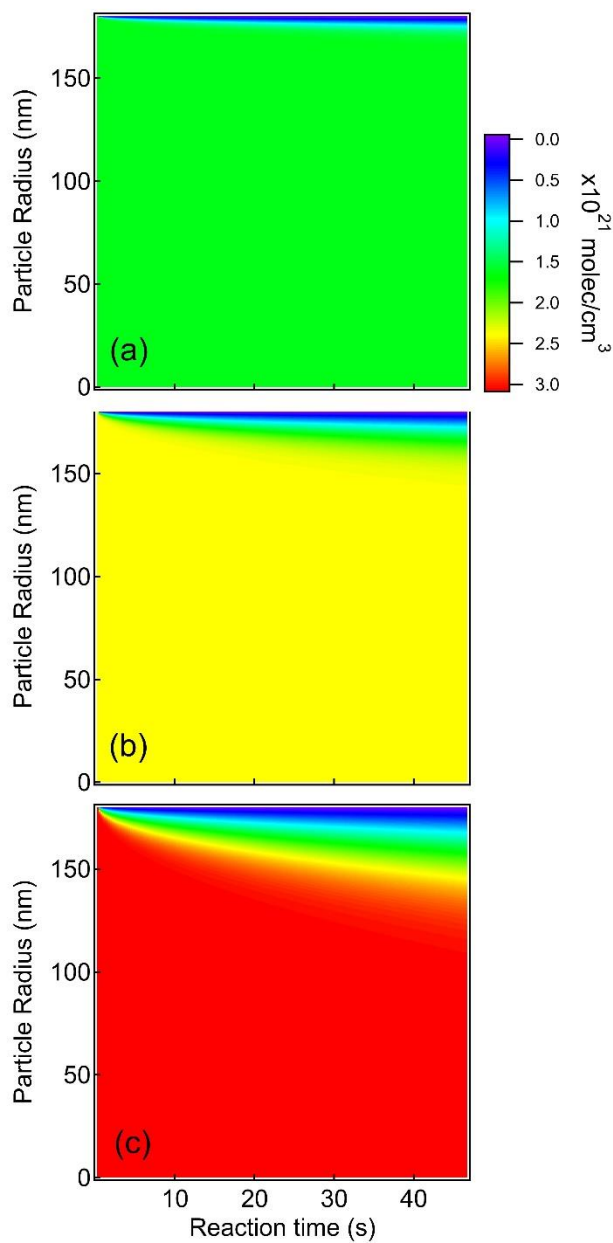
Figure 4. 12 Modeled space-time plots of concentration of MGP for MGP:lactose molar ratios of (a) 1:1 (b) 2:1 and (c) 4:1 with a constant OH gas number density of 8.70×10^{10} cm^{-3}. The particle radius is 180 nm and the reaction time is 46 s.

Figure 4.13 shows simulated radial distribution and temporal evolution of the bulk diffusion coefficient of MGP in homogeneous multiple component particle for the model parameters shown in Table 4.2 for MGP:lactose molar ratios of (a) 1:1, (b) 2:1, (c) 4:1. The diffusion coefficient of saccharides is assumed to initially have a radially homogeneous profile.

The radial heterogeneity of particle diffusion is established to follow the Vignes-type relationship through the radial concentration gradient of MGP component resulting from reaction shown in Figure 4.12. In Figure 4.13 (a), the diffusion coefficient of MGP near the surface within 10 nm remain largely unaffected by the oxidation process. In Figure 4.13 (b), a diffusion coefficient gradient of MGP is observed within the top 25 nm of the particle. The diffusion coefficient of MGP is reduced by a factor of 40 from the inner core of particle compared to the surface of particle. Figure 4.13 (c) shows a more pronounced MGP diffusion coefficient gradient than those at ratio 1:1 and 2:1. The observed diffusion gradient of MGP is within the outermost 50 nm of the particle. The diffusion coefficient of MGP is reduced by 2 orders of magnitude within the top 50 nm.
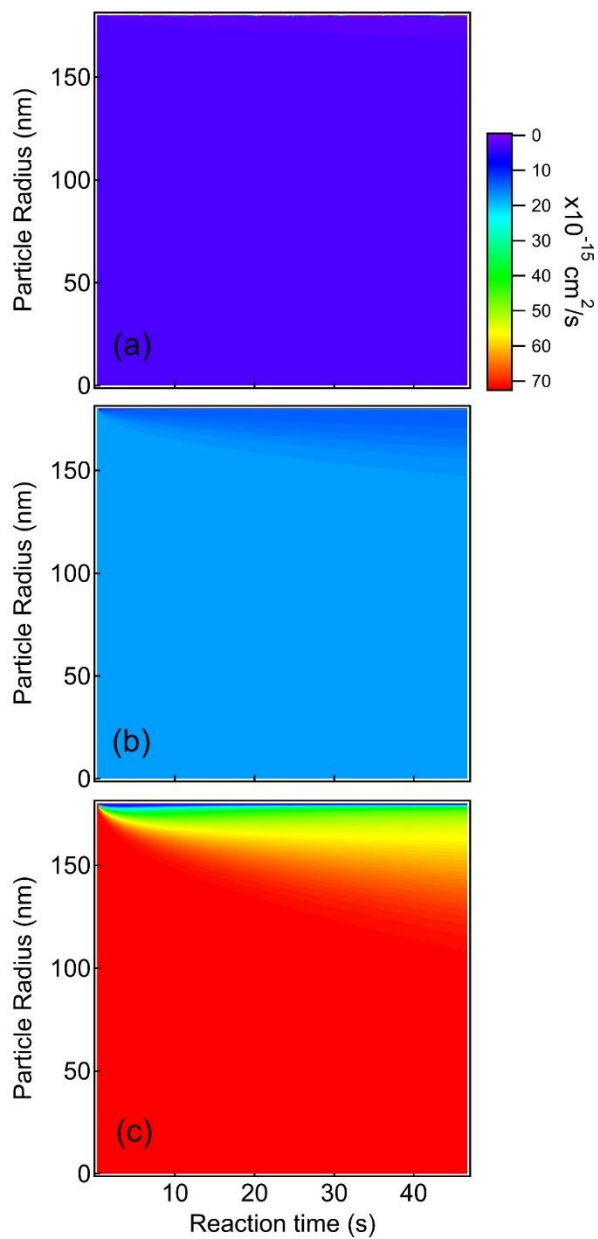
Figure 4. 13 Modeled space-time plots of diffusion coefficients of MGP for MGP:lactose molar ratios of (a) 1:1 (b) 2:1 and (c) 4:1 with a constant OH gas number density of 8.70×10^{10} cm^{-3}. The particle radius is 180 nm and reaction time is 46 s.

4.3 Discussion and implication for heterogeneous chemistry

In Table 4.1, as the MGP:lactose molar ratio is changed from 8:1 to 2:1, the value of γ_{MGP} is decreased by a factor of 2.4. In Table 4.2, as the MGP:lactose molar ratio is varied from 4:1 to 1:1, the value of γ_{MGP} is decreased by a factor of 5. From both VUV-AMS and GC-MS data analysis,

it shows that the reactant decay rate is greatly dependent on the bulk composition. In the semi-solid particles, diffusion of the reactant from the particle bulk to its surface is expected to be the rate limiting step. [1] These decay behaviors can be interpreted by examination of the diffusion coefficients of saccharide in the system. The presence of high molecular weight component (lactose) in the bulk phase increases the viscosity of particle, therefore it reduces the bulk diffusion in the semi-solid particles. [11] Our results are consistent with a previous study of the ozonolysis of maleic acid in the mixture of maleic acid-sucrose semi-solid particles. [14]

In the Table 4.2, the value of γ_{Lac} is smaller than that of the γ_{MGP} within 20% at ratio 1:1 and 2:1. This reactivity of lactose/MGP is consistent with the lactose/MGP diffusion: the diffusion coefficient of lactose is less than 20% smaller than that of MGP in the same particle based on using S-E relationship: the difference on diffusion constant among the species in the same matrix media is inversely proportional to their radius. However, at ratio 4:1, the value of γ_{Lac} is smaller than that of the γ_{MGP} by a factor of 7. In the model, it is found that the initial decay of saccharide reactant is not only limited by bulk diffusion but also the concentration of OH adsorbed onto the surface site of saccharide reactant. According to the S-E relationship, it is not possible that D_{Lac} is more than one order of magnitude slower than D_{MGP} in the same particle. In aqueous solution (as is the case for $D_{bulk} \geq 1\times10^{-6}$ cm^2 s^{-1}), the reactivity of OH toward MGP and lactose are similar. [6, 7, 15] Here the significant discrepancy between γ_{MGP} and γ_{Lac} is therefore unlikely to be due to differences in reactivity or bulk diffusion. It is more likely that there is less chance for OH radicals to react with the lactose molecules at the surface of the particle. In our MGP-lactose aqueous droplets with ratio of 1:1 study, we report a similar result: the value of γ_{Lac} is smaller than that of γ_{MGP} is by a factor of 13. The difference in MGP/lactose reactivity is due to there is a poor spatial overlap between the OH radicals and lactose at the gas-liquid interface since lactose has an exclusion layer of ~1 nm at the interface. [16] The semi-solid MGP-lactose particles with ratio of 4:1 have a relatively low viscosity, which explains the product glucose signal starts to be detected in the condensed phase. Here the bulk diffusion (as is the case for $D_{bulk} \geq 1\times10^{-13}$ cm^2 s^{-1}) may be fast enough for partitioning of bulk reactant at the interface and in the bulk to happen. A relative high amount of MGP and the increase production of glucose near the surface may replace lactose to react with OH radicals at the gas-solid interfaces. In the model, the concentration of lactose at the surface of particle is reduced to be half of its bulk concentration in order to simulate the partitioning of lactose

at the gas-solid interface. The simulation result is able to reproduce the observed lactose decay behavior at ratio 4:1.

Slow D_{MGP} leads to a concentration gradient of MGP within the particle illustrated in Figure 4.12. That the MGP concentration at the surface of the particle is getting close to zero after reaction of 46 s is only observed in the semi-solid MGP-lactose particles with ratio of 1:1. Here the replenishment of MGP at the surface of particle is not competitive against surface reaction loss due to slow D_{MGP} (as is the case for $D_{bulk} \leq 3 \times 10^{-15}$ cm^2 s^{-1}). At ratio 4:1, the MGP concentration gradient within the top ~50 nm of the particle decreases by 3 orders of magnitude. A relatively fast D_{MGP} (as is the case for $D_{bulk} \geq 1 \times 10^{-13}$ cm^2 s^{-1}) leads to efficient amount of MGP react with OH radicals at the surface of particle.

Figure 4.13 shows the evolution of MGP diffusivity in the bulk of semi-solid MGP-lactose particle, which illustrates the extent of slow bulk diffusion close to the particle surface. This gradient of bulk diffusion is established through a change to the MGP mole fraction in the particle resulting from the difference on reactivity between MGP and lactose in the particle. The steepness of diffusion gradient is more pronounced at ratio 4:1. This is attributed to consider the surface mole fraction of partitioning component. The time-space MGP diffusivity distribution suggests that chemical oxidation processes in more complex semi-solid organic particles containing high-molecule-weight species induce a slow diffusion at the diffusion "front", which accounts for solidifying effect. This will be particularly important as the molecular components become more oxidized in semi-solid multi-component particles with a relatively low viscosity ($D_{bulk} \geq 1 \times 10^{-13}$ cm^2 s^{-1}).

Isaacman et al reported that the reactive uptake coefficients of hydrocarbons in the motor oil particles are structure dependent. [17] The logarithm of the relative abundance of hydrocarbons as a function of OH exposure display steeper slopes, which indicate faster reaction rates. It is the rate of surface reaction rather than the diffusion rate (bulk to surface) determining the oxidation reaction rate in the motor oil particles.

In the atmospheric semi-solid aerosols, the presence of high-molecular-weight molecule species is responsible for significantly reduced the viscosity of these complex mixture particles. As the oxidation goes forward, the less reactive large molecule species remaining at the surface

induce a particle surface viscosity decrease followed by forming a "hard skin" at the outer layer of particle. This "hard skin" acts as a protective shell against the oxidative aging process, which shields the reactive species underneath the surface reacting with gas phase oxidants, and thus the aged aerosols survive long in the atmosphere.

4.4 Conclusion

The reactive uptake coefficients of the OH-initiated heterogeneous oxidation of semi-solid MGP-lactose particles reveals that the value of γ_{MGP} is decreased by a factor of 5 as the mole fraction of lactose is increased from 20% to 50%. Such a behavior is expected for molecules in the semi-solid particles where the bulk diffusion of reactants is the rate-limiting step. The D_{MGP} is lowered by the viscosity of the particles with the increasing mole fraction of lactose. The difference in the values of γ_{MGP} and γ_{Lac} appear to be consistent with the difference between D_{MGP} and D_{Lac} at ratio 1:1 and ratio 1:1 study. The observed uptake coefficients suggest that the reactivity difference among the molecule species in the relatively high viscosity of semi-solid particles ($D_{bulk} < 1 \times 10^{-14}$ cm^2 s^{-1}) can be estimated by its molecular size. However, in the case of semi-solid particles with relatively low viscosity ($D_{bulk} \geq 1 \times 10^{-13}$ cm^2 s^{-1}), the value of γ_{Lac} is smaller than that of γ_{MGP} by a factor of 7. The simulations suggest that the observed low reactivity of lactose is limited by a relative low surface mole fraction of lactose due to partitioning toward the bulk of particle.

A simple Vignes relationship has been successfully applied to estimate the bulk diffusion within semi-solid MGP-lactose particles at 30% RH over a range of molar ratio between MGP and lactose. The model is capable to treat the changes in bulk diffusion account for composition dependence. The observed kinetics are consistent with the slow composition-dependent bulk diffusion, leading to a gradient concentration of reactive species across the particle. The gradient diffusion of reactive species near the surface bulk illustrates that a "hard skin" formed during oxidative aging of semi-solid particles, which would pronouncedly reduce the chemical loss rates in aging semi-solid particles at long reaction times. The kinetics and simulation results provide valuable insight into the influence of bulk components in determining diffusivity properties within semi-solid organic particles and the role of composition-dependent bulk diffusion in regulating the rate of heterogeneous oxidation of semi-solid organic particles.

References:

1.   Fan, H.; Tinsley, M. R.; Goulay, F., Effect of Relative Humidity on the OH-Initiated Heterogeneous Oxidation of Monosaccharide Nanoparticles. *The Journal of Physical Chemistry A* **2015,** *119* (45), 11182-11190.

2.   Atkinson, R., Kinetics of the gas-phase reactions of OH radicals with alkanes and cycloalkanes. *Atmos. Chem. Phys.* **2003,** *3* (6), 2233-2307.

3.   Smith, G. D.; Woods, E.; Baer, T.; Miller, R. E., Aerosol Uptake Described by Numerical Solution of the Diffusion−Reaction Equations in the Particle. *The Journal of Physical Chemistry A* **2003,** *107* (45), 9582-9587.

4.   Wiegel, A. A.; Liu, M. J.; Hinsberg, W. D.; Wilson, K. R.; Houle, F. A., Diffusive confinement of free radical intermediates in the OH radical oxidation of semisolid aerosols. *Physical Chemistry Chemical Physics* **2017,** *19* (9), 6814-6830.

5.   Vieceli, J. R., M.; Potter, N.; Dang, L. X.; Garrett, B. C. and Tobias, D. J. , Molecular Dynamics Simulations of Atmospheric Oxidants at the Air−Water Interface: Solvation and Accommodation of OH and O3. *J. Phys. Chem. B.* **2005,** (109), 15876-15892.

6.   Bucknall, T.; Edwards, H. E.; Kemsley, K. G.; Moore, J. S.; Phillips, G. O., The formation of malonaldehyde in irradiated carbohydrates. *Carbohydrate research* **1978,** *62* (1), 49-59.

7.   Zakatova, N. V. M., D. P. and Sharpatyi, V. A., Role of OH-radicals in the radiolytic decomposition of carbohydrates and polysaccharides. *Bull. Acad. Sci. USSR, Div. Chem. Sci. (Engl. Tran)* **1969**.

8.   Davies, J. F.; Wilson, K. R., Raman Spectroscopy of Isotopic Water Diffusion in Ultraviscous, Glassy, and Gel States in Aerosol by Use of Optical Tweezers. *Analytical Chemistry* **2016,** *88* (4), 2361-2366.

9.   Vignes, A., Diffusion in Binary Solutions. Variation of Diffusion Coefficient with Composition. *Industrial & Engineering Chemistry Fundamentals* **1966,** *5* (2), 189-199.

10.   Peng, C.; Chow, A. H. L.; Chan, C. K., Hygroscopic Study of Glucose, Citric Acid, and Sorbitol Using an Electrodynamic Balance: Comparison with UNIFAC Predictions. *Aerosol Science and Technology* **2001,** *35* (3), 753-758.

11.   Song, Y. C.; Haddrell, A. E.; Bzdek, B. R.; Reid, J. P.; Bannan, T.; Topping, D. O.; Percival, C.; Cai, C., Measurements and Predictions of Binary Component Aerosol Particle Viscosity. *The Journal of Physical Chemistry A* **2016,** *120* (41), 8123-8137.

12.	Lide, D. R., *CRC Handbook of Chemistry and Physics*. 64th ed.; CRC Press: Boca Raton: FL, 1983.

13.	Mai, H.; Shiraiwa, M.; Flagan, R. C.; Seinfeld, J. H., Under What Conditions Can Equilibrium Gas–Particle Partitioning Be Expected to Hold in the Atmosphere? *Environmental Science & Technology* **2015,** *49* (19), 11485-11491.

14.	Marshall, F. H.; Miles, R. E. H.; Song, Y.-C.; Ohm, P. B.; Power, R. M.; Reid, J. P.; Dutcher, C. S., Diffusion and reactivity in ultraviscous aerosol and the correlation with particle viscosity. *Chemical Science* **2016,** *7* (2), 1298-1308.

15.	Ribeiro, A. C. F.; Ortona, O.; Simões, S. M. N.; Santos, C. I. A. V.; Prazeres, P. M. R. A.; Valente, A. J. M.; Lobo, V. M. M.; Burrows, H. D., Binary Mutual Diffusion Coefficients of Aqueous Solutions of Sucrose, Lactose, Glucose, and Fructose in the Temperature Range from (298.15 to 328.15) K. *Journal of Chemical & Engineering Data* **2006,** *51* (5), 1836-1840.

16.	Fan, H.; Wenyika Masaya, T.; Goulay, F., Effect of surface–bulk partitioning on the heterogeneous oxidation of aqueous saccharide aerosols. *Physical Chemistry Chemical Physics* **2019,** *21* (6), 2992-3001.

17.	Isaacman, G.; Chan, A. W. H.; Nah, T.; Worton, D. R.; Ruehl, C. R.; Wilson, K. R.; Goldstein, A. H., Heterogeneous OH Oxidation of Motor Oil Particles Causes Selective Depletion of Branched and Less Cyclic Hydrocarbons. *Environmental Science & Technology* **2012,** *46* (19), 10632-10640.

Chapter Five

Effect of Surface–bulk Partitioning on the Heterogeneous Oxidation of Aqueous Saccharide Aerosols

Chapter 5: Effect of surface partitioning on the heterogeneous oxidation of saccharide aerosols

In the present study, we have characterized the OH-initiated heterogeneous oxidation of equimolar mixed aqueous aerosols of two non-surface-active saccharides: a monosaccharide, β-methyl glucopyranoside (MGP), and a disaccharide, lactose, using an atmospheric-pressure flow tube at room temperature. The relative concentrations of the aerosol reactants and primary products are monitored by off-line analysis as a function of the time-integrated total concentration of OH radical. We found that the kinetic traces of the monosaccharide and disaccharide reactants are significantly different. To gain more detailed insights into this mechanism, Molecular dynamics simulations were carried out, allowing for prediction of concentration profiles of reactants near the air-water interface. Stochastic simulations using a simplified chemical model were also performed to support the interpretation of the data. Our experimental results appear to be consistent with the formation of a ~1 nm exclusion layer of disaccharides at the particle surface resulting in a more probable reaction of the monosaccharide with the OH radical.

5.1 Experimental results

5.1.1 Kinetic results

5.1.1.1 OH oxidation of MGP-lactose aqueous droplets kinetics result

Figure 5.1 shows the relative decay of MGP (red filled circles) and lactose (black filled squares) in MGP-lactose aqueous droplets as a function of OH exposure. Each point is the mean value obtained by triple GC-MS analysis of two particles samples. The error bars represent the maximum and minimum experimental values. The apparent disappearance rate constants for the MGP and lactose in the MGP-lactose aqueous droplets are determined from an exponential fit with all the experimental data. The observed decay rate for MGP is $(4.67\pm1.04)\times10^{-12}$ cm^3 s^{-1} and for lactose is $(3.44\pm0.85)\times10^{-13}$ cm^3 s^{-1}. The error bars are 2-stardard deviations from the fit. The good exponential fit of the MGP decay trace suggests that the reaction proceeds under pseudo first order conditions where diffusion of the reactants is not the rate limiting phenomena in aqueous droplets. Here the decay rate value of MGP in aqueous droplets is close to that of MGP measured in aqueous solution (k_{OH+MGP}=5.31×10^{-12} cm^3 s^{-1}). [1] The decay rate of lactose is a factor of 10 times slower

than that of MGP. The reactive uptake coefficient for MGP is 5.02±1.12 which suggests that the reaction proceeds through a complex multistep radical chain mechanism, and the uptake coefficient for lactose is 0.39±0.10.
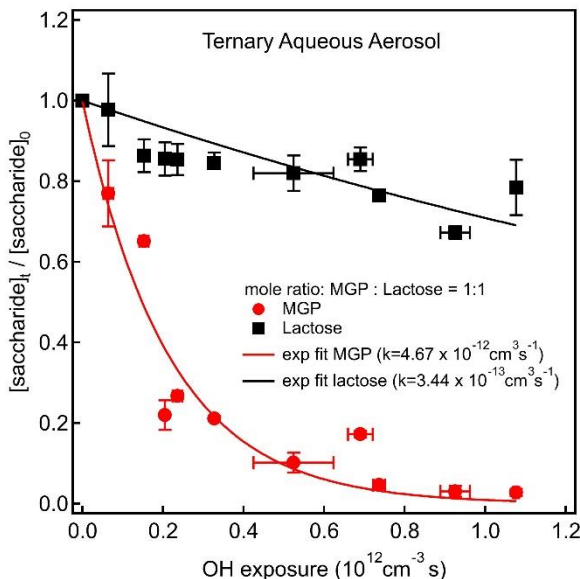
Figure 5. 1 Relative signal of unreacted saccharides in the MGP-lactose aqueous droplets as a function of OH exposure. The red filled circles are the normalized signal of MGP and the black filled squares are that of lactose. The fit lines are fitting all the experimental data to an exponential decay in order to determine the rate constant for the reaction of saccharides with OH. The decay rate for MGP+OH is (4.67±1.04) ×10^{-12} cm^3 s^{-1}. The decay rate for lactose+OH is (3.44±0.85) ×10^{-13} cm^3 s^{-1}

5.1.1.2 OH oxidation of lactose aqueous droplets kinetics result

Figure 5.2 shows the normalized decay of lactose in the lactose aqueous droplets as a function of OH exposure. The decay of lactose follows a biexponential decay behavior with the shape $Ae^{-k_{fast}\cdot<OH>_t\cdot t}+Be^{-k_{slow}\cdot<OH>_t\cdot t}$. The first component represents an acute fast-decaying lactose, with an initial fast decay rate constant k_{fast} and the second component represents a slow-decaying lactose, with a slow decay rate constant k_{slow}. The apparent fast disappearance rate constant (k_{fast}) for the lactose in aqueous droplets is (9.58±3.25) ×10^{-12} cm^3 s^{-1}. The following slow disappearance rate constant (k_{slow}) is (1.56±1.52) ×10^{-13} cm^3 s^{-1}. Here the initial fast decay of the lactose reactant (k_{fast}) is of the same order of magnitude as that observed for the MGP (k_{MGP}= (4.67±1.04) ×10^{-12} cm^3 s^{-1}) in the MGP-lactose aqueous droplet kinetics result and corresponds to

an uptake coefficient of 7.75±3.25. The decay rate is found to decrease considerably for OH exposure larger than 2×10^{11} cm^{-3} s corresponding to an uptake coefficient of 0.13±0.12. The rate constants and uptake coefficients obtained from fit to the data are shown in Table 5.1
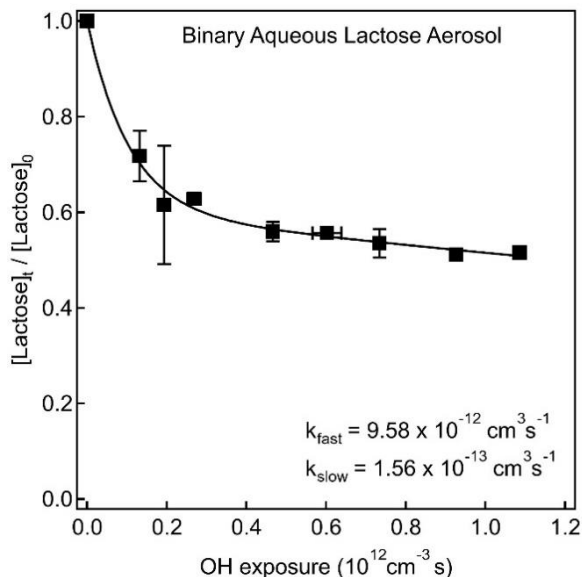
Figure 5. 2 Relative signal of unreacted lactose in binary aqueous-lactose droplet as a function of OH exposure. The black line is a biexponential fit with the shape $Ae^{-k_{fast}.<OH>_t.t}+Be^{-k_{slow}.<OH>_t.t}$. The arrested initial fast decay rate of lactose (k_{fast}) is (9.58±3.25) ×10^{-12} cm^3 s^{-1}. The following slow decay rate of lactose (k_{slow}) is (1.56±1.52) ×10^{-13} cm^3 s^{-1}.

Table 5. 1 Rate constants and uptake coefficients for heterogeneous oxidation of saccharides aqueous droplet with OH radicals.

Molar ratio (MGP:lactose)	Rate constant $k_{MGP}±2\sigma$ (cm^3 molecule^{-1} s^{-1})	Uptake coefficient ($\gamma_{MGP}±2\sigma$)	Rate constant $k_{Lac}±2\sigma$ (cm^3 molecule^{-1} s^{-1})	Uptake coefficient ($\gamma_{Lac}±2\sigma$)
0:1	----------	-----------	9.58±2.01 ×10^{-12} (fast decay) 1.56±1.52 ×10^{-13} (slow decay)	7.75±3.25 (fast decay) 0.13±0.12 (slow decay)
1:1	4.67±1.04 ×10^{-12}	5.02±1.12	3.44±0.85 ×10^{-13}	0.39±0.10

5.1.2 Particle size characterization

Figure 5.3 displays the surface-weighted particle size distribution for aqueous saccharide droplets. The particle sizer scan of aqueous saccharide droplets is from unreacted sample obtained in the MGP-lactose aqueous droplets (red dashed line) measurement and in the lactose aqueous droplets (black dashed line) measurement. The average of particle surface-weighted diameter is about 360 nm.
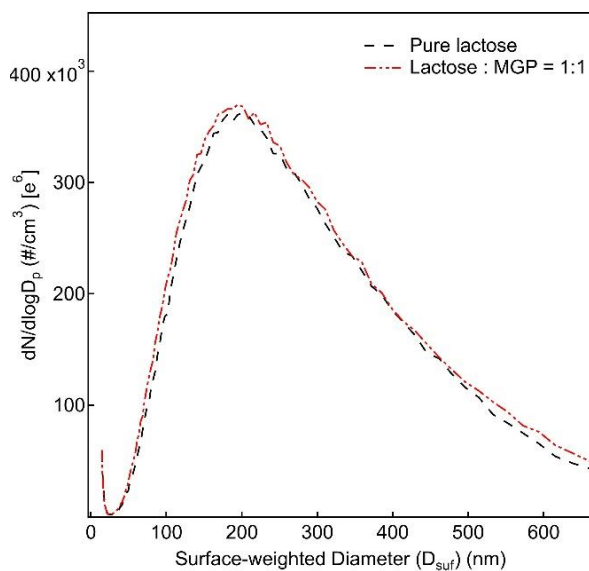
Figure 5. 3 Surface-weighted particle size distribution for unreacted saccharides containing aqueous droplets. Pure lactose droplets (black dashed line): the mean surface-weighted diameter is 361.8 nm, and the total concentration of number particle size is 2.32×10^5 #/cm^3. Equimolar MGP-lactose aqueous droplets (red dashed line): the mean surface-weighted diameter is 365.4 nm, and the total concentration of number particle size is 2.46×10^5 #/cm^3.

5.1.2.1 Evolution of MGP-lactose aqueous droplets characterization

Figure 5.4 displays relative surface weighted diameter (red solid circles) and relative single particle mass fraction (relative ratio of total mass/total number concentration, black solid circles) remaining as a function of OH exposure obtained in the MGP-lactose aqueous droplets measurement. These data are measured by Scanning Mobility Particle Sizer (SMPS) measurement. The error bars are two standard deviation about four times particle size data measurements. There is no significant decrease on surface-weighted mean diameter as function of OH exposure. There

is a slight increase within 20% on relative single particle mass fraction up to OH exposure of 2×10^{11} cm^{-3} s then decrease to be a ratio value of 1.0.
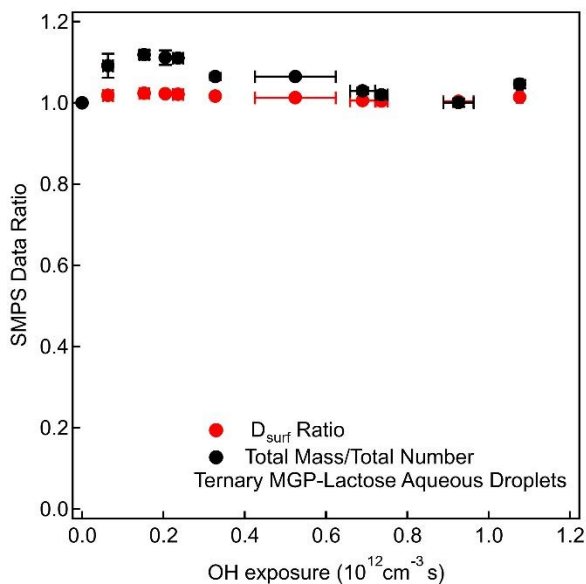
Figure 5. 4 Relative surface weighted diameter (red solid circles) and relative single particle mass fraction remaining (black solid circles) as a function of OH exposure obtained in the MGP-lactose aqueous droplets measurement. The error bar is 2σ about mean value.

5.1.2.2 Evolution of lactose aqueous droplets characterization

Figure 5.5 displays relative surface weighted diameter (red solid circles) and relative single particle mass fraction (relative ratio of total mass/total number concentration, black solid circles) remaining as a function of OH exposure obtained in the lactose aqueous droplets measurement. These data are measured by Scanning Mobility Particle Sizer (SMPS) measurement. The error bars are two standard deviation about four time particle size data measurement. There is no significant changes on surface-weighted mean diameter and relative single particle mass fraction as function of OH exposure.
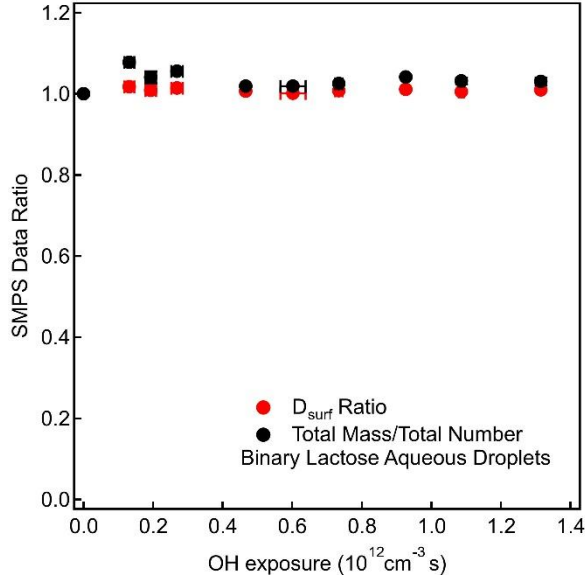
Figure 5. 5 Relative surface weighted diameter (red solid circles) and relative single particle mass fraction remaining (black solid circles) as a function of OH exposure obtained in the lactose aqueous droplets measurement. The error bar is 2σ about mean value.

5.1.3 Products identification

5.1.3.1 OH oxidation of MGP-lactose aqueous droplets study

The first-generation product of oxidation lactose with OH, glucose is detected in the condensed phase by GC-MS. Figure 5.6 shows the normalized glucose signal (blue solid triangles) as a function of OH exposure obtained in the MGP-lactose aqueous droplets kinetics measurement. The normalized signal S for glucose is fit to the following double exponential equation as a function of OH exposure $< OH >_t.t$:

$$S\left(< OH >_t.t\right) = \left(\frac{k_1}{k_2 - k_1}\right).\left(e^{-k_1.<OH>_t.t} - e^{-k_2.<OH>_t.t}\right) \qquad (1)$$

The kinetics rate k_1 and k_2 are second-order rate constants for the rise and decay of glucose. The formation rate coefficient k_1 is set to that of the MGP decay observed in Figure 5.1. The fit to the data returns a rate coefficient k_2 of $9.37(\pm3.30) \times10^{-13}$ cm^3 s^{-1} for the glucose oxidation.
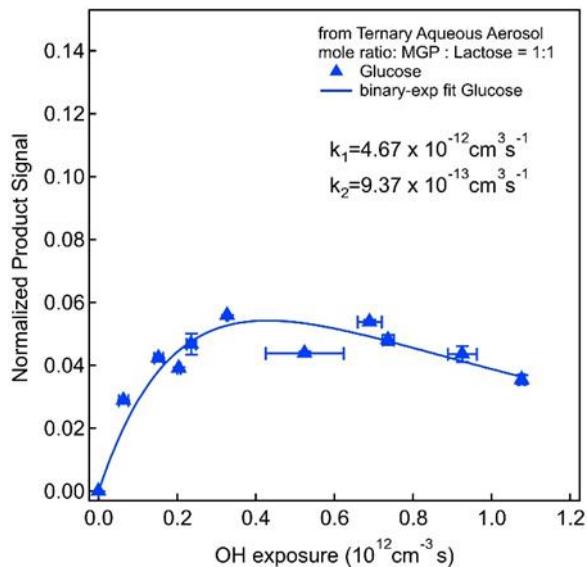
Figure 5. 6 Normalized yields of the detected glucose in the MGP-lactose aqueous droplets as a function of OH exposure. The blue line is fitting all the experimental data points with a double exponential function. k_1 is set as 4.67 $\times 10^{-12}$ cm^3 s^{-1}, which is rate constant for the reaction of MGP with OH in the MGP-lactose aqueous droplets. k_2 is 9.37×10^{-13} cm^3 s^{-1} in order to best fit the observed trend.

5.1.3.2 OH oxidation of lactose aqueous droplets study

Figure 5.7 shows the normalized glucose signal (blue solid triangles) exhibits a double exponential behavior with the shape $\left(\frac{k_1}{k_2-k_1}\right) \cdot (e^{-k_1 \cdot <OH>_t \cdot t} - e^{-k_2 \cdot <OH>_t \cdot t})$ as a function of OH exposure as shown in Eq. (1). The glucose signals are observed during the oxidation of lactose aqueous aerosols. The rate constant for the rise of glucose, k_1 is set to be the observed disappearance rate constant for lactose in the lactose aqueous droplets, 9.58×10^{-12} cm^3 s^{-1}. The rate constant for the decay of glucose, the return k_2 is 1.30 (± 0.54) $\times 10^{-12}$ cm^3 s^{-1} in order to fit the observed behavior. The summary of fitted k_1 and k_2 for the evolution of normalized glucose signals identified in both ternary aqueous-MGP-lactose droplets and binary aqueous-lactose droplets is in Table 5.2.

94

Table 5. 2 The fitted kinetic parameters for the evolution of normalized glucose signals identified in both the MGP-lactose aqueous droplets and the lactose aqueous droplets.

Molar ratio (MGP:lactose)	Formation rate constant for glucose $k_1 \pm 2\sigma$ (cm^3 molecule^{-1} s^{-1})	Loss rate constant for glucose $k_2 \pm 2\sigma$ (cm^3 molecule^{-1} s^{-1})
0:1	$9.58 \pm 2.01 \times 10^{-12}$	$9.37 \pm 3.30 \times 10^{-13}$ cm^3 s^{-1}
1:1	$4.67 \pm 1.04 \times 10^{-12}$	$1.30 \pm 0.54 \times 10^{-12}$ cm^3 s^{-1}
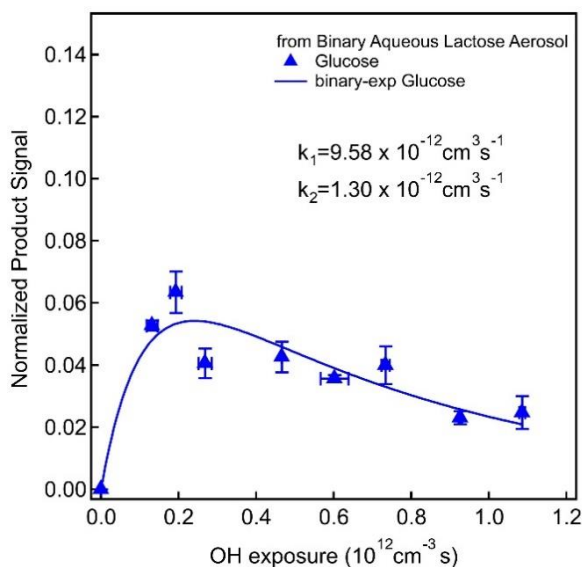
Figure 5. 7 Normalized signal of detected glucose in the lactose aqueous droplets as a function of OH exposure. The blue line is a double exponential fit with the shape $\left(\frac{k_1}{k_2-k_1}\right) \cdot (e^{-k_1 \cdot <OH> \cdot t} - e^{-k_2 \cdot <OH> \cdot t})$ to all the experimental data. The rate constant for the rise of glucose k_1 is 9.58×10^{-12} cm^3 s^{-1}, which is rate constant for the reaction of lactose with OH in binary aqueous-lactose aerosol. k_2, the rate constant for the decay of glucose is 1.30×10^{-12} cm^3 s^{-1} in order to fit the observed trend.

5.2 Molecular perspective of gas-liquid interfaces: learned from dynamic simulation results

Molecular dynamics simulation (performed by T.M. Masaya) are applied to quantify the saccharides partitioning at the interface and estimate the length of the lactose exclusion layer. The

averaged normalized atoms occurrence profiles were obtained from analyzing a 110 ns production run for water, MGP, and lactose for 4 independent runs. Figure 5.8 displays the MGP and lactose profiles within the first 15 Å (1.5 nm) of the surface. The shading areas are one-standard deviation about the mean from the averaging of 4 independent profiles. The MGP and Lactose profiles are normalized to the area under the curves. The ratio between the areas of the water and saccharide profiles is kept to the ratio of water-to-saccharide molecules in the simulations. After 110 ns of simulation, the water molecules diffuse outside their initial boundaries. The position of the water surface is determined on both sides of the simulation box by the location at which the water profile derivative reaches 1% of its maximum value. The saccharide occurrence close to the water surface remains greater for MGP than for lactose. The MGP profile is found to be low at the surface and to increase rapidly within the first 10 Å (1 nm) of the air-water interface. The lactose profile is found to rapidly decrease close to the surface, generating an exclusion layer with no or very low lactose occurrence of up to 10 Å (1 nm). [2]
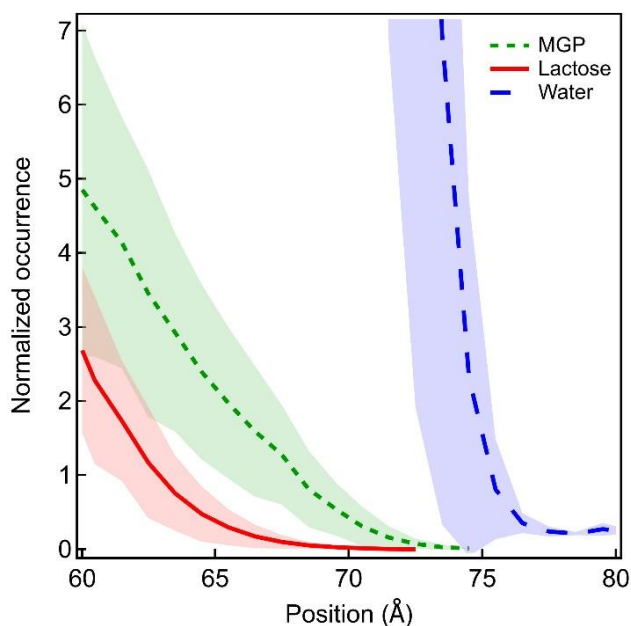
Figure 5. 8 Simulated averaged number of atoms occurrence at a given location found after analyzing a 110ns production simulation run for water (blue dashed line), MGP (green dotted line), and lactose (solid red line) for 4 independent runs within 15 nm of the water surface. The shading areas are one standard deviation about the mean from the 4 independent profiles. The MGP and Lactose profiles are normalized by the area under the curve. [2]

5.3 Reaction-diffusion kinetic model development

5.3.1 Stochastic model overview

A reaction-diffusion kinetic model was developed using Kineticscope software in order to investigate role of air-water interface plays in bulk aqueous chemistry. [3, 4] (http://hinsberg.net/kineticscope) The particle is modeled with a radius of 100 nm. A stack of 200 individual 100×100 nm compartments that are 0.5 nm thick represents the center of particle to the surface of the particle. The outermost compartment represents the gas-particle interface and beneath of that represents the bulk region of the aerosol. A reactive site is defined as a MGP, lactose, or glucose molecule in the compartment. Species (i.e. molecules) can diffuse forward and back between the compartments. In order to simulate the partitioning of lactose at the gas-particle interface, lactose is allowed to diffuse only downward in the gas-particle interface. The number of outermost compartments selected as gas-particle interface represents the thickness of lactose exclusion layer in the surface of the aerosol. The diffusion coefficient of organic material for dilute aqueous solution is about 10^{-5} cm^2 s^{-1}. [5] Such high diffusion coefficient will lead to a very long simulation. Here the diffusion coefficients of MGP and lactose are applied on the order of 10^{-10} cm^2 s^{-1} which still lead to a well-mixed particle within a few microseconds. In order to have a shorter simulation, the bulk concentration of MGP and lactose are set only 1×10^{16} cm^{-3}, two orders of magnitude smaller than the experimental number density. The OH gas density is of the order of 1×10^{11} cm^{-3} and the total reaction time is 10s corresponding to an overall OH exposure of 1×10^{12} cm^{-3} s^{-1}. The summary of reaction and diffusion parameters used in the stochastic simulation is listed in the Table 5.3. Within each compartment, elementary chemical reaction steps describe the reaction of OH with MGP, lactose and glucose. The reaction rate coefficients for each elementary chemical reaction are set as that of aqueous solution. The chemistry is described as follows:

$$OH_g + site \xrightarrow{k_{ad}} OH_{ad-site} \qquad \text{(R1)}$$

$$OH_{ad-site} \xrightarrow{k_{des}} OH_g + site \qquad \text{(R2)}$$

$$MGP + OH_{ad-site} \xrightarrow{k} Products \qquad \text{(R3)}$$

$$Lactose + OH_{ad-site} \xrightarrow{k} Glucose \qquad \text{(R4)}$$

$$Glucose + OH_{ad-site} \xrightarrow{k} Products \qquad \text{(R5)}$$

$$OH_g + site \xrightarrow{k_{ad}} OH_{ad-site} \qquad \text{(R6)}$$
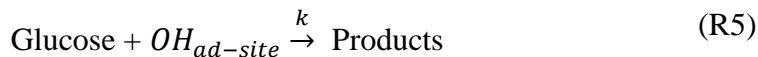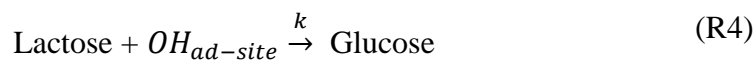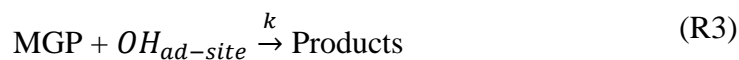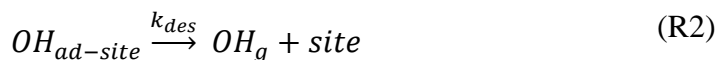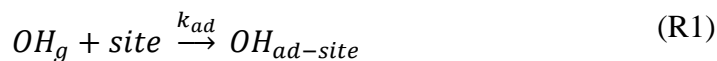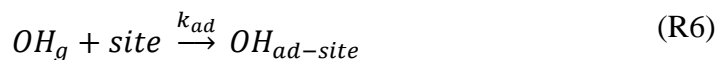
Table 5. 3 Reaction and diffusion parameters used in the stochastic simulation of the heterogeneous reaction of OH radicals with the MGP-lactose aqueous droplets.

	OH reaction rate coefficient (cm^3 s^{-1})	Bulk diffusion coefficient (cm^2 s^{-1})	OH adsorption rate (s^{-1})
MGP	5×10^{-12}	6.7×10^{-10}	100
Lactose	4×10^{-12}	4.9×10^{-10}	100
Glucose	5×10^{-12}	6.7×10^{-10}	100
Products	--	6.7×10^{-10}	--
OH	--	10.0×10^{-10}	--

5.3.2 Kinetic model results

Figure 5.9 shows the overlap integrated model profiles of unreacted saccharide with experimental data in the well-mixed droplet as a function of OH exposure. The simulation was run for different thickness of the lactose exclusion layer. The best match is for a layer of 2nm. The thickness of the lactose exclusion layer has only a minimum effect on the MGP decay profile but strongly affects the lactose decay. Thicker exclusion layers lead to no observable decay of the lactose over the considered OH exposure range.
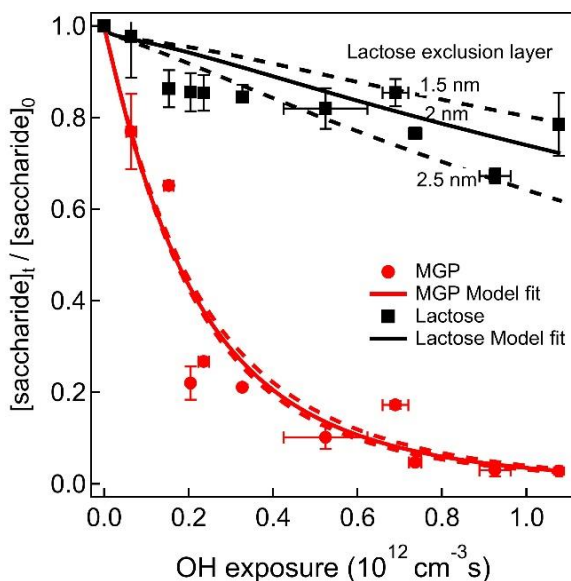
Figure 5. 9 Modeled mass of saccharides remaining in the aerosol as a function of OH exposure for MGP (red): lactose (black) a molar ratio 1:1 in aqueous droplet. All the lines are the modeled fit. A lactose exclusion layer of 2nm (solid line) is in a best agreement with the experimental data.

Figure 5.10 displays modeled space-time plots of lactose and MGP in the aqueous droplet (molar ratio 1:1) with a constant OH gas number density of 1×10^{11} cm^{-3}. The y-axis is the radial distance from the core of the aerosol particle. The x-axis is the reaction time. The concentration of lactose and MGP within the droplet are homogenous through the whole reaction due to the fast diffusion of saccharides in the dilute aqueous droplet. The MGP is approximately completely consumed within 6 s. The concentration of lactose starts to be significantly reduced after 6s. There is no lactose molecules within 2 nm of the surface of droplet through the whole reaction.
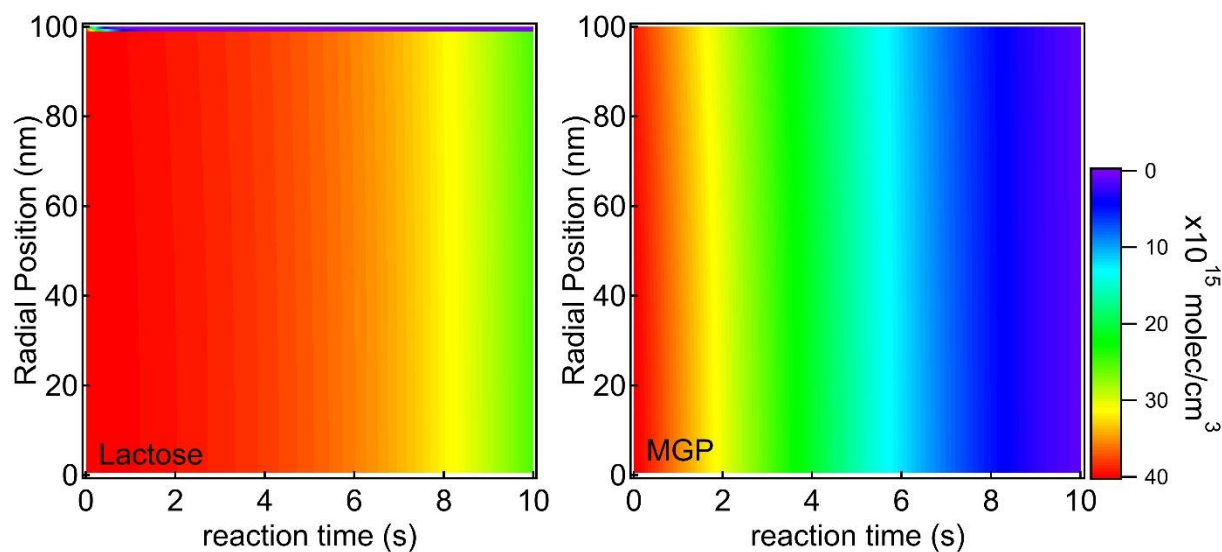
Figure 5. 10 Modeled space-time plots of concentration of lactose (left) and MGP (right) for Lactose:MGP a molar ratio of 1:1 aqueous droplet with a constant OH gas number density of 1×10^{11} cm^{-3}.

Figure 5.11 shows the number density of lactose (top, blue) and OH (bottom, red) as a function of the particle radius. The OH concentrations is found to decay very rapidly at the surface of the particle to reach zero after 3 to 4 nm. The lactose has an opposite profile. The poor overlap of the two profiles lead to a slow kinetic for OH+lactose reaction as only very few OH are reaching the lactose layer. The MD simulation in Figure 5.8 clearly shows that the MGP concentration is significantly higher at the interface than that of lactose. If the reaction rate of the OH radical with reactive species molecule at the gas-liquid interface is faster than that of the bulk reaction, then the

surface partitioning could lead to a large reactivity difference between the two saccharides. As the MGP diffusion to the interface is fast, the heterogeneous reaction rate will remain constant for MGP as the reaction progresses. At higher lactose and MGP number densities, the behavior is expected to remain the same although the dimension of the system will likely change. For a given OH exposure, higher MGP concentration in the particle could result in a slower lactose decay rate as more OH radicals react with the MGP at the interface. Keeping the lactose so far away from the surface is likely to lead to no reaction at all as the radical will react with the very concentrated MGP instead.
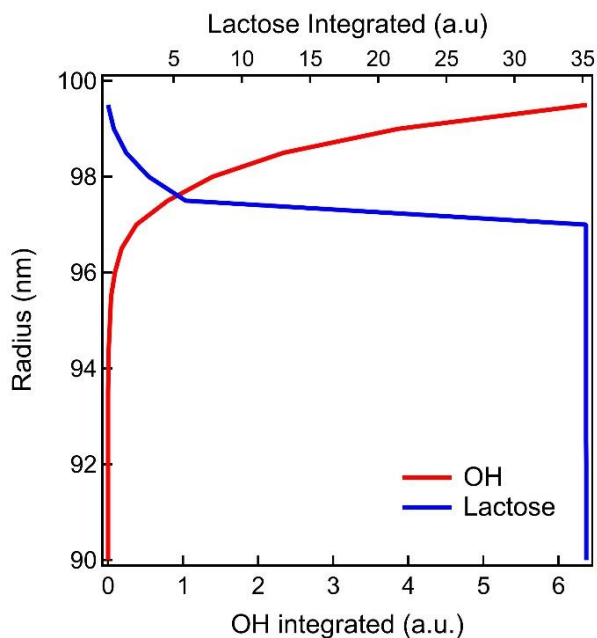
Figure 5. 11 The number density of lactose (top, blue) and OH (bottom, red) as a function of the particle radius.

5.4 Discussion and implication for atmospheric chemistry

Quantitative studies of surface tension increments (STI) of several polyols suggest that higher-order polyols like sucrose exhibits the largest positive STI (approximately completely excluded from the surface of water). [6] Figure 5.12 shows the polyol partitioning free energies is in an excellently linear dependence of solvent accessible surface area. The relationship between the partitioning free energy ΔG_p and surface-bulk partition coefficient $K_{p,2}$ can be related through the following equation:

$$\Delta G_p = -RT \ln K_{p,2} \tag{2}$$

Where surface-bulk partition coefficient for the solute ($K_{p,2} = m_2^\sigma / m_2^b$), defined as the molar concentration ratio between the solute in the air-water interface and solute in bulk. R is 8.314 J mol^{-1} K^{-1} and T is the temperature on the Kelvin scale. The linear fit of the partitioning free energy ΔG_p to the solvent accessible surface area (SASA) data not including sucrose is leading to:

$$\Delta_p G^o(\text{kCal mol}^{-1}) = \text{ASA}(\text{Å}^2) \times 0.013 - 3.08 \tag{3}$$

Figure 5.12 also displays the Gibbs free energies for MGP and lactose obtained using calculated SASA values and Eq. 3. The obtained ΔG_p values are 1.04 kCal mol^{-1} and 3.26 kCal mol^{-1} for MGP and lactose, respectively. For MGP this corresponds to a concentration at the interface about 6 times lower than that of the bulk. With a ΔG_p value higher than 3 kCal mol^{-1}, lactose is likely not to be found at the interface. The calculation suggests that $K_{p,2}$ for MGP is 38 times as much as that of lactose. Therefore, the concentration of MGP in the gas-particle interface is much higher than that of lactose.
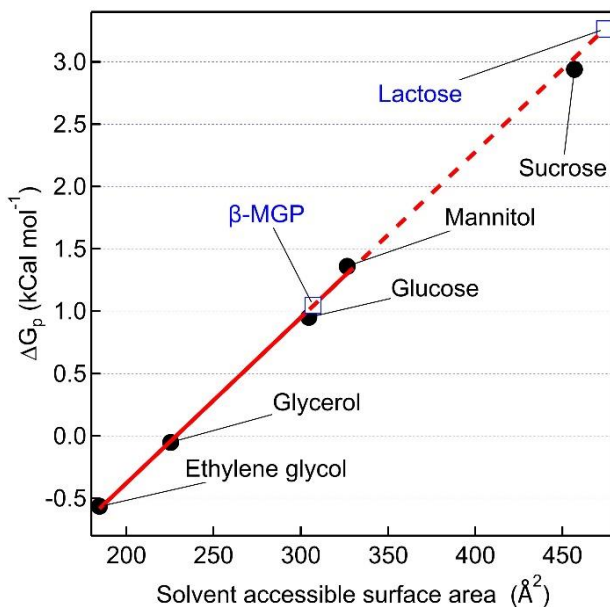
Figure 5. 12 The partitioning free energy ΔG_p for each polyol is plotted against the solvent accessible surface area (ASA) of that solute. The accessible solvent accessible surface area is calculated using Surface Racer 5 and the Gibbs free energy values (black dots) are from Pegran et al. [6] The solid red line is a linear fit (Eq. 3.) to the data up to

mannitol and extrapolated (red dashed line) up to lactose. The blue squares are interpolated and extrapolated Gibbs free energy values for MGP and lactose based on their calculated solvent accessible surface area.

For aqueous phase chemistry study, as Figure 5.1 shows the decay rate of lactose is about 10 times slower than that of MGP in the MGP-lactose aqueous droplets with a molar ratio 1:1. The reaction rate constant for OH+lactose and OH+MGP are almost the same in the aqueous solution. The decay rate of OH+MGP measured in aqueous droplet is close to the reaction rate of OH+MGP in aqueous solution. The reactive uptake coefficient observed for the MGP reactant is 5.02 ± 1.12, which indicates a complex radical chain reaction where the OH radical is not the sole reactive species in the aqueous droplet. In aqueous droplets, where the diffusion is not a rate limiting step these radicals are likely to be present at the air-water interface as well as in the bulk. The reaction scheme may lead to a wide range of products with different partitioning properties. It is possible that some of these products have a higher affinity toward the air-water interface therefore limiting the access of the OH radical to the high lactose concentration in the bulk.

The binary aqueous lactose study is shown in Figure 5.2 and Figure 5.7. The fast-decaying rate of lactose starts to slow down where the product glucose signal rises the maximum at the OH exposure of 0.2×10^{12} molecule cm^{-3} s^{-1}. The fast-decaying rate of lactose (k_{fast}=(9.58$\pm$3.25) $\times10^{-12}$cm^{3}s^{-1}) is the same order of magnitude of the reaction rate of OH+lactose ($k_{OH+lactose}$=5.15$\times10^{-12}$ cm^3 s^{-1}) in aqueous solution. The slow-decaying rate of lac constant (k_{slow}= (1.56$\pm$1.52) $\times10^{-13}$ cm^3 s^{-1}) is close to that measured (k_{Lac}=(3.44$\pm$0.85) $\times10^{-13}$ cm^3 s^{-1}) in ternary aqueous-MGP-lactose droplets in Figure 5.1. The biexponential decays observed for the OH oxidation of binary aqueous-lactose droplets may be attributed to the formation of glucose as an oxidation product, migrating toward the interface, between the lactose and the surface.

The fitted formation rate of glucose in the MGP-lactose aqueous droplets in Figure 5.6 is fixed with the value of decay rate of MGP (k_{MGP}=(4.67$\pm$1.04) $\times10^{-12}$ cm^3 s^{-1}) obtained in Figure 5.4. The fitted formation rate of glucose in binary aqueous-lactose droplets in Figure 5.7 is fixed with value of initial fast decay rate of lactose (k_{fast}=9.58$\times10^{-12}$ cm^3 s^{-1}) obtained in the Figure 5.1. Both of the formation rates of glucose are the same order of magnitude as the reaction rate of lactose ($k_{OH+lactose}$=5.15$\times10^{-12}$ cm^3 s^{-1}) in aqueous solution. Both of the return decay rates of glucose are close to the order of magnitude as the decay rate of MGP measured in aqueous droplets.

This result is consistent with the similar reactive species with a similar partitioning coefficient at the interface.

The experimental observed decay rates of both MGP and lactose combined with the molecular dynamic simulations suggest that partitioning could play a significant role on the reactivity of reactive species in aqueous aerosols. For well-mixed mixture particles, the reactive species molecules could compete to react with gas-phase oxidation at the gas-liquid interface which depends on the propensity of the reactive molecules to transport into the interface. This is particularly important as the molecular components become more oxidized with products generated.

Wan and Yu [7] have reported the saccharide and polyols composition of atmospheric aerosols collected in urban centers in Hong Kong. The amount of levoglucosan, xylose, and fructose in the atmospheric aerosols are the most abundant monosaccharides during all the seasons. Disaccharides (trehalose) and trisaccharide (melezitose) are also found in the atmospheric aerosols in the fall season. Table 5.4 shows the SASA for these detected saccharides and the corresponding partitioning Gibbs free energy calculated using a linear fit equation (Eq. 3.) from the data reported by Pegran et al., and the fall abundance relatively to levoglucosan. [5, 6]

Table 5. 4 Relative abundance, solvent accessible surface area, and partitioning Gibbs free energy for detected saccharide in atmospheric aerosols. [7]

Saccharide	Relative abundance in aerosols	ASA (Å^2)	$\Delta_p G^o$ (kCal mol^{-1})
Levoglucosan	1	268.78	0.41
Xylose	0.98	276.39	0.51
Fructose	0.21	311.12	0.97
Trehalose	0.02	445.18	2.71
Melezitose	0.14	635.02	5.18

All the detected saccharides in Table 5.4Table 5. 4 display a positive Gibbs free energy and may be characterized as surface inactive compounds. The extrapolated values of $\Delta_p G^o$ spam a very broad range corresponding to partitioning constants between 0.5 for levoglucosan and $1.6 \times 10^-$

[4] for the trisaccharide melozitose. In such mixed particles, levoglucosan is present at the interface with relatively high concentrations while the trisaccharide is restricted to the bulk, likely with a large (>1 nm) exclusion layer. Because of the large range of partitioning properties, the interface displays a gradient of concentrations for each saccharide, with the monosaccharide having a higher concentration at the interface than the disaccharide and trisaccharide. The chemical composition of the interface and how it evolves under oxidative conditions will change the optical properties of the particles and their surface tension. This will ultimately affect the reflective property of the atmosphere and the process of cloud nucleation. For multicomponent aqueous aerosols, it becomes vital to understand the role of partitioning at the interface involved in the particle aging. Including such effects in atmospheric and cloud formation models may lead to dramatic changes in their predictive abilities.

5.5 Conclusion

The heterogeneous oxidation of the MGP-lactose aqueous droplets reveals a much higher reactive uptake coefficient for MGP than for lactose. In aqueous droplets, the bulk diffusion of the reactants is not to be the rate limiting step. The difference in reactive uptake coefficients appears to be consistent with the formation of a lactose exclusion layer at the surface of the particle. Molecular dynamic simulations suggest that there is formation of a ~1 nm lactose exclusion layer below the particle surface in the MGP-lactose aqueous droplets. The lactose abundance is low within the first few molecular layers of the air-water interface while that of the MGP is up to one order of magnitude larger. There is a higher probability of finding the MGP at the open water surface relatively to the lactose.

The simple stochastic modeling shows that the observed kinetics trend can be reproduced if there is a sufficient amount of MGP within the lactose exclusion layer to react with the OH radicals. The decay of the lactose is found to be strongly dependent on the amount of radicals diffusing below the lactose exclusion layer. This developed model is found insufficient to reproduce the behavior observed for the heterogeneous OH oxidation of binary aqueous-lactose droplets. In this case, the formation of oxidation products and their diffusion into the exclusion layer may lead to a more complex kinetic behavior.

The study of the heterogeneous OH oxidation of the MGP-lactose aqueous droplets provides a further understanding the role of surface-bulk partitioning on aqueous aerosol chemistry. A full understanding of the elementary phenomena controlling the chemical transformation requires more detailed investigations of the reactivity of aerosols containing organic compounds with different degrees of oxidation. It is likely that the inclusion of surface partitioning in the chemistry of aqueous aerosols could have a transformative effect on the predictive ability of atmospheric models.

References:

1.   Zakatova, N. V. M., D. P. and Sharpatyi, V. A., Role of OH-radicals in the radiolytic decomposition of carbohydrates and polysaccharides. *Bull. Acad. Sci. USSR, Div. Chem. Sci. (Engl. Tran)* **1969**.

2.   Fan, H.; Wenyika Masaya, T.; Goulay, F., Effect of surface–bulk partitioning on the heterogeneous oxidation of aqueous saccharide aerosols. *Physical Chemistry Chemical Physics* **2019,** *21* (6), 2992-3001.

3.   Wiegel, A. A.; Liu, M. J.; Hinsberg, W. D.; Wilson, K. R.; Houle, F. A., Diffusive confinement of free radical intermediates in the OH radical oxidation of semisolid aerosols. *Physical Chemistry Chemical Physics* **2017,** *19* (9), 6814-6830.

4.   Houle, F. A.; Hinsberg, W. D.; Wilson, K. R., Oxidation of a model alkane aerosol by OH radical: the emergent nature of reactive uptake. *Physical Chemistry Chemical Physics* **2015,** *17* (6), 4412-4423.

5.   Song, M.; Liu, P. F.; Hanna, S. J.; Li, Y. J.; Martin, S. T.; Bertram, A. K., Relative humidity-dependent viscosities of isoprene-derived secondary organic material and atmospheric implications for isoprene-dominant forests. *Atmos. Chem. Phys.* **2015,** *15* (9), 5145-5159.

6.   Pegram, L. M.; Record, M. T., Using Surface Tension Data to Predict Differences in Surface and Bulk Concentrations of Nonelectrolytes in Water. *The Journal of Physical Chemistry C* **2009,** *113* (6), 2171-2174.

7.   Wan, E. C. H.; Yu, J. Z., Analysis of Sugars and Sugar Polyols in Atmospheric Aerosols by Chloride Attachment in Liquid Chromatography/Negative Ion Electrospray Mass Spectrometry. *Environmental Science & Technology* **2007,** *41* (7), 2459-2466.

Chapter Six

Conclusion:

Heterogeneous oxidation of semi-solid and
aqueous saccharide aerosols

Chapter 6. Conclusion

Heterogeneous oxidation of atmospheric aerosols is one of the least understood processes involved in the chemical aging (chemical oxidation) of atmospheric aerosols. This thesis mainly focuses on investigating the role of bulk diffusion in the heterogenous oxidation of semi-solid particles and figuring out the rate-limiting step in aqueous aerosol chemistry. The experiments were performed in an atmospheric pressure aerosol flow tube with online VUV-AMS (Vacuum-Ultraviolet Aerosol Mass Spectrometer) analysis technique and offline Teflon filter collection then analyzed using GC-MS (Gas chromatograph Gas chromatograph interfaced with a Single Quadrupole Mass Spectrometer) analysis technique. The organic particles used ranged from single component semi-solid, multiple component semi-solid to liquid phase state. The monosaccharide (MGP, methyl-β-D-glucopyranoside, $C_7H_{14}O_6$) and disaccharide (lactose, $C_{12}H_{22}O_{11}$) are chosen as model molecules to form highly oxygenated organic particles.

6.1 The kinetics of OH+semi-solid saccharide particles

The kinetics of the OH-initiated heterogeneous oxidation of MGP over a wide range of ambient relative humidity was studied in Chapter 3 with VUV-AMS analysis technique. [1] The observed kinetics behavior shows an initial rapid exponential decay followed by a slower decrease of the reactant fraction. The heterogeneous oxidation of MGP semi-solid particles is kinetically limited by the bulk diffusion of the reactant MGP (D_{MGP}). The reactive uptake coefficient of MGP (γ_{MGP}) is increased by a factor of 2.4 as the surrounding relative humidity ranging from 10% to 30%, which can be explained by a decrease of particle viscosity and increase of bulk diffusivity due to moisture-induced viscosity reduction. The observed decay rate of MGP depends on the bulk diffusion coefficient of MGP, which can be described by a reaction-diffusion kinetic model with a constant diffusion coefficient.

The heterogeneous oxidation of OH radicals with MGP-lactose semi-solid particles over different molar ratio of MGP:lactose changing from 1:1 to 4:1 at 30% relative humidity was studied in Chapter 4 using both VUV-AMS and GC-MS analysis techniques. [2] The value of γ_{MGP} is decreased by a factor of 5 as the molar ratio MGP:lactose is changed from 4:1 to 1:1. The value of γ_{MGP} shows a pronounced decrease with the mole fraction of lactose increased, which can be

explained by an increase of particle viscosity and decrease of MGP bulk diffusivity due to oligomer-induced viscosity increase. The values of γ_{Lact} are smaller than those of MGP within 20% at ratio 1:1 and 2:1, which can be illustrated by the value of D_{Lac} is 20% smaller than that of D_{MGP}. However, the value of γ_{Lac} is smaller than that of γ_{MGP} by a factor of 7 at ratio 4:1. The observed low reactivity of lactose in the relatively high viscosity of semi-solid particles, which is interpreted by a relatively low surface mole fraction of lactose due to the partitioning of lactose toward the bulk of particle.

A reaction-diffusion model with composition-dependent diffusion was applied to investigate the impact of oligomer on oxidation of semi-solid multi-component particles. This study demonstrates that Vignes-type equation may explain the changes in diffusivity altered by oligomerization. Simulation results suggest that a gradient diffusivity near the surface bulk and a decrease in particle surface viscosity in the oxidation of semi-solid multi-component particles. This model treatment allows prediction of the evolution of the diffusivity during oxidative aging of mixed organic multi-component aerosols.

From this kinetics of OH+semi-solid saccharide particles study, now we have a better understanding of the role of bulk diffusion in determining the oxidation rate of reactive species in the semi-solid particles. This study highlights that the diffusion of the bulk reactant from the particle inner core to its surface is the rate-limiting step in oxidation of the semi-solid aerosols. The reactivity difference among the molecule species in the relatively high viscosity of semi-solid particles can be estimated by its molecular size. We successfully resolve composition-dependent bulk diffusion and temporal change of bulk diffusivity in the complex multi-component semi-solid particles. Our simulation results suggest that a "hard skin" (a decrease in the viscosity of particle surface) formed at the outer layer of particle in the oxidation of semi-solid multi-component particles containing oligomers. The chemical life-time of reactive species in the semi-solid particles can increase from seconds to days as the bulk diffusion of reactants decrease by multiple orders of magnitude in response to low relative humidity or oligomerization.

6.2 The kinetics of OH+aqueous saccharide droplets

The kinetics of the OH-initiated heterogeneous oxidation of the MGP-lactose aqueous droplets was studied in Chapter 5 using an offline analysis technique. [3] The measured kinetics result reveals

the value of γ_{Lac} is smaller than that of γ_{MGP} is by a factor of 13. Molecular dynamic simulations suggest that there is formation of a ~1 nm lactose exclusion layer below the particle surface in the MGP-lactose aqueous droplets. The lactose abundance is low within the first few molecular layers of the air-water interface while that of the MGP is up to one order of magnitude larger. There is a higher probability of finding the MGP at the open water surface relatively to the lactose. A simple stochastic reaction-diffusion model was employed to explain the possible effect of lactose surface exclusion on the heterogeneous kinetics. A 2.5 nm length of lactose exclusion layers is able to reproduce the experimental trends, which is larger than that predicted by the MD simulations. Because of the fast reaction of the OH radical with the MGP, there is a poor spatial overlap of the OH radical at the interface with the lactose in the particle bulk.

From this kinetics of OH+aqueous saccharide droplets study, now we have learned the critical importance of partitioning of bulk reactant at the gas-liquid interface in determining the reaction rate of reactive species in aqueous droplets, where the bulk diffusion of the reactants is not the rate limiting step any more. It is evident that gas-liquid interface is important to properly account for chemical transformations in aqueous droplets. The chemical life of reactive species in aqueous droplets depends on the relative concentrations close to the particle surface. These findings demonstrate that the inclusion of surface partitioning in the chemistry of aqueous aerosols could have a transformative effect on the predictive ability of atmospheric models.

References:

1.   Fan, H.; Tinsley, M. R.; Goulay, F., Effect of Relative Humidity on the OH-Initiated Heterogeneous Oxidation of Monosaccharide Nanoparticles. *The Journal of Physical Chemistry A* **2015,** *119* (45), 11182-11190.

2.   Fan, H. and Goulay, F., Effect of bulk composition on the diffusion properties of saccharide aerosols. (In Preparation).

3.   Fan, H.; Wenyika Masaya, T.; Goulay, F., Effect of surface–bulk partitioning on the heterogeneous oxidation of aqueous saccharide aerosols. *Physical Chemistry Chemical Physics* **2019,** *21* (6), 2992-3001.